Including van der Waals interactions in first-principles electronic structure calculations

Lampros Andrinopoulos

Imperial College London,
Department of Physics

Thesis submitted for the degree of
Doctor of Philosophy of Imperial College London
and
Diploma of Imperial College

September 2013

Abstract

Dispersion (van der Waals or vdW) interactions are long-range, non-local in nature, and can be important for understanding and predicting structure and energetics in many systems. Examples of such systems include weakly bound dimers, molecules on surfaces and molecular crystals. Because of the inherent non-locality of these interactions, they are not accounted for by traditional local and semi-local exchange and correlation functionals in density functional theory (DFT). In this thesis, two different approaches to including dispersion interactions in DFT were investigated and implemented.

The first approach is based on a recently developed method [1] that maps the DFT ground-state electron density onto a set of maximally-localized Wannier functions (MLWFs). These MLWFs act as fragments of electron density that are used in a pairwise summation of the vdW contribution to the total energy. This contribution is added to the total DFT ground-state energy in a post-processing fashion. The method, as originally proposed, has a number of shortcomings that hamper its predictive power. To overcome these problems, we developed and implemented a number of improvements to it and demonstrated that these modifications give rise to calculated binding energies and equilibrium geometries that are in closer agreement to results of quantum-chemical coupled-cluster calculations.

The second approach, known as the vdW density functional (vdW-DF) method, incorporates a non-local vdW term directly into the exchange and correlation functional. Following a recent efficient implementation [2] we coded this approach and a number of vdW functionals (vdW-DF, vdW-DF2, optB88, optPBE) in the ONETEP linear-scaling DFT package, enabling treatment of very large systems that were previously too computationally demanding for such methods. We applied the vdW-DF method to a system of interest for applications in photovoltaics, namely fullerene (C_{60}) molecular crystals, and investigated the effect of including vdW interactions on the relative stability of different crystal structures.

The copyright of this thesis rests with the author and is made available under a Creative Commons Attribution Non-Commercial No Derivatives licence. Researchers are free to copy, distribute or transmit the thesis on the condition that they attribute it, that they do not use it for commercial purposes and that they do not alter, transform or build upon it. For any reuse or redistribution, researchers must make clear to others the licence terms of this work.

Preface

The work presented in this thesis was carried out between October 2009 and September 2013 at Imperial College London under the supervision of Dr. Arash A. Mostofi. I hereby declare that the work in this thesis is my own and any other work herein is appropriately referenced and acknowledged.

Acknowledgements

I would like to thank my supervisor Arash Mostofi for all the invaluable help and discussions during these four years, for being patient and motivating and overall an excellent supervisor. I would equally like to thank Nicholas Hine for the countless times he has been helpful and always available for discussion. I am grateful that I was given the opportunity to work with both Arash and Nick and have learned a lot from them.

I would also like to thank my parents and family for their love and support over the years and for always being there for me. Last but not least, I would like to thank all my lifelong friends that honour me with their friendship and keep me company, and also my flatmates.

Contents

1 Introduction **11**

2 Density Functional Theory **15**
2.1 The many-body electron problem 15
2.2 Density functional theory fundamentals 19
2.2.1 Hohenberg-Kohn theorems 19
2.2.2 Kohn-Sham equations 21
2.2.3 Exchange and correlation functionals 24
2.3 Solving the Kohn-Sham equations 27
2.3.1 Basis sets 27
2.3.2 Bloch's theorem 27
2.3.3 Plane waves 28
2.3.4 Pseudopotentials 30

3 Dispersion Interactions in DFT **33**
3.1 Theory and formalism 33
3.1.1 A simple picture 34
3.1.2 Multipole moments 36
3.1.3 Quantum mechanical picture 37
3.1.4 Dispersion energy 41
3.2 ACFD theorem 43
3.2.1 RPA methods 44
3.3 Quantum chemical methods 44
3.4 DFT Methods 45
3.4.1 Non-additivity 46
3.4.2 DFT+D 47
3.4.3 DFT+vdW 48
3.4.4 vdW-DF 51

4 vdW interactions with MLWFs **55**
4.1 Wannier functions 56
4.2 Silvestrelli's method 58
4.2.1 Original MLWF approach 58
4.2.2 Recent work 60

4.3 Improvements . . . 61
4.3.1 Partly Occupied Wannier Functions . . . 61
4.3.2 Modification to describe p-like states . . . 61
4.3.3 Symmetry Considerations . . . 63
4.4 Applications . . . 64
4.4.1 Calculation Details . . . 64
4.4.2 Argon . . . 65
4.4.3 Methane . . . 69
4.4.4 Ethene . . . 69
4.4.5 Benzene . . . 72
4.4.6 H_2Pc and CuPc . . . 73
4.4.7 Intermolecular C_6 coefficients . . . 80
4.4.8 Sensitivity to cutoff radius r_c . . . 81
4.4.9 Approximations to the density . . . 82
4.4.10 Sensitivity to energy window E_{win} . . . 84
4.5 vdW interactions with NGWFs . . . 86
4.6 Conclusion . . . 89

5 The vdW-DF method in ONETEP 92
5.1 Linear-scaling DFT . . . 93
5.2 ONETEP . . . 94
5.3 Overview of Soler's method . . . 99
5.3.1 Original vdW-DF formulation . . . 99
5.3.2 Non-local correlation energy . . . 100
5.3.3 Kernel . . . 102
5.3.4 Non-local potential . . . 102
5.4 vdW-DF flavours . . . 103
5.5 Validation tests for vdW-DF . . . 105
5.6 Scaling in ONETEP . . . 106

6 Buckminsterfullerene (C_{60}) 109
6.1 Motivation . . . 109
6.2 Structure . . . 112
6.3 Applications . . . 115
6.3.1 Calculation details . . . 115
6.3.2 Orientational dependence of total energy . . . 116
6.3.3 Geometry and energetics . . . 121
6.3.4 Rotational freedom . . . 123
6.4 Conclusion . . . 124

7 Conclusion 126

A Inverse of overlap matrix 151

B vdW-DF non-local correlation in reciprocal space 153

C Becke 88 exchange **155**

List of Tables

4.1 Equilibrium separation for benzene dimers. 75
4.2 Binding energies for benzene dimers. 75
4.3 Effective intermolecular C_6 coefficients. 81

5.1 vdW-DF validation tests for S22. 106

6.1 Lattice parameters and cohesive energies for C_{60}. 122

List of Figures

3.1 Simple harmonic oscillators. 34

4.1 p-like orbital on benzene molecule 63
4.2 Orientation of MLWF centres for argon dimer. 66
4.3 Binding energy for argon dimer with revPBE. 67
4.4 Binding energy for argon dimer with vdW corrections. 68
4.5 Methane dimer molecules. 69
4.6 Binding energy for methane dimer. 70
4.7 MLWF centres on ethene dimers. 71
4.8 Binding energy for ethene dimer. 71
4.9 Benzene dimer in S configuration. 73
4.10 Binding energies for benzene dimers. 74
4.11 Phthalocyanine molecule and its MLWF centres. 77
4.12 Binding energy of phthalocyanine dimer. 78
4.13 Copper phthalocyanine molecule and its MLWFs. 79
4.14 Binding energy for copper phthalocyanine dimer. 80
4.15 Effect of cutoff radius on energy of benzene dimer. 82
4.16 Kohn-Sham and and off-diagonal density profiles. 83
4.17 Density profiles on benzene ring with valence MLWFs. 84
4.18 Density profiles on benzene rings with our method. 85
4.19 Effect of energy window on energy of benzene dimer. 86

5.1 Kohn-Sham orbitals and NGWFs. 96
5.2 Psinc grid and NGWF localization. 97
5.3 Timings for ONETEP calculation on C_{60} crystal. 108

6.1 Symmetric truncated icosahedron structure. 113
6.2 C_{60} crystal unit cell. 114
6.3 Binding curve for C_{60} with PBE. 117
6.4 Binding curve for C_{60} with opt-vdW functionals. 117
6.5 Energy vs angle for C_{60} with different functionals. 118
6.6 Alignment of C_{60} bonds with pentagon/hexagon. 119
6.7 Cohesive energy for C_{60} with opt-vdW functionals. 119
6.8 Effect of relaxation on energy of C_{60} crystal. 120
6.9 Bond length frequency for C_{60}. 123

6.10 Energy curve for orientationally defective C_{60} crystal. 124

Chapter 1

Introduction

A little over a century ago, the theory of quantum mechanics made its appearance. It introduced concepts and ideas that were in contradiction to what was believed at the time about how atoms and molecules behave, and what laws of physics apply to the microscopic level. The electrons were no longer considered particles but also sometimes as waves. Their motion was not governed by deterministic principles, but was rather probabilistic. Despite its counter-intuitive nature, quantum mechanics has repeatedly been shown to work, and is regularly validated to remarkable precision. The widely used Schrödinger equation is the starting point for many quantum problems, and is the one we use here.

The understanding generated by quantum mechanics is largely responsible for the rapid development of technology over the past century. For instance, exploring the behaviour of materials at the microscopic level would be impossible without quantum mechanics, since it is the structure and composition of atoms and molecules that determines their properties and in particular their *electronic structure*. Up until a few decades ago, the extensive study of materials was almost exclusively limited to a combination of experiment and analytic theory, which is quite limiting on its own. Solving the Schrödinger equation for a many-body system is an extremely challenging task, and exact solutions do not exist even for systems with a small number of particles. While approximate solutions were in some cases obtained with iterative numerical methods, the scope was very limited. The introduction of digital computers revolutionized the way numerical methods were applied, and allowed for many procedures to be automated, thus performing previously time-consuming tasks relatively fast. With the appearance of a new era of faster computers, as well as the development

of efficient algorithms, the interest in simulating materials using computational methods dramatically increased. Beyond the theoretical interest, simulating materials has also very important applicability to industry, particularly technology. The simulation of materials can be extremely useful for discovering new properties by examining their predicted behaviour. As a result, significant research effort is been devoted to further developing and improving methods and algorithms that allow more accurate and more efficient simulations.

Computational simulations are not exact when approximations have been used in order to perform the operations within a realistic timeframe. The challenge is then to find methods which are accurate enough but also efficient; unfortunately these are often competing requirements. One good compromise is density functional theory (DFT). It has been increasingly used since its conception, with an explosion in its use and performance, and is still being used to this day very successfully for applications on a number of systems. Its further development is still a very active research topic, with a number of different branches that are constantly being expanded. The accuracy of any approximate method can always be improved by "including more physics" into it, as some physics is missed either partly or completely because of the underlying approximations made. A type of interaction that is missed by traditional DFT is dispersion, or van der Waals (vdW). Because of the local or semi-local nature of most common approximations to the exchange and correlation functionals used in DFT simulations, DFT is not able to capture these interactions. Dispersion interactions are long-range and non-local in nature. They are weaker than ionic or covalent interactions, but are very important in weakly bound systems such as molecular dimers, molecular crystals and organic systems. Including vdW in DFT has been desirable since the early days of DFT, but very recently there has been a dramatic increase in interest in this particular subject. Many methods, of varying degrees of accuracy, have been developed within DFT codes and tested on a number of systems, with a vast range of applications to realistic systems. For example, it is of interest to study fullerene crystals, which are dominated by vdW interactions, as it has been show that they can improve the efficiency of photovoltaic devices [3–5].

This thesis is structured as follows: In Chapter 2 we give an overview of the theoretical framework used in density functional theory. First we introduce the many-body problem, and discuss the problems it poses. We then introduce the concept of density functional theory, whereby the electronic density is used as the fundamental variable of the system, and discuss the advantages of this

approach. The concept of the energy density functional is introduced and the various ways of approximating it are mentioned. Next, the main methods used to simplify the task of solving the many-body equation in DFT are briefly outlined. The limitations and successes of DFT are put into context.

In Chapter 3, a brief review of vdW interactions and their nature is given. Starting from a simple picture, we show how vdW interactions arise and how to describe them mathematically to various levels of sophistication. We follow this with a discussion of various methods to include vdW in electronic structure, focusing in particular on the DFT framework. The physical motivation of these methods and the approximations they rely on is given, and their performance and efficiency are assessed.

In Chapter 4, we focus on one of the methods (Silvestrelli 2008 [1]) that has been developed to include vdW in DFT. As this method is based on the use of maximally-localized Wannier functions [6] (MLWFs), we first introduce the MLWF concept. This method relies on approximating the real electronic density of the system by using MLWFs to partition the density, and then approximate those MLWFs with hydrogenic orbitals. This approximate density is then used in an expression to evaluate the vdW energy of the system in a post-processing fashion. We study the method carefully, apply it to a range of increasingly complex systems and assess its performance. We identify a number of shortcomings and address some of them by proposing modifications to the method, yielding significant improvement on a number of the systems we study; we compare against quantum chemical coupled-cluster calculations and find much better agreement than the original method. We discuss the method's limitations when moving to larger and more structurally complex systems. This work has been published as *J. Chem. Phys.* **135**, 154105 (2011) [7].

In Chapter 5, we show how another recently proposed efficient method for the inclusion of vdW in DFT was implemented within the Order-N Electronic Total Energy Package [8] (ONETEP) framework and present its formulation. The original method by Dion *et al.* [9] is termed vdW-DF as it proposes a vdW non-local correlation functional which is to be included in a fully self-consistent calculation. The efficient nearly-linear scaling implementation that has been proposed [2] make it an ideal addition to ONETEP, allowing the simulation of large weakly-bound systems. Many of the proposed variations (flavours) to the vdW-DF have also been implemented in ONETEP, such as the vdW-DF2 by Lee *et al.* [10] and the "opt-vdW" functionals by Klimeš *et al.* [11], and are also discussed. An overview of linear-scaling density functional theory is

given, with particular focus on ONETEP, which makes use of highly-localized non-orthogonal orbitals to calculate the ground state electronic density and ultimately the total ground state energy of the system in a linear-scaling fashion, meaning that the computational time for a calculation scales linearly with the number of atoms in the system. This is achieved by applying a number of spatial cutoffs justified by the near-sightedness of electronic structure. The basic formulation and approximations used in the code are given.

In Chapter 6, we focus on the structure known as Buckminsterfullerene (C_{60}), or bucky-ball. The bucky-ball was discovered in 1985 by Kroto *et al.* [12] and has been extensively studied experimentally. It is found in an ordered crystal structure at low temperatures; at higher temperatures, there is disorder in the system. We give an overview of the available literature regarding experimental and electronic structure research on the bucky-ball and discuss why it is a good testing system for vdW-DF functionals, as well as its potential use in applications. We apply a number of functionals, amongst which are various flavours of the vdW-DF and present our results on geometry, structure and energetics on the C_{60} crystal; we compare to experimental values as well as other electronic structure simulations from the literature, and find reasonable overall agreement. Remarkable agreement is found for one vdW-DF functional (optPBE) for the lattice parameter of the crystal cell with respect to the experimental value. We argue that a particular family of vdW-DF flavours might indeed be appropriate for studying molecular crystals.

In Chapter 7, we draw our conclusions regarding our work, and where it stands in the framework of the field, and discuss potential future directions that may be taken in the spirit of vdW functionals within linear-scaling DFT.

Chapter 2

Density Functional Theory

A method used in computational simulations that has gained increasing popularity due to its efficiency and accuracy is Density Functional Theory (DFT). Density functional theory is a quantum mechanical theory which uses the electronic density of the system as the fundamental variable rather than the full many-body wavefunction. In this chapter, the electronic many-body problem is presented first, followed by the fundamentals of DFT, the various approximations used in it, as well as a brief discussion on implementation and scaling of DFT computational codes.

2.1 The many-body electron problem

The single-particle time-dependent Schrödinger equation is the starting point for any quantum problem:

$$\Big(-\frac{\hbar^2}{2m}\nabla^2 + V(\mathbf{r})\Big)\Phi(\mathbf{r},t) = i\hbar\frac{\partial\Psi(\mathbf{r},t)}{\partial t} \tag{2.1}$$

where m is the mass of the particle, $\Phi(\mathbf{r},t)$ is the wavefunction of the system and $V(\mathbf{r})$ is the potential energy of the particle at the given position. The physical interpretation of the wavefunction is given through $|\Phi(\mathbf{r},t)|^2$, which is the probability density at position $\mathbf{r}$ and time t. The probability of finding the particle in an infinitesimal volume δV around the position $\mathbf{r}$ at time t is then $|\Phi(\mathbf{r},t)|^2\delta V$.

Assuming that the wavefunction can be written in a separable form as $\Phi(\mathbf{r},t) = \Psi(\mathbf{r})\Omega(t)$, it can be easily shown by separation of variables that the

time-independent Schrödinger equation is:

$$\Big(-\frac{\hbar^2}{2m}\nabla^2 + V(\mathbf{r})\Big)\Psi(\mathbf{r}) = E\Psi(\mathbf{r}) \tag{2.2}$$

where E is the separation constant and represents an energy eigenvalue, while the time-dependent part of the equation satisfies:

$$i\frac{\partial\Omega(t)}{\partial t} = E\Omega. \tag{2.3}$$

Eq. 2.3 yields a trivial exponential solution, and Eq. 2.2 has to be solved for the particular potential. The operator $-\frac{\hbar^2}{2m}\nabla^2 + V(\mathbf{r})$ is called the *Hamiltonian* of the system. The time-independent Schrödinger is the one that we will be concerned with here.

Determining the properties of a material *ab initio*, that is without any empirical parameters characterising it other than its atomic structure, involves solving the Schrödinger equation for a system of many interacting particles. We start by extending Eq. 2.1 to a collection of particles by writing the Hamiltonian for a system of electrons at positions $\{\mathbf{r}_i\}$ with charges e, and nuclei at positions $\{\mathbf{R}_I\}$ with charges $Z_I e$ as

$$\begin{aligned}\hat{\mathcal{H}} = -\frac{\hbar^2}{2m_e}\sum_i \nabla_i^2 - \sum_{i,I}\frac{Z_I e^2}{4\pi\epsilon_0|\mathbf{r}_i - \mathbf{R}_I|} + \frac{1}{2}\sum_{i\neq j}\frac{e^2}{4\pi\epsilon_0|\mathbf{r}_i - \mathbf{r}_j|} \\ - \sum_I \frac{\hbar^2}{2M_I}\nabla_I^2 + \frac{1}{2}\sum_{I\neq J}\frac{Z_I Z_J e^2}{4\pi\epsilon_0|\mathbf{R}_I - \mathbf{R}_J|}\end{aligned} \tag{2.4}$$

where m_e is the mass of an electron, M_I the mass of the I-th nucleus, and the Laplacian operators only act on their corresponding coordinates. In order to work with quantities of order 1, the atomic, or Hartree units are adopted, in which $e = m_e = \hbar = a_0 = 4\pi\epsilon_0 = 1$. The dimensionless Hamiltonian then reads:

$$\begin{aligned}\hat{\mathcal{H}}' = -\frac{1}{2}\sum_i \nabla_i^2 - \sum_{i,I}\frac{Z_I}{|\mathbf{r}_i - \mathbf{R}_I|} + \frac{1}{2}\sum_{i\neq j}\frac{1}{|\mathbf{r}_i - \mathbf{r}_j|} \\ - \sum_I \frac{1}{2M_I}\nabla_I^2 + \frac{1}{2}\sum_{I\neq J}\frac{Z_I Z_J}{|\mathbf{R}_I - \mathbf{R}_J|}.\end{aligned} \tag{2.5}$$

Atomic units will be used throughout this thesis, unless otherwise specified.

An important approximation is the Born-Oppenheimer (BO) [13] or adiabatic approximation, in which the nuclei are treated as classical particles. The

electrons are assumed to remain in a specific choice of ground or excited state as the nuclei move. The BO approximation allows to get from the full Hamiltonian of the full electronic and nuclear system to the Hamiltonian of the electrons only, which depends only parametrically on $\{\mathbf{R}_I\}$. First, the following form for the electron nuclei wavefunction is assumed:

$$\Psi(\{\mathbf{R}_I\},\{\mathbf{r}_i\}) = \sum_n \Theta_n(\{\mathbf{R}_I\})\Phi_n(\{\mathbf{R}_I,\mathbf{r}_i\}) \tag{2.6}$$

and now the $\Phi_n(\{\mathbf{R}_I,\mathbf{r}_i\})$ satisfy the Schrödinger equation for the electron-only Hamiltonian:

$$\hat{H}_\mathrm{e}\Phi_n(\{\mathbf{R}_I,\mathbf{r}_i\}) = E_n(\{\mathbf{R}_I\})\Phi_n(\{\mathbf{R}_I,\mathbf{r}_i\}) \tag{2.7}$$

where

$$\hat{H}_\mathrm{e} = -\frac{1}{2}\sum_i \nabla_i^2 - \sum_{i,I}\frac{Z_I}{|\mathbf{r}_i-\mathbf{R}_I|} + \frac{1}{2}\sum_{i\neq j}\frac{1}{|\mathbf{r}_i-\mathbf{r}_j|} \tag{2.8}$$

is the electron-only Hamiltonian. We define

$$\hat{T} = -\frac{1}{2}\sum_i \nabla_i^2 \tag{2.9}$$

$$\hat{V}_\mathrm{ne} = \sum_{i,I}\frac{Z_I}{|\mathbf{r}_i-\mathbf{R}_I|} \tag{2.10}$$

$$\hat{U}_\mathrm{ee} = \frac{1}{2}\sum_{i\neq j}\frac{1}{|\mathbf{r}_i-\mathbf{r}_j|} \tag{2.11}$$

where $\hat{U}_\mathrm{ee}$ is the operator for the electron interaction, $\hat{T}$ is the kinetic energy operator, and $\hat{V}_\mathrm{ne}$ the electron-nuclear interaction operator.

Substituting an ansatz for the wavefunction of the separable form $\Psi = \Theta(\{\mathbf{R}_I\})\Phi(\{\mathbf{R}_I,\mathbf{r}_i\})$ into the full Hamiltonian of Eq. 2.5 and recalling Eq. 2.7, one obtains

$$\begin{aligned}
&\hat{\mathcal{H}}'\Psi(\{\mathbf{R}_I\},\{\mathbf{r}_i\}) = \\
&\Phi(\{\mathbf{R}_I,\mathbf{r}_i\})\Big[-\sum_I\frac{1}{2M_I}\nabla_I^2 + \frac{1}{2}\sum_{I\neq J}\frac{Z_IZ_J}{|\mathbf{R}_I-\mathbf{R}_J|} + E_n(\{\mathbf{R}_I\})\Big]\Theta(\{\mathbf{R}_I\}) \\
&-\sum_I\frac{1}{2M_I}\Big[\nabla_I^2\Theta(\{\mathbf{R}_I\})\nabla_I^2\Phi(\{\mathbf{R}_I,\mathbf{r}_i\}) + 2\nabla_I\Theta(\{\mathbf{R}_I\})\cdot\nabla_I\Phi(\{\mathbf{R}_I,\mathbf{r}_i\})\Big]
\end{aligned} \tag{2.12}$$

Because the ∇_I operator acts on the $\mathbf{R}_I$ space, it also operates on the elec-

tronic wavefunction $\Phi(\{\mathbf{R}_I, \mathbf{r}_i\})$. As a result, two terms containing off-diagonal components appear in Eq. 2.12 meaning that Eq. 2.6 is not an eigenstate of $\hat{\mathcal{H}}'$. However, based on the fact that nuclei are heavier than electrons, we can ignore the off-diagonal terms since they are multiplied by $1/2M_I$. Ultimately, the electron part of the separable wavefunction satisfies the Schrödinger equation in Eq. 2.7 and the nuclear wavefunction satisfies a Schrödinger equation in which the electronic energy is a mean-field potential. Unless otherwise stated, we will work with the electronic Hamiltonian throughout this work. From now on, the parametric dependence of the electronic wavefunction and energy eigenvalues on the nuclear coordinates will no longer be denoted, and implicitly assumed. For a system with N electrons, the Hamiltonian defined in Eq. 2.8 will be used with a wavefunction $\Psi(\mathbf{r}_1, \ldots, \mathbf{r}_N)$. The wavefunction has to be antisymmetric under exchange of any pair of electrons, that is

$$\Psi(\mathbf{r}_2, \mathbf{r}_1, \ldots, \mathbf{r}_N) = -\Psi(\mathbf{r}_1, \mathbf{r}_2, \ldots, \mathbf{r}_N) \tag{2.13}$$

and also normalized, so that

$$\int |\Psi(\mathbf{r}_1, \ldots, \mathbf{r}_N)|^2 \prod_i^N d\mathbf{r}_i = 1. \tag{2.14}$$

The exchange condition arises because of the indistinguishability of electrons, and the normalization condition ensures that the probability of finding the electrons *anywhere* in space is 1.

Analytical or exact numerical solutions of $3N$ coupled second order partial differential equations can only be found for a very small N. For larger numbers of interacting particles, solution of the $3N$-dimensional partial differential equations becomes an impossible computational task. A method is then required which makes the problem more tractable, but also yields reasonably accurate results. Density functional theory has been successful in achieving remarkably accurate results for a wide range of systems [14] and is currently the method of choice for simulating materials.

2.2 Density functional theory fundamentals

In density functional theory, the fundamental variable of the system is the electronic density

$$\rho(\mathbf{r}) = N \int d\mathbf{r}_2 \ldots \int d\mathbf{r}_N |\Psi(\mathbf{r}, \mathbf{r}_2, \ldots, \mathbf{r}_N)|^2 \tag{2.15}$$

rather that the full many-body wavefunction. The energy is expressed as a functional of the electronic density, and the ground state energy can be calculated by minimizing this functional after making a number of well-justified approximations. We start by stating and showing the proof of two important theorems by Hohenberg and Kohn.

2.2.1 Hohenberg-Kohn theorems

In 1964 Hohengerg and Kohn (HK) proved two theorems [15] underpinning DFT as it is known today. The first theorem states that there is a one-to-one mapping between the electronic density and the external potential $V_{\text{ext}}(\mathbf{r})$, which we define as the electron-nuclear potential from Eq. 2.10, so $\hat{V}_{\text{ext}} = \hat{V}_{\text{ne}}$. As a result of the one-to-one mapping between the electronic density and the external potential, the ground state wavefunction is also determined by the density. The second theorem states that there exists a universal functional of the density, $F[\rho]$, valid for any external potential $V_{\text{ext}}(\mathbf{r})$; the ground state energy of the system for any particular $V_{\text{ext}}(\mathbf{r})$ is then the global minimum of that functional, and the density that minimizes it corresponds to the ground state density. The great importance of the HK theorems is that all the information about the ground state is embodied in the density as opposed to the $3N$ variable many-body wavefunction. This on its own is remarkable: the problem of solving $3N$ coupled differential equations can be reduced down to determining the ground state density. In the next sections, the HK theorems will be proved and their implications discussed.

First HK theorem

We start from the Schrödinger equation for the electrons, now using "bra" and "ket" notation for a wavefunction $|\Psi\rangle$, and dropping the e subscript from the

Hamiltonian for convenience:

$$\hat{H}|\Psi\rangle = \left(\hat{T} + \hat{U}_{\text{ee}} + \hat{V}_{\text{ext}}\right)|\Psi\rangle = E|\Psi\rangle. \tag{2.16}$$

To prove the first theorem [16], let us suppose we have two different external potentials $V_{\text{ext}}(\mathbf{r})$ and $V'_{\text{ext}}(\mathbf{r})$, for two systems that have the same number of electrons. The Hamiltonians of the two systems corresponding to the two external potentials are $\hat{H} = \hat{T} + \hat{U}_{\text{ee}} + \hat{V}_{\text{ext}}$ and $\hat{H}' = \hat{T} + \hat{U}_{\text{ee}} + \hat{V}'_{\text{ext}}$. Let $|\Psi\rangle$, $|\Psi'\rangle$ be the ground state wavefunctions of the two different systems. We can write their ground state energies as $E_0 = \langle\Psi|\hat{H}|\Psi\rangle$ and $E'_0 = \langle\Psi'|\hat{H}'|\Psi'\rangle$.

Using the Rayleigh-Ritz variational principle, we know that the energy of the ground state is the minimum, so it will always be smaller than the energy of any other state. We can then write

$$\begin{aligned} E_0 &< \langle\Psi'|\hat{H}|\Psi'\rangle \\ &= \langle\Psi'|\hat{H}'|\Psi'\rangle + \langle\Psi'|\hat{H} - \hat{H}'|\Psi'\rangle \\ &= E'_0 + \langle\Psi'|\hat{V}_{\text{ext}} - \hat{V}'_{\text{ext}}|\Psi'\rangle \end{aligned}$$

so

$$E < E'_0 + \int \rho(\mathbf{r})(V_{\text{ext}}(\mathbf{r}) - V'_{\text{ext}}(\mathbf{r}))d\mathbf{r} \tag{2.17}$$

Following the same argument,

$$E'_0 < E_0 - \langle\Psi|\hat{V}'_{\text{ext}} - \hat{V}_{\text{ext}}|\Psi\rangle = E_0 - \int \rho(\mathbf{r})(V'_{\text{ext}}(\mathbf{r}) - V_{\text{ext}}(\mathbf{r}))d\mathbf{r} \tag{2.18}$$

Adding 2.17 to 2.18 gives $E_0 + E'_0 < E'_0 + E_0$, which is contradictory; thus it is concluded that two different external potentials cannot give rise to the same ground state electronic density, $\rho_0(\mathbf{r})$. Therefore, there is a one-to-one correspondence between $V_{\text{ext}}(\mathbf{r})$ and $\rho_0(\mathbf{r})$. Since the electronic density determines the external potential, it should also determine the ground state wavefunction, therefore the energy must be a functional of the electronic density.

Second HK theorem

The second theorem proves that the ground state energy is a functional of the density, which can be deduced from the previous part of the theorem by considering the following argument:

The energy functional is defined as

$$E_{\mathrm{HK}}[\rho] = F_{\mathrm{HK}}[\rho] + \int \rho(\mathbf{r}) V_{\mathrm{ext}}(\mathbf{r}) d\mathbf{r} \tag{2.19}$$

where

$$F_{\mathrm{HK}}[\rho] = T[\rho] + U_{\mathrm{ee}}[\rho] \tag{2.20}$$

is a universal functional for systems with the same number of electrons, independent of the external potential.

Considering a system with a ground state density $\rho_0(\mathbf{r})$ corresponding to an external potential $V_{\mathrm{ext}}(\mathbf{r})$, we can write the ground state energy as $E = E_{\mathrm{HK}}[\rho] = \langle\Psi|\hat{H}|\Psi\rangle$, where $|\Psi\rangle$ is the wavefunction of the system. For a different density $\rho(\mathbf{r})$ corresponding to a different wavefunction Ψ' we have $E' = E_{\mathrm{HK}}[\rho'] = \langle\Psi'|\hat{H}|\Psi'\rangle > E$ since $|\Psi'\rangle$ is not the ground state of the Hamiltonian $\hat{H}$. It is therefore concluded that the ground state density gives the lowest energy, corresponding to the ground state energy.

The ground state energy can be calculated by minimizing the energy functional, imposing the constraint that the electronic density integrates to the number of particles, $\int \rho(\mathbf{r}) d\mathbf{r} = N$. The Euler-Lagrange equation then reads:

$$\frac{\delta}{\delta\rho(\mathbf{r})}\{E_{\mathrm{HK}}[\rho] - \mu \int \rho(\mathbf{r}') d\mathbf{r}'\} = 0 \tag{2.21}$$

which yields

$$\mu = V_{\mathrm{ext}}(\mathbf{r}) + \frac{\delta F_{\mathrm{HK}}[\rho]}{\delta\rho(\mathbf{r})} \tag{2.22}$$

where μ is the chemical potential.

2.2.2 Kohn-Sham equations

Since F is an unknown functional, an approximation is needed to be able to calculate the energy. A widely used scheme was proposed by Kohn and Sham (KS) [17] which makes the problem tractable.

As the HK theorem proves, the energy can be written as a functional of the density. The ground state energy of a system is then

$$E[\rho] = F_{\mathrm{HK}}[\rho] + \int \rho(\mathbf{r}) V_{\mathrm{ext}}(\mathbf{r}) d\mathbf{r} \tag{2.23}$$

Since the functional $F_{\mathrm{HK}}[\rho]$ is independent of the external potential, Kohn and

Sham proposed to use an auxiliary non-interacting system with the same ground state density as the real, interacting one. The non-interacting system can be written in terms of one-electron orbitals, thus making the equations easy to solve. The Hamiltonian describing this non-interacting system is

$$\hat{H}_{\mathrm{non-int}} = \sum_{i=1}^{N} \left[-\frac{1}{2}\nabla_i^2 + V_{\mathrm{eff}}(\mathbf{r}_i) \right] \tag{2.24}$$

where $V_{\mathrm{eff}}(\mathbf{r})$ is an effective potential that gives rise to the same density as the fully interacting real system.

The eigenstates of this Hamiltonian are described by an antisymmetric wavefunction written as a *Slater determinant*, which encompasses the anti-symmetry of the wavefunction under the exchange of two electrons:

$$\Psi(\mathbf{r}_1 \dots \mathbf{r}_N) = \frac{1}{\sqrt{N!}} \begin{vmatrix} \psi_1(\mathbf{r}_1) & \dots & \psi_N(\mathbf{r}_1) \\ \vdots & \ddots & \vdots \\ \psi_1(\mathbf{r}_N) & \dots & \psi_N(\mathbf{r}_N) \end{vmatrix}. \tag{2.25}$$

It can be shown using the definition of the density in Eq. 2.15 that for a wavefunction of the form given in Eq. 2.25, the expression for the density becomes

$$\rho(\mathbf{r}) = 2 \sum_{i}^{N/2} |\psi_i(\mathbf{r})|^2 \tag{2.26}$$

for doubly degenerate orbitals, where the Slater determinant only has $N/2$ single particle states.

The kinetic energy term of the non-interacting system is then:

$$\hat{T}_{\mathrm{s}} = -\frac{1}{2} \sum_{i} \langle \psi_i | \nabla^2 | \psi_i \rangle \tag{2.27}$$

The one-electron orbitals are solutions to the Schrödinger equation

$$\hat{H}_{\mathrm{KS}} \psi_i(\mathbf{r}) = \varepsilon_i \psi_i(\mathbf{r}) \tag{2.28}$$

where $\hat{H}_{\mathrm{KS}}$ is the single-electron Kohn-Sham Hamiltonian

$$\hat{H}_{\mathrm{KS}} = -\frac{\nabla^2}{2} + V_{\mathrm{eff}}(\mathbf{r}). \tag{2.29}$$

The ground state energy of the KS system can then be written as

$$E_{\mathrm{KS}}[\rho] = T_{\mathrm{s}}[\rho] + \int V_{\mathrm{eff}}(\mathbf{r})\rho(\mathbf{r})d\mathbf{r} \tag{2.30}$$

so the Euler-Lagrange equation for the KS system is:

$$\mu_{\mathrm{s}} = \frac{\delta T_{\mathrm{s}}[\rho]}{\delta\rho(\mathbf{r})} + V_{\mathrm{eff}}(\mathbf{r}) \tag{2.31}$$

where μ_s is again a chemical potential.

Recalling Eq. 2.20 we can write:

$$\begin{aligned} F_{\mathrm{HK}}[\rho] &= T[\rho] + U_{\mathrm{ee}}[\rho] \\ &= T_{\mathrm{s}}[\rho] + E_{\mathrm{H}}[\rho] + E_{\mathrm{xc}}[\rho] \end{aligned} \tag{2.32}$$

where

$$E_{\mathrm{H}}[\rho] = \frac{1}{2}\int\int \frac{\rho(\mathbf{r})\rho(\mathbf{r}')}{|\mathbf{r}-\mathbf{r}'|}d\mathbf{r}d\mathbf{r}' \tag{2.33}$$

is the Hartree energy and $E_{\mathrm{xc}}[\rho]$ is the *exchange-correlation* functional containing all the many-body effects of the system and in this case also includes the kinetic correlation ignored in the kinetic energy of the non-interacting system $T_{\mathrm{s}}[\rho]$. Having made this decomposition, we have essentially reduced the many-body problem down to determining the exchange and correlation functional. This decomposition is also very convenient as it allows to treat each term separately, in different approximations. Now, from Eq. 2.19 and Eq. 2.32 we can write

$$E_{\mathrm{HK}}[\rho] = T_s[\rho] + E_H[\rho] + \int \rho(\mathbf{r})V_{\mathrm{ext}}(\mathbf{r})d\mathbf{r} + E_{\mathrm{xc}}[\rho]. \tag{2.34}$$

Taking the functional derivative of Eq. 2.34 and Eq. 2.19 with respect to the density and equating them (or equivalently equating Eq. 2.31 to Eq. 2.22), we obtain

$$\frac{\delta T_{\mathrm{s}}[\rho]}{\delta\rho(\mathbf{r})} + V_{\mathrm{eff}}[\rho](\mathbf{r}) = \frac{\delta T_{\mathrm{s}}[\rho]}{\delta\rho(\mathbf{r})} + \frac{\delta E_{\mathrm{H}}[\rho]}{\delta\rho(\mathbf{r})} + \frac{\delta E_{\mathrm{xc}}[\rho]}{\delta\rho(\mathbf{r})} + V_{\mathrm{ext}}[\rho](\mathbf{r}) \tag{2.35}$$

so now the effective potential can be written as:

$$V_{\mathrm{eff}}[\rho](\mathbf{r}) = V_{\mathrm{ext}}[\rho](\mathbf{r}) + \int \frac{\rho(\mathbf{r}')}{|\mathbf{r}-\mathbf{r}'|}d\mathbf{r}' + \frac{\delta E_{\mathrm{xc}}[\rho]}{\delta\rho(\mathbf{r})}. \tag{2.36}$$

The $\int \frac{\rho(\mathbf{r}')}{|\mathbf{r}-\mathbf{r}'|} d\mathbf{r}'$ term is called the *Hartree potential* and denoted V_{H}. Now the Schrödinger equation

$$\left[-\frac{\nabla^2}{2} + V_{\mathrm{eff}}[\rho](\mathbf{r})\right] \psi_i(\mathbf{r}) = \varepsilon_i \psi_i(\mathbf{r}) \tag{2.37}$$

has to be solved to obtain the eigenvalues ε_i. Since the effective potential is a functional of the density, Eq. 2.37 has to be solved self-consistently: an initial guess for the density is used to solve the equation for the energy and once solved, the new density is constructed from the resulting eigenfunctions; this continues in an iterative fashion, until convergence of the energy within a certain threshold is achieved. This is the basis for many DFT codes.

The ground state energy is calculated as:

$$E[\rho] = 2\sum_i \varepsilon_i - \frac{1}{2}\int\int \frac{\rho(\mathbf{r})\rho(\mathbf{r}')}{|\mathbf{r}-\mathbf{r}'|} d\mathbf{r} d\mathbf{r}' + E_{\mathrm{xc}}[\rho] - \int V_{\mathrm{xc}}[\rho(\mathbf{r})]\rho(\mathbf{r}) d\mathbf{r} \tag{2.38}$$

where the double counting is removed by subtracting the appropriate terms and $V_{\mathrm{xc}}[\rho(\mathbf{r})] = \frac{\delta E_{\mathrm{xc}}[\rho]}{\delta \rho}$.

2.2.3 Exchange and correlation functionals

Even though the HK theorems and the KS mapping are exact, they merely replace one problem with another, as there is no exact expression for the exchange-correlation (XC) functional introduced in Eq. 2.34. The exchange energy arises due to the indistinguishability of electrons and the correlation energy describes the interaction of all electrons with one another. As such, the correlation energy is the most challenging term to describe accurately. Although the exchange energy can be calculated exactly for single particle orbitals, it is computationally expensive to compute for some particular basis sets and is often approximated. There exist various approximations for calculating the exchange and correlation energy. We present some of them here.

Local Density Approximation

The Local Density Approximation (LDA) is the simplest approximation to the exchange and correlation functional. The exchange and correlation energy associated with an infinitesimal volume of the system is approximated by the exchange and correlation energy of the same volume of a homogeneous electron gas

with an electron density equal to the density associated with the volume. In the limits of low density, the exchange-correlation energy per electron, $\varepsilon_{\mathrm{xc}}^{\mathrm{hom}}(\rho(\mathbf{r}))$, is known accurately from Quantum Monte-Carlo simulations (QMC) by Ceperley and Alder [18]; in the limits of high density, it can be calculated analytically. On the basis of a parametrized form [19,20] of $\varepsilon_{\mathrm{xc}}^{\mathrm{hom}}(\rho(\mathbf{r}))$, the XC energy functional is approximated as:

$$E_{\mathrm{xc}}^{\mathrm{LDA}}[\rho] = \int \rho(\mathbf{r})\varepsilon_{\mathrm{xc}}^{\mathrm{hom}}(\rho(\mathbf{r}))d\mathbf{r}. \tag{2.39}$$

The LDA has been successful for a number of systems. For instance, lattice constants for diamond, Si and Ge are predicted within 1% of experimental values [21], however, overbinding is typically seen, meaning energies are overestimated compared to experimental values. LDA is successful particularly where the density is uniform, but also for molecular or crystal systems. It is however limited by the approximations that go into it, and fails to capture the correct behaviour on some types of systems, for example hydrogen-bonded systems.

Gradient approximations

The next level of approximation is to expand the density in its gradients and higher order derivatives. The most commonly used form of such an expansion is the Generalised Gradient Approximation (GGA). GGA functionals are constructed in a way to satisfy a set of sum rules on the asymptotic behaviour of the functional. GGAs provide better atomisation and lattice constants but usually underbind, meaning the binding energies are underestimated compared to experiment. Some commonly used GGA functionals are the Perdew, Burke and Ernzerhof (PBE) [22], Perdew and Wang 91 (PW91) [23], BLYP [24], Wu and Cohen (WC) [25], PBEsol [26].

The general form for a GGA exchange and correlation functional is:

$$E_{\mathrm{xc}}[\rho] = \int \rho(\mathbf{r})F_{\mathrm{xc}}[\rho(\mathbf{r}), \nabla\rho(\mathbf{r}), \nabla^2\rho(\mathbf{r}), \ldots]d\mathbf{r} \tag{2.40}$$

where F_{xc} is called the enhancement factor, and all the gradients and higher order derivatives are encompassed by it. This approach is only semi-local.

The exchange part of a GGA functional can be written as:

$$E_{\mathrm{x}} = \int \varepsilon_x^{LDA} \rho(\mathbf{r}) F_{\mathrm{x}}(s) d\mathbf{r} \tag{2.41}$$

where $s = |\nabla\rho|/(2k_{\mathrm{F}}\rho)$ and $k_{\mathrm{F}} = (3\pi^2\rho)^{1/3}$. Different functionals use different enhancement factors that are physically motivated in various limits and approximations.

There are other types of functionals that go beyond the GGA such as meta-GGAs that include higher powers of the density gradient in the enhancement factor, up to fourth order, and hybrid functionals that combine Hartree-Fock exchange with DFT exchange. The Hartree-Fock (HF) method is a wavefunction-based method that uses one-electron orbitals and a mean potential in the Hamiltonian to calculate the energy of the system. With HF the exchange is calculated exactly, however it is more computationally costly as a method. Before the Hartree-Fock method, the Hartree method was proposed, where the total wavefunction of the system was taken to be simply a product of the one-electron orbitals. That form of course misses exchange, which the later developed HF method included by writing the total wavefunction of the system as a Slater determinant of one-electron orbitals. Correlation is not taken into account in either the Hartree or the Hartree-Fock method.

John Perdew classified the various functionals into levels of increasing sophistication [27] but also increasing computational cost, as follows:

- Hartree method
- LDA
- GGAs
- Meta-GGAs
- Hybrids
- Fully non-local

This "ladder" is used to demonstrate that the accuracy and computational efficiency are competing requirements and often one is at the cost of the other. Research on the field of electronic structure calculations is geared towards attempting to bridge that gap, by inventing methods that are accurate but also efficient. This is often very difficult to do for a general set of systems, so the focus is mainly on developing methods that perform well for a particular type of systems.

2.3 Solving the Kohn-Sham equations

In this section we briefly outline some ways which can significantly simplify the task of solving the KS equations (Eq. 2.37) computationally. First, the concept of basis sets is introduced, with focus on plane-wave basis sets. Next, Bloch's theorem for periodic systems and its uses are presented, followed by a basic discussion on how a plane wave basis is used in practice. Finally, an overview of the pseudopotential method is given.

2.3.1 Basis sets

Representing the one-electron orbitals in a particular basis rather than a three-dimensional grid is desirable as it can reduce the complexity of solving the KS equations. With an appropriate choice of basis the problem then comes down to, for instance, diagonalizing a matrix, or generally an easier task than solving N differential equations. There are various choices of basis sets: atomic orbitals; Gaussian basis, both used extensively in quantum chemistry approaches; plane waves (PW), used in a number of DFT packages.

The general expansion of a wavefunction $\psi_i(\mathbf{r})$ in a basis set $\{\phi_\alpha(\mathbf{r})\}$ is

$$\psi_i(\mathbf{r}) = \sum_\alpha c_{i\alpha}\phi_\alpha(\mathbf{r}) \tag{2.42}$$

Assuming the general case where the ϕ_α are not orthonormal, the Schrödinger equation (Eq. 2.37) may be cast into matrix form as

$$\sum_\alpha H_{\beta\alpha}c_{i\alpha} = \varepsilon_i \sum_\alpha S_{\beta\alpha}c_{i\alpha} \tag{2.43}$$

where $H_{\beta\alpha} = \langle\phi_\beta|\hat{H}|\phi_\alpha\rangle$ is the Hamiltonian matrix and $S_{\beta\alpha} = \langle\phi_\beta|\phi_\alpha\rangle$ is the overlap matrix, which for an orthonormal basis becomes the identity matrix.

2.3.2 Bloch's theorem

Before we move onto the discussion about the plane wave basis, it is important to mention Bloch's theorem [28]. Bloch's theorem states [29] that for a periodic external potential, i.e., one where $V(\mathbf{r}) = V(\mathbf{r}+\mathbf{R}_i)$, where $\mathbf{R}_i$ is a *lattice vector* of the unit cell, the wavefunction of an electron can be written as

$$\psi_{n\mathbf{k}}(\mathbf{r}) = e^{i\mathbf{k}\cdot\mathbf{r}}u_{n\mathbf{k}}(\mathbf{r}) \tag{2.44}$$

with

$$u_{n\mathbf{k}}(\mathbf{r}) = u_{n\mathbf{k}}(\mathbf{r} + \mathbf{R}_i). \tag{2.45}$$

The label $\mathbf{k}$ denotes the wave vector of the electron and n labels the band in question. Bloch's theorem has important implications, as it allows to treat periodic systems like perfect crystals very conveniently by taking advantage of the symmetries present in the system, thus enabling us to perform calculations of key quantities in a relatively simple manner. We show briefly how this can be done in the next section.

2.3.3 Plane waves

Because of Bloch's theorem, a plane wave basis is a natural choice for solid state systems, where a periodic external potential is present. Plane waves are solutions to the Schrödinger equation with a constant external potential. A great advantage of the PW basis is the fact that it is a complete basis and in practice can be systematically improved by using more plane waves in the representation of a wavefunction. Another advantage is the ease of switching between real and reciprocal space representations, by merely applying a Fourier transform, which for a PW basis requires $O(N \log N)$ operations.

Knowing from Eq. 2.45 that $u_{n\mathbf{k}}(\mathbf{r})$ is periodic, we can write it as a Fourier series:

$$u_{n\mathbf{k}}(\mathbf{r}) = \sum_n C_{n\mathbf{k},\mathbf{G}} e^{i\mathbf{G}\cdot\mathbf{r}}. \tag{2.46}$$

We can see that because of Eq. 2.44 we have $\exp(i\mathbf{G} \cdot \mathbf{R}_i) = 1$, which means that the only allowed values for $\mathbf{G}$ are the reciprocal lattice vectors $\mathbf{g}_i$, defined as:

$$\mathbf{g}_i = 2\pi\varepsilon_{ijk}\frac{\mathbf{R}_j \times \mathbf{R}_k}{\Omega} \text{ for } i \neq j \neq k \tag{2.47}$$

where ε_{ijk} is the Levi-Civita symbol and is equal to 1 for cyclic permutations of indices, -1 for anti-cyclic permutations, and 0 for any repeated indices, and Ω is the volume of the primitive cell.

The volume defined by the primitive reciprocal lattice vectors, $\Omega_{\mathrm{R}} = \mathbf{g}_1 \cdot (\mathbf{g}_2 \times \mathbf{g}_3)$, is called the first *Brillouin zone* (BZ).

A PW expansion for the wavefunction takes the form:

$$\psi_{n\mathbf{k}}(\mathbf{r}) = \sum_{\mathbf{G}} C_{n\mathbf{k},\mathbf{G}} e^{i(\mathbf{G}+\mathbf{k})\cdot\mathbf{r}}. \tag{2.48}$$

The problem of finding the energy eigenvalues of Eq. 2.37 then comes down to calculating the matrix elements of the kinetic operator and the effective potential operator in the PW basis, and diagonalising the Hamiltonian matrix obtained.

Considering a periodic system, we substitute the form for the eigenstates from Eq. 2.48 into Eq. 2.37, left-multiply by $e^{-i(\mathbf{G}'+\mathbf{k}')\cdot\mathbf{r}}$, integrate over $\mathbf{r}$ and use orthonormality of plane waves to obtain:

$$\sum_{\mathbf{G}}\left[\frac{|\mathbf{k}+\mathbf{G}|^2}{2}\delta_{\mathbf{G}+\mathbf{k},\mathbf{G}'+\mathbf{k}'}+\int V_{\text{eff}}(\mathbf{r})e^{-i(\mathbf{G}+\mathbf{k}-\mathbf{G}'-\mathbf{k}')\cdot\mathbf{r}}d\mathbf{r}\right]C_{n\mathbf{k},\mathbf{G}}=\epsilon_i C_{n\mathbf{k}',\mathbf{G}'}. \tag{2.49}$$

Note that $\delta_{\mathbf{G}+\mathbf{k},\mathbf{G}'+\mathbf{k}'}=\delta_{\mathbf{G},\mathbf{G}'}$ since for $\mathbf{k}\neq\mathbf{k}'$ it should vanish for any $\mathbf{G}$. Now by writing the periodic effective potential as a Fourier series $V_{\text{eff}}(\mathbf{r})=\sum_{\mathbf{G}}V_{\text{eff}}(\mathbf{G})e^{i\mathbf{G}\cdot\mathbf{R}}$ and recognizing that $V_{\text{eff}}(\mathbf{G})$ are the Fourier components of the expansion, we can write

$$\begin{aligned}\int V_{\text{eff}}(\mathbf{r})e^{-i(\mathbf{G}'+\mathbf{k}'-\mathbf{G}-\mathbf{k})\cdot\mathbf{r}}d\mathbf{r}&=\sum_{\mathbf{G}''}V_{\text{eff}}(\mathbf{G})\delta_{\mathbf{G}-\mathbf{G}',\mathbf{G}''}\\&=V_{\text{eff}}(\mathbf{G}-\mathbf{G}').\end{aligned}$$

Putting all this together we get

$$\sum_{\mathbf{G}}\left[\frac{|\mathbf{k}+\mathbf{G}|^2}{2}\delta_{\mathbf{G},\mathbf{G}'}+V_{\text{eff}}(\mathbf{G}-\mathbf{G}')\right]C_{n\mathbf{k},\mathbf{G}}=\epsilon_i C_{n\mathbf{k}',\mathbf{G}'}. \tag{2.50}$$

This is now the equation that has to be solved in order to calculate the total energy of the ground state; this is done by diagonalizing the Hamiltonian matrix

$$H_{\mathbf{G},\mathbf{G}'}(\mathbf{k})=\left[\frac{|\mathbf{k}+\mathbf{G}|^2}{2}\delta_{\mathbf{G},\mathbf{G}'}+\int V_{\text{eff}}(\mathbf{G}-\mathbf{G}')\right]. \tag{2.51}$$

Note that the computational cost of diagonalizing an $N\times N$ matrix is $O(N^3)$, which is the scaling of typical PW DFT codes. Even in the case of using grid methods, $O(N^3)$ scaling arises because orthonormality has to be imposed on the KS orbital pairs ($O(N^2)$) which involves calculating the integral $\int\psi_n^*(\mathbf{r})\psi_m(\mathbf{r})d\mathbf{r}$; because the KS orbitals are delocalized over the system, this leads to $O(N^3)$ scaling. The Fourier representation allows for the convenient calculation of the individual terms in V_{eff}: the Hartree potential V_{H}, external potential V_{ext} and

exchange-correlation potential V_{xc}. Since the evaluation of the Hartree and exchange-correlation potential involves the density, it also has to be expressed in reciprocal space, which is done using fast Fourier transforms (FFT). Sums of $\mathbf{G}$ are in practice evaluated up to a maximum value, $\mathbf{G}_{\text{max}}$, which is related to an energy cutoff through the dispersion relation $\epsilon = \frac{1}{2}|\mathbf{k} + \mathbf{G}|^2$. By increasing the cut-off energy in a simulation, the total energy decreases variationally.

It was assumed so far that the $\mathbf{k}$ vectors are continuous and span the Brillouin zone, but in practice both the $\mathbf{G}$ and the $\mathbf{k}$ vectors have to be discretized. The type of discretization for the $\mathbf{k}$ points has to be carefully chosen in order to appropriately and accurately sample the Brillouin zone. A widely used scheme to do this is the Monkhorst-Pack method [30]. The choice of a $\mathbf{k}$-point grid that includes the high-symmetry point $\mathbf{k} = 0$ only is termed "Γ-point sampling".

These same principles can be applied to aperiodic systems by using a *supercell*. In this case nothing changes in the way the calculations are performed and periodicity will still be present at the supercell level. However, there will be interactions between the periodic replicas of the system in the supercells, but they can be made negligible by choosing a large enough supercell. The energy calculated asymptotically converges to the energy of the isolated system as the supercell size is increased.

A disadvantage of the plane wave expansion is that a large number of plane waves is required to accurately represent the wavefunction near the nucleus because of the divergence of the Coulomb potential as $r \to 0$. In practice, this necessitates the representation of the bare nuclei with pseudopotentials.

2.3.4 Pseudopotentials

The core electrons generally don't contribute to the chemistry of a system because they are tightly bound to the nucleus, so it is desirable to replace the core electrons with a potential; this is called the *pseudopotential* approximation [31]. The motivation for using pseudopotentials is to reduce the number of electrons, and consequently the number of orbitals involved in a calculation. Moreover, by using a pseudopotential the PW basis set size will be reduced since the nodes of one-electron wavefunctions close to the nucleus require a large number of PW in order to maintain orthogonality; by replacing the core electrons with a smooth potential, the wavefunctions close to the nucleus no longer have nodes and therefore the number of PW will be reduced. The external potential near the nucleus is replaced by an effective smooth potential up to a chosen cut-off radius

r_c. The solution to the Schrödinger equation is therefore a *pseudo-wavefunction* and has no nodes in the core region. Note that semi-core states may be included as valence, in which case some of the wavefunctions will have nodes.

Pseudopotentials are usually generated in a stand-alone calculation for a single atom, using the exchange and correlation functional that is intended for the full calculation. This is done by first solving the all-electron problem for the single-particle orbitals and effective potential and then choosing which electrons will be used as valence electrons. Next, pseudo-orbitals are constructed from the all-electron orbitals and then the Schrödinger equation is inverted to determine the effective potential, which is now going to be smooth.

The construction of pseudopotentials should satisfy some properties: accuracy, in that the pseudo-wavefunctions have to have the same eigenvalues for the valence state as the all-electron ones; transferability, meaning that the accuracy should be maintained in different chemical environments in order for the pseudopotential to be suitable for use with various types of systems; softness, that is fast convergence of the energy with respect to the energy cutoff of the plane wave basis. Hamann *et al.* [32] showed that the requirement for pseudo-wavefunctions to be the same as the all-electron ones beyond the cut-off radius is that the integrals of their norm are the same in the core region. This is the norm conservation condition and also ensures preservation of scattering properties. One commonly used type of norm-conserving pseudopotential is given by the Troullier-Martins [33] (TM) scheme.

Ultrasoft pseudopotentials [34] allow the use of a low energy cut-off for the PW basis (therefore making the calculation more efficient) by relaxing the norm conservation requirement for core wavefunctions.

The quality of a pseudopotential is defined by a few factors: the agreement of the pseudo-orbital eigenvalues with the all-electron ones; the agreement of the pseudo-orbitals with the all-electron orbitals beyond the cutoff radius r_c; the integrated charge within the cutoff radius for the pseudo-orbitals should be the same as the one obtained with all-electron orbitals; derivatives of pseudo-orbitals should match derivatives of all-electron orbitals.

A generalization of the pseudopotential approximation is the projector augmented wave (PAW) method [35]. The concept behind it is that the all-electron wavefunction is decomposed in terms of a smooth pseudo-wavefunction everywhere, and a combination of all-electron and pseudo partial waves within a radially localized region (augmentation sphere) around each atom. This formalism offers the advantage that it combines the efficiency of the pseudopotential

approach while providing good accuracy.

Chapter 3

Dispersion Interactions in DFT

Dispersion interactions are long-range and attractive in nature, but are weaker than ionic or covalent bonding forces. Because of this non-local, long-range character of dispersion forces, traditional exchange-correlation functionals in DFT do not account for them. As a result, describing dispersion interactions in DFT has been and still remains a challenging topic.

There has recently been an increasing interest in van der Waals methods in DFT as shown by recent reviews [36–39], with a variety of new types of methods being developed and applied successfully to a broad range of systems. This is a fast-growing field, where many of the recent methods offering improved accuracy and computational efficiency indicate promising directions for future research and applications.

In this chapter, the nature of dispersion interactions is outlined, followed by a description and evaluation of the various methods to include dispersion in the DFT formalism.

3.1 Theory and formalism

Dispersion or van der Waals interactions are due to electronic density fluctuations of distant regions in space. At large distances, R, the expression for the van der Waals energy decays as $E_{\mathrm{vdW}} = -C_6/R^6$ and, as will be shown shortly, it is the energy of a spontaneous dipole-induced dipole interaction. The quan-

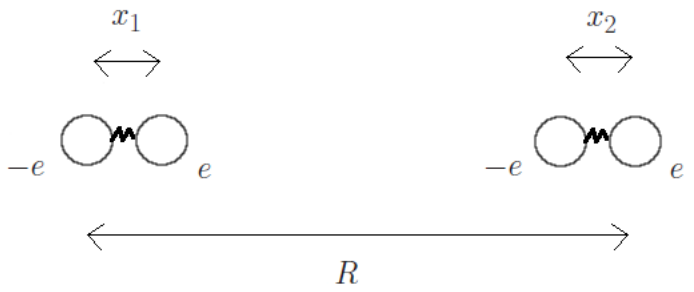


Figure 3.1: Depiction of the two simple harmonic oscillators with separations x_1 and x_2, separated by large distance $R >> x_i$. Each oscillator is comprised of two oscillating charges, of charge $\pm e$, connected by a harmonic spring.

tity C_6 is known as the vdW coefficient, or Hamaker constant [40]. There exist higher-order terms (C_8/R^8, C_{10}/R^{10}, etc) in the expansion, however here we will mainly focus on the C_6/R^6 contributions. It should also be noted that electromagnetic retardation is not considered when treating dispersion interactions in the formalisms that will be presented.

The term "van der Waals" interactions includes all possible combinations of dipole-dipole interactions: the interaction between two permanent dipoles, the interaction between a permanent and an induced dipole and the interactions between a spontaneous dipole with an induced dipole (i.e. London dispersion [41]), the latter being our main focus. However, the terms "van der Waals" and "dispersion" are often used interchangeably, particularly in the area of condensed matter physics.

3.1.1 A simple picture

A way to obtain some insight on the nature of van der Waals interactions from a classical picture is to consider two identical distant atoms at large separation R and treat them as simple harmonic oscillators, each with $\pm e$ charges connected by a harmonic spring (Fig. 3.1). This treatment, which we show here, adapted from Kittel [29] (page 53), is a very simplistic version of the coupled plasmon picture [42]. The physical motivation for this is that charge densities in reality fluctuate rather than remain static, and this causes spontaneous dipoles to appear on one atom, which then induce a dipole on another atom, leading to an interaction between them that is attractive in nature.

Considering the unperturbed system first, where the force constant is $C = m\omega_0^2$, ω_0 is the frequency of the strongest optical absorption line of the atom, x_i are the separations of the charges that are oscillating and p_i the momenta of the oscillators, we can write its Hamiltonian as:

$$H_0 = \frac{1}{2m}p_1^2 + \frac{1}{2}Cx_1^2 + \frac{1}{2m}p_2^2 + \frac{1}{2}Cx_1^2. \tag{3.1}$$

The Coulombic energy is given by:

$$H_1 = \frac{1}{R} + \frac{1}{R + x_1 - x_2} - \frac{1}{R + x_1} - \frac{1}{R - x_2} \tag{3.2}$$

Since $x_1/R << 1$ and $x_2/R << 1$, a polynomial expansion to second order (lowest non-zero order in this case) is used to approximate Eq. 3.2, leading to:

$$H_1 \approx -\frac{2x_1x_2}{R^3}. \tag{3.3}$$

Making a transformation for the modes in terms of symmetric and asymmetric ones we get

$$\begin{aligned} x_1 &= \frac{1}{\sqrt{2}}(x_s + x_a) \\ x_2 &= \frac{1}{\sqrt{2}}(x_s - x_a) \end{aligned} \tag{3.4}$$

for the coordinates and

$$\begin{aligned} p_1 &= \frac{1}{\sqrt{2}}(p_s + p_a) \\ p_2 &= \frac{1}{\sqrt{2}}(p_s - p_a) \end{aligned} \tag{3.5}$$

for the momenta. The total Hamiltonian, $H_0 + H_1$, can then be written in diagonal form:

$$\begin{aligned} H &= H_0 + H_1 \\ &= \big[\frac{1}{2m}p_s^2 + \frac{1}{2}(C - \frac{2}{R^3})x_s^2\big] + \big[\frac{1}{2m}p_a^2 + \frac{1}{2}(C + \frac{1}{R^3})x_a^2\big]. \end{aligned} \tag{3.6}$$

From this expression, two mode frequencies can be recognized:

$$\omega_s = \big[\frac{1}{m}\big(C - \frac{2}{R^3}\big)\big]^{1/2} \tag{3.7}$$

$$\omega_a = \big[\frac{1}{m}\big(C + \frac{2}{R^3}\big)\big]^{1/2}. \tag{3.8}$$

Expanding the frequencies to second order we get:

$$\omega_s = (C/m)^{1/2}\left(1 - \frac{2}{CR^3} - \frac{1}{8}\left(\frac{2}{CR^3}\right)^2\right) \tag{3.9}$$

$$\omega_a = (C/m)^{1/2}\left(1 + \frac{2}{CR^3} - \frac{1}{8}\left(\frac{2}{CR^3}\right)^2\right) \tag{3.10}$$

Now, considering the zero-point energy, $\frac{1}{2}(\omega_s + \omega_a)$, and remembering that $C = m\omega_0^2$ we finally find:

$$E_{\mathrm{vdW}} = -\omega_0 \frac{1}{8}\left(\frac{2}{C}\right)^2 \frac{1}{R^6}. \tag{3.11}$$

This is precisely in the well-known $E_{\mathrm{vdW}} = -C_6/R^6$ form.

The result from this approach is closely related with the one obtained from a coupled-fluctuation picture (see e.g. [43], [44]), in which $C_6 = K\omega_0\alpha_1\alpha_2$, where α_i are the dipolar polarizabilites of the two different atoms and K is a dimensionless constant. The physical argument in the coupled-fluctuation picture is that zero-point fluctuations result in a temporary fluctuating dipole arising in one atom, which then induces another dipole on the other atom. The average value of the energy of this interaction is estimated as

$$E = -\langle\big(\alpha_1 d_2 R^{-3}\big)\big(d_2 R^{-3}\big)\rangle \approx -C_6 R^{-6}. \tag{3.12}$$

From this, it can be clearly seen that there exists a relationship between the constant C in Eq. 3.11 and polarizability.

3.1.2 Multipole moments

Here we introduce the concept of multipole moments from classical electrostatics. They are useful as they allow us to write the electrostatic potential as an expansion and retain terms up to a given order. The expansion can be used to draw important conclusions about the form of electrostatic interactions. Consider a system of charges q_i with coordinates $\mathbf{r}_i$. The electrostatic potential due to this

system of charges, at position $\mathbf{R}$ is $\varphi(\mathbf{R})$. For large distances $|\mathbf{R}| = R >> |\mathbf{r}_i|$, the expansion of $\varphi(\mathbf{R})$ in terms of multipole moments is (see, e.g. Kaplan [45]):

$$\varphi(\mathbf{R}) = \sum_i \frac{q_i}{|\mathbf{R} - \mathbf{r}_i|} = \frac{\sum_i q_i}{R} + \frac{\mathbf{d} \cdot \mathbf{R}}{R^3} + \sum_{\alpha\beta} Q_{\alpha\beta} \frac{[\mathbf{R}]_\alpha [\mathbf{R}]_\beta}{R^5} \tag{3.13}$$

where $\mathbf{d}$ is termed the *dipole moment* and is given by:

$$\mathbf{d} = \sum_i q_i \mathbf{r}_i, \tag{3.14}$$

and $Q_{\alpha\beta}$ is the *quadrupole moment tensor*:

$$Q_{\alpha\beta} = \frac{1}{2} \sum_k q_k \left(3[\mathbf{r}_k]_\alpha [\mathbf{r}_k]_\beta - |\mathbf{r}_k|^2 \delta_{\alpha\beta} \right) \tag{3.15}$$

where $[\mathbf{r}_l]_\alpha$ denotes the α-th cartesian component of the position vector $\mathbf{r}_l$. This expansion will be used in the next section within the context of other approximations to estimate the form of dispersion interactions. Looking at Eq. 3.13 for the multipole moment expansion, we can see that symmetry will play an important role in determining which terms are dominant. In fact, it is known that the quadrupole moment tensor can *always* be cast into a diagonal form $Q_{\alpha\alpha}$ [45]. If the dipole moment of a system vanishes, the first leading term in the expansion is then given by the quadrupole moment. This can have important implications as we will see in the next section. A full discussion of symmetry and its importance related to multipole moments is beyond the scope of this thesis.

3.1.3 Quantum mechanical picture

Having shown the mathematical form of vdW interactions using a very simple classical picture, we need to turn to the quantum treatment of vdW in order to better understand them, as well as be able to integrate them into the electronic structure framework. We briefly outline London's approach [41] who was one of the first to work on dispersion interactions using quantum mechanics. In his work, London considered two neutral, widely separated hydrogen atoms in their ground state and used second-order perturbation theory to obtain the energy of interaction between the two atoms. Here we show we show how this was done, adapting from Mahanty and Ninham [46].

This system has two protons and two electrons, so its Hamiltonian, $\hat{H}$, may

be written as (disregarding nuclear kinetic terms):

$$\hat{H} = -\frac{1}{2}(\nabla_1^2 + \nabla_2^2) - \frac{1}{|\mathbf{r}_1|} - \frac{1}{|\mathbf{r}_2|} + \frac{1}{|\mathbf{R}_2 - \mathbf{R}_1|} - \frac{1}{|\mathbf{r}_1 - \mathbf{R}_2 - \mathbf{R}_1|} - \frac{1}{|\mathbf{r}_2 + \mathbf{R}_1 - \mathbf{R}_2|} - \frac{1}{|\mathbf{r}_1 - \mathbf{r}_2 - \mathbf{R}_1 - \mathbf{R}_2|} \tag{3.16}$$

where $\mathbf{r}_i$ are the electronic coordinates and $\mathbf{R}_i$ the nuclear coordinates. ∇_i acts only on system i. The transformation $\mathbf{r}_i \to \mathbf{r}_i - \mathbf{R}_i$ was made for the electronic coordinates so that their positions are defined in relation to the protons. We then write this Hamiltonian as the sum of two terms, $\hat{H} = \hat{H}_0 + \hat{V}_\mathrm{I}$, where $\hat{H}_0$ is the term on the first line of Eq. 3.16 and $\hat{V}_\mathrm{I}$ is the term on the second line. Based on the initial assumption that the two hydrogen atoms are widely separated, all the interactions between one atom with the other (electron-electron, nucleus-nucleus and electron-nucleus), which are encompassed by $\hat{V}_\mathrm{I}$. are treated as a perturbation. The $\hat{V}_\mathrm{I}$ Hamiltonian is then used as a perturbation Hamiltonian. Here we note the similarity of this approach with the simple model given in Sec. 3.1.1. The approach by London is of course much more sophisticated, but the underlying principles are fundamentally the same: now we are treating two well-separated atoms, where the negatively charged electron is "oscillating" around a positively charged nucleus of the same charge, and the two atoms interact weakly through $\hat{V}_\mathrm{I}$, which includes all the inter-atomic terms (c.f. Eq. 3.2), while the kinetic and intra-atomic interactions in $\hat{H}_0$ are the main contributions to the energy (c.f. Eq. 3.1).

We assume that the ground-state wavefunction is simply the product of the wavefunctions of the electrons on each hydrogen atom (this in fact means that we do not take electron exchange effects into account, which within the well-separated limit is a reasonable assumption[1]), so

$$\Psi_0(\mathbf{r}_1, \mathbf{r}_2) = \psi_{0(1)}(\mathbf{r}_1)\psi_{0(2)}(\mathbf{r}_2) = \frac{1}{\pi a_0^3} e^{(-|\mathbf{r}_1| - |\mathbf{r}_2|)/a_0}. \tag{3.17}$$

Using second order perturbation theory for, the perturbation to the ground

[1] This assumption, along with the particular decomposition of the Hamiltonian is called the polarization approximation [47]. Symmetry-adapted perturbation theory (SAPT) [48, 49] in fact addresses the drawbacks of this approximation and proposes a different formalism of perturbation theory which allows both the exchange and polarization effects to be taken into account.

state energy can be written as:

$$\Delta E = \langle \psi_{0(1)}\psi_{0(2)}|\hat{V}_{\rm I}|\psi_{0(1)}\psi_{0(2)}\rangle + \sum_{m,n\neq 0} \frac{|\langle \psi_{0(1)}\psi_{0(2)}|\hat{V}_{\rm I}|\psi_{m(1)}\psi_{n(2)}\rangle|^2}{(E_{0(1)} - E_{n(1)}) + (E_{0(2)} - E_{m(2)})}. \tag{3.18}$$

where $\psi_{n(i)}$ is the wavefunction of the i-th atom in an excited state n with energy E_n. Note that in this case $E_{n(1)} = E_{n(2)}$ and $E_{0(1)} = E_{0(2)}$ as we are treating two identical atoms.

Since the inter-atomic distance of this system is assumed to be large and the atoms are in the ground state, so there are no excitations, the radial extent of the electrons is much smaller than the inter-nuclear distance, so $|\mathbf{r}_i| << |\mathbf{R}_1 - \mathbf{R}_2|$. This condition makes it possible to perform a multipole moment expansion on $\hat{V}_{\rm I}$ in powers of $\frac{|\mathbf{r}_i|}{|\mathbf{R}_1 - \mathbf{R}_2|}$, up to the quadrupole moment term in Eq. 3.13. Defining the z-axis along the $\mathbf{R}_1 - \mathbf{R}_2$ direction[2] so that $\mathbf{R}_1 - \mathbf{R}_2 = R_{12}\hat{\mathbf{z}}$ and after some algebra, we find that the only term remaining is:

$$\hat{V}_{\rm I} = \frac{1}{R_{12}^3}\big(x_1x_2 + y_1y_2 - 2z_1z_2\big). \tag{3.19}$$

This now can be used in Eq. 3.18 to find the second order perturbation to the energy.

Using the perturbation Hamiltonian from Eq. 3.19 into Eq. 3.18, it is found that:

$$\Delta E = \frac{1}{R_{12}^6} \sum_{m,n\neq 0} \frac{|x_{1(0m)}x_{2(0n)} + y_{1(0m)}y_{2(0n)} - 2z_{1(0m)}z_{2(0n)}|^2}{2E_0 - E_m - E_n} \tag{3.20}$$

where $\mathbf{r}_{i(0m)} = \langle \psi_{0(i)}|\mathbf{r}_i|\psi_{m(i)}\rangle$ are matrix elements. Note that the first order correction has vanished.

Estimations of Eq. 3.20 [46] yield

$$\Delta E = E_{\rm disp} = -\frac{30a_0^5}{R_{12}^6} \tag{3.21}$$

which is in the well-known form of vdW interactions. We see that the dispersion energy is in the form $E_{\rm disp} = -C_6/R^6$; we call C_6 the *dispersion coefficients*.

London found that Eq. 3.20 can be cast in terms of *oscillator strengths*, f_{lm},

[2]Recall from Sec. 3.1.2 that by an appropriate choice for the coordinate system, the quadrupole moment tensor can be made diagonal; in fact in this case by choosing $\mathbf{R}_1 - \mathbf{R}_2$ along the z-axis, only Q_{33} terms remain.

which are defined by

$$f_{lm} = \frac{2}{3}(E_m - E_l)|\mathbf{d}_{lm}|^2 \tag{3.22}$$

and $\mathbf{d}_{lm} = |\langle l|\mathbf{d}|m\rangle|$ are the matrix elements of the dipole moment. The oscillator strengths describe transitions between states, $|l\rangle \rightarrow |m\rangle$. Oscillator strengths satisfy a sum rule

$$\sum_m f_{lm} = N \tag{3.23}$$

where this is valid $\forall\ l$ that are substates of m, and where N is the total number of electrons of the system.

Here we will state three different forms for C_6 coefficients, who's starting point is

$$E_{\text{disp}} = \frac{3}{2R^6}\sum_{m,n}\frac{f_{0m}f_{0n}}{[(E_m - E_0)(E_n - E_0)][(E_0 - E_m)(E_0 - E_n)]}. \tag{3.24}$$

This form is obtained from Eq. 3.20 using the definition of oscillator strengths. It is a useful form since the oscillator strengths are known from experiment by looking at the intensities of spectral lines.

London showed that for two molecules separated by distance R with strong transitions at frequencies ω_1 and ω_2 and number of electrons N_1 and N_2, respectively, Eq. 3.24 becomes

$$C_6 = \frac{3}{2}\frac{N_1 N_2}{\omega_1\omega_2(\omega_1 + \omega_2)}. \tag{3.25}$$

The number of electrons comes into the equation by using the summation rule for the oscillator strengths from Eq. 3.23.

Slater and Kirkwood [50] showed that:

$$C_6 = \frac{3}{2}\frac{\alpha_1(0)\alpha_2(0)}{(\alpha_1(0)/N_1)^{1/2} + (\alpha_2(0)/N_2)^{1/2}} \tag{3.26}$$

where α is the *dynamic polarizability* defined as

$$\alpha(\omega) = \sum_{n\neq 0}\frac{f_{0n}}{\omega_{n0}^2 - \omega^2} \tag{3.27}$$

and ω are again transition frequencies.

Finally, Casimir and Polder [51] showed that

$$C_6 = \frac{3}{\pi}\int_0^\infty \alpha_1(i\omega)\alpha_2(i\omega)d\omega. \tag{3.28}$$

A commonly used approach for calculating dispersion interaction energies is then to find expressions for C_6 coefficients using experimentally or computationally determined *free-atom* polarizabilties. However, other than for the case of two well-separated atoms, one cannot use the real free-atom polarizabilities; instead an *effective* expression has to be found taking into account the fact that when atoms are in a molecule, the chemical environment changes, which results in changes of their effective polarizabilities. One then obtains different C_6 for every pair of density fragments and pairwise-sums over all of them to obtain the dispersion energy. Other methods rely on using experimentally or computationally determined free-atom dispersion coefficients and then taking a geometric mean to calculate C_6 coefficients between two different atoms or molecules. We will review the aforementioned types of methods in Sec. 3.4.

Having seen the approach by London, we may say that this picture demonstrates that van der Waals interactions are dipole-dipole interactions and arise from density fluctuations, considering each hydrogen atom is a dipole of $\pm e$ charge. We can also draw the conclusion that vdW interactions are a quantum effect, where the aforementioned density fluctuations are in fact zero-point energy fluctuations. Even though what London demonstrated is based on two distant hydrogen atoms, it is still valid for general systems: the first-order perturbation term in Eq. 3.18 will always vanish, and the leading order term in Eq. 3.19 for the multipole expansion of the perturbation Hamiltonian will always be of the R^{-3} order, thus leading to a R^{-6} interaction.

3.1.4 Dispersion energy

All these concepts and approaches introduced by London can be generalized to any two separated systems; in more complex cases anisotropic effects are also present, but the principles are the same. For two widely separated molecules, A and B, with ground state wavefunctions Ψ_0^A and Ψ_0^B, the energy correction to second order perturbation theory, representing polarization interactions, is given by:

$$E_{\text{pol}} = -\sum_{n\neq 0 \wedge m\neq 0} \frac{|\langle \Psi_n^A \Psi_m^B | \hat{V} | \Psi_0^A \Psi_0^B \rangle|^2}{(E_n^A - E_0^A) + (E_m^B - E_0^B)} \tag{3.29}$$

where $n \neq 0 \wedge m \neq 0$ means that n and m cannot simultaneously take the value 0, and $\Psi_n^{A/B}$ are excited states. The polarization energy can be written as the sum of two parts; the induction energy and the dispersion energy:

$$E_{\text{pol}} = E_{\text{ind}} + E_{\text{disp}}. \tag{3.30}$$

This is in fact the definition of dispersion.

The induction energy is given by:

$$E_{\text{ind}} = -\sum_{m\neq 0} \frac{|\langle \Psi_0^A \Psi_m^B | \hat{V} | \Psi_0^A \Psi_0^B \rangle|^2}{E_m^B - E_0^B} - \sum_{n\neq 0} \frac{|\langle \Psi_n^A \Psi_0^B | \hat{V} | \Psi_0^A \Psi_0^B \rangle|^2}{E_n^A - E_0^A}. \tag{3.31}$$

The first term in the sum represents the electrostatic interaction of molecule A in its ground state with density $\rho_{00}^A(\mathbf{r})$, with molecule B in an excited state m with density $\rho_{m0}^A(\mathbf{r})$. The second term is defined in the same manner. For overlapping charge distributions, the induction interactions are important, however due to their exponential decay with distance for non-polar atoms or molecules, they carry no significance at large distances [45].

For the same molecules A and B, the dispersion part of the energy which we have already visited for the special case of two distant hydrogen atoms, is defined by:

$$E_{\text{disp}} = -\sum_{m\neq 0, n\neq 0} \frac{|\langle \Psi_n^A \Psi_m^B | \hat{V} | \Psi_0^A \Psi_0^B \rangle|^2}{(E_n^A - E_0^A) + (E_m^B - E_0^B)}. \tag{3.32}$$

More generally, following a perturbative approach in the spirit of London's work by using Eq. 3.32 for molecules or fragments of electronic density A and B and performing a multipole expansion for the perturbation Hamiltonian $\hat{V}$, the energy of vdW interactions can be estimated. Including higher-order terms in the multipole expansion for $\hat{V}$, the dispersion energy can be written as:

$$E_{\text{disp}} = -\sum_{n=6}^{\infty} \frac{C_n}{R^n}. \tag{3.33}$$

Note that $n = 6$ is the first non-vanishing term in the expansion is valid for general systems. The higher-order terms in the expansion in Eq. 3.33 can contain either exclusively even powers (for spherically symmetric systems) or both even and odd powers for more complex systems like molecules. As previously mentioned, the first term of Eq. 3.33 is the basis for a number of approaches aiming to calculate vdW interactions which involve finding appropriate expressions for

the C_6 coefficients and pairwise-summing over interacting non-overlapping fragments of density in the system. The perturbative types of approaches shown here cannot be used for overlapping fragments (molecules or atoms) since the initial assumption is that the two interacting systems are well separated and electron exchange was thereby ignored as was done for the simple case of hydrogen atoms.

3.2 Adiabatic connection - fluctuation dissipation theorem

Adiabatic connection - fluctuation dissipation theorem (ACFD) methods [52–55] are based on the *exact* expression for the exchange-correlation energy:

$$E_{\mathrm{xc}} = -\int_0^1 d\lambda \int_0^\infty \frac{du}{2\pi} \int\int d\mathbf{r} d\mathbf{r}' \frac{1}{|\mathbf{r}-\mathbf{r}'|}\big(\chi_\lambda(\mathbf{r},\mathbf{r}',iu) - \chi_0(\mathbf{r},\mathbf{r}',iu)\big) \quad (3.34)$$

where ω is the frequency and χ is the *density response function*, and represents how the density changes when the external potential V is varied. In mathematical terms

$$\chi(\mathbf{r},\mathbf{r}') = \frac{\delta\rho(\mathbf{r})}{\delta V(\mathbf{r}')}. \quad (3.35)$$

The density response functions can be determined from single-particle orbitals. The parameter λ in Eq. 3.34 determines how close the system is to the fully interacting one. For $\lambda = 0$, we have a non-interacting system while for $\lambda = 1$ we have the fully interacting one. χ_0 is the bare density response function, while χ_λ is the interacting one. An expression exists for χ_λ:

$$\chi_\lambda = \chi_0 + \chi_0\Big(\frac{\lambda}{|\mathbf{r}-\mathbf{r}'|} + f_{\mathrm{xc}}^\lambda\Big) \quad (3.36)$$

where f_{xc}^λ is called the *exchange-correlation kernel*. Eq. 3.34 encompasses all correlation effects, and as a result vdW interactions are automatically included. However, solving this equation corresponds to solving the full many-body problem, and is unfeasible for realistic systems, unless an approximation to the exchange-correlation kernel is found. ACFD provides the starting point for a range of other methods, such as random phase approximation [56] (RPA) approaches.

3.2.1 RPA methods

The RPA types of approaches [57–60] are based on approximating the correlation functional starting from the ACFD expression for the exchange-correlation energy, while the exchange term is treated either exactly or in some other approximation. In RPA, the exchange-correlation kernel from Eq. 3.36 is set to zero. Expressions for the density response functions are obtained based on the single-electron orbitals used and Eq. 3.34 is evaluated. The integral is typically reduced to a Casimir-Polder type of formula (Eq. 3.28). RPA approaches are considered the most sophisticated approximation to the correlation energy in DFT [37], offering a *seamless*[3] treatment of dispersion interactions and very good accuracy for lattice constants and bulk moduli of solids [61]. The calculations, however, are computationally expensive and are not performed self-consistently and also can be sensitive to the input orbitals. The lack of efficiency of RPA methods is therefore their weakness. The scaling of RPA methods depends on the implementation and is within the range $O(N^4) - O(N^6)$ [60, 62].

3.3 Quantum chemical methods

Quantum chemical methods are part of electronic structure family of methods. As opposed to DFT, these methods work with wavefunctions. The treatment is all-electron, which means all the electrons in the system are taken into account, and there is no substitution of a number of electrons by an approximating potential, like in the case of pseudopotential methods often used in DFT.

One such method is the configuration interaction (CI) [16, 63] method. It uses a trial wavefunction which is a sum of the ground-state HF determinant and a finite number of determinants for excited states. The excited determinants can include singles (S), doubles (D), triples (T), quadruples (Q), etc. A "single" means one electron has been excited to any higher-energy unoccupied state, "double" means two electrons have been excited to any higher-energy unoccupied state etc.

When all possible determinants are included in the calculation, it is called a full CI method. It can be made arbitrarily accurate by increasing the basis set size, M. The highest level of truncated CI is in practice CISDTQ (includes up to quadruples) and is very close to full CI. It is, however, extremely compu-

[3] By seamlessness we mean a treatment of vdW in a continuous manner, not strictly for non-overlapping, distant fragments of density.

tationally expensive, with a $O(M^{10})$ scaling. For a CISD (singles and doubles) the cost is $O(M^6)$, which is still very demanding. While the accuracy of these methods is very high, the down-side of them is clearly the poor computational efficiency.

Another family of methods are perturbative approaches, such as coupled-clusters [64] (CC) method and Møller-Plesset (MP) [65]. The coupled-clusters method is similar in spirit to CI, in that the HF ground state is used, only in this method the singles, doubles, etc are treated as perturbations, using many-body perturbation operators. CCSD(T), (T) meaning that triples are treated approximately, is considered the "gold standard" in terms of accuracy, however the computational cost is once more very high ($O(M^8)$). Typically systems of no more than 50 atoms [66] can be treated because of computational bottlenecks. The accuracy level is dependent on the basis sets, but even within that, excellent accuracy is achieved. For example, binding energies for the benzene dimer agree with experiment within 0.1-0.3 kcal/mol [67, 68].

Møller-Plesset theory uses the Hartree-Fock Hamiltonian for the unperturbed system and adds a perturbation to it. The MP2 approach goes up to second order in perturbation theory and, as a result, encompasses vdW interactions to some extent. Because of its relatively better scaling ($O(M^5)$), it offers a middle ground between accuracy and efficiency, but it is generally not used as a benchmark as they overestimate binding energies compared to CCSD(T) [69]. The method termed "MP2+vdW" by Tkatchenko *et al.* [70] corrects for vdW in MP2 and yields excellent accuracy, at the same computational cost as the underlying calculation.

Generally, quantum chemical methods offer great accuracy but at high computational cost and as a result may be applied only to small systems. CCSD(T) is used for benchmarking, and is the method of preference to compare against when testing the accuracy of other methods.

3.4 DFT Methods

A number of methods for vdW in DFT exist, with varying degrees of accuracy and computational cost. Some methods are valid for specific types of systems, while others are able to describe dispersion more generally. Most of the methods are based on estimating the interatomic C_6 coefficients in various ways. However, more sophisticated methods exist which include higher order terms in the sum in

Eq. 3.33, such as the coupled-fluctuating dipole model [71] (CFDM), calculations of interatomic C_6 and higher-order dispersion coefficients using an exchange-hole dipole moment approach [72–75] or time-dependent DFT (TDDFT) [76–78]. There are also semi-empirical pseudopotential methods [79–81] to include dispersion in the form of the pseudopotential used.

Here we will mainly focus on pairwise treatment of density fragments, involving the $n = 6$ term in Eq. 3.33, either in an empirical way or through a density functional. The main types of approaches are presented here and their advantages and disadvantages in terms of accuracy, physical motivation and efficiency are discussed. A brief discussion of non-additivity is given first.

3.4.1 Non-additivity

One of the issues encountered with simplistic approaches such as treating pairwise fragments of density is what is called "non-additivity": it describes non-additive effects arising when a collection of particles is treated instead of just two well-separated fragments of density. Three types of such effects have been recognized by Dobson [36, 82]:

• Type A: Because of the electronic cloud overlap being compressed by the presence of positive nuclei as well as by possible Pauli effects, the electrons may be less polarizable and the dispersion energy is reduced compared to having had sums of free atoms. This type of non-additivity is generally not a problem for any method.

• Type B: When a polarizable atom is present in the vicinity of a second atom, Coulomb screening occurs and the response of the second atom to fluctuations of a third one, is changed (the interaction can either be reduced or enhanced).

• Type C: When there is degeneracy that favours significant fluctuations in electronic density by electron hopping between neighbouring atoms, large dipoles may be induced, which may increase the dispersion interaction. For three-dimensional metals, this effect is tamed by type B non-additivity, but is more pronounced in two or one-dimensional metals.

Type A is included in all methods that will follow, whereas type B is only part of a few, while type C is encompassed only in very advanced and computationally expensive methods, such as RPA.

3.4.2 DFT+D

The class of methods referred to as dispersion-corrected (DFT-D or DFT+D) methods [83–88] correct the energy obtained from a DFT calculation by adding an interatomic vdW interaction with *semi-empirical* C_6 coefficients in the form of a pairwise sum

$$E_{\mathrm{vdW}} = -\sum_{i>j} f_{\mathrm{damp}}(r_{ij}) C_{6ij} r_{ij}^{-6} \tag{3.37}$$

where i, j label the atoms, $r_{ij} = |\mathbf{r}_i - \mathbf{r}_j|$ is the distance between the atoms and $f_{\mathrm{damp}}(r)$ is a damping function introduced to account for the singular behaviour of r^{-6} terms at short distances. The various schemes of these types of methods make use of different damping functions. The interatomic C_{6ij} coefficients are calculated from the homoatomic coefficients C_{6i}, using quantities known from experiment, or *ab initio* calculations. For example, Grimme *et al.* [84] calculate the homoatomic dispersion coefficients through ionization potentials and static polarizabilities known from computational calculations, and then take the geometric mean to calculate $C_{6ij} = \sqrt{C_{6i} C_{6j}}$. Other methods [86] use a variation of the London formula (Eq. 3.25) for the C_6 coefficients, given by:

$$C_{6ij} = \frac{3}{2} \alpha_i \alpha_j \frac{I_i I_j}{I_i + I_j} \tag{3.38}$$

where I_i are ionization potentials and α_i the polarizabilities as usual. In a similar way, the interatomic vdW radii appearing in the damping functions are calculated from the homoatomic ones.

These types of methods have the advantage of good accuracy in the calculation of binding energies and equilibrium separations for intermolecular interactions at the same computational cost as the DFT calculation. One of the most widely used methods by Grimme *et al.* [84] yields intermolecular interactions within 15-20% error for energies and 0.1-0.2 Å for equilibrium separations. The great disadvantage is the fact that the dispersion energy does not depend on the real density of the system. Moreover, at least two empirical parameters are required (for example ionization potential and polarizability) for each atom. Fitting of other parameters is often performed in some methods [89] (dispersion coefficients as well as parameters involved in the damping function), by varying the parameters and identifying the values which yield the minimum energy within a given energy functional. That requires additional effort and introduces further dependence of the methods on parameters.

A more recent work by Grimme *et al.* [87] involves the use of dispersion coefficients calculated *ab initio* with time-dependent DFT, and also takes into account the fact that the dispersion coefficients change when an atom is in a molecule. This makes the dispersion coefficients dependent on the environment, which is not the case in other DFT+D methods. In this work, they also considered three-body interactions, but they seem to worsen the agreement with the S22 set slightly. Type A and B non-additivity effects are then partly included in this method. In general, however, neither type A, B or C are well-described by most DFT+D schemes.

3.4.3 DFT+vdW

In DFT+vdW types of methods, C_6 coefficients are calculated from the electronic density and a correction is again added in the same way as in Eq. 3.37 (for most of them). With the exception of one method that also takes into account type B non-additivity, DFT+vdW approaches only include Type A additivity. This is due to the fact that many-body effects are not taken into account.

Andersson-Langreth-Lundqvist 1996

The Andersson, Langreth and Lundqvist (ALL) method [90] is based on considering two distant perturbations in a uniform electron gas to describe the asymptotic part of vdW interactions, and therefore does not provide a seamless treatment of dispersion. Like most available methods, this one also treats dispersion interactions pairwise. Starting from the expression for the interaction between two distant small charge perturbations [91] Andersson, Langreth and Lundqvist obtained an expression for the effective long-range electron interaction in a similar manner to Ashcroft and Rapcewicz [92], by choosing an effective density, ρ_{eff}, of the form

$$\rho_{\text{eff}} = \left[\sqrt{\rho(\mathbf{r}_1)\rho(\mathbf{r}_2)}\left(\sqrt{\rho(\mathbf{r}_1)} + \sqrt{\rho(\mathbf{r}_2)}\right)\right]^{2/3} \tag{3.39}$$

to approximate the uniform density of the medium, where $\rho(\mathbf{r}_i)$ is the density at $\mathbf{r}_i$. This form for the density yields an effective long-range interaction of the form

$$\phi(\mathbf{r}_1, \mathbf{r}_2) = -\frac{-3}{2\omega_p(\mathbf{r}_1)\omega_p(\mathbf{r}_2)[\omega_p(\mathbf{r}_1) + \omega_p(\mathbf{r}_2)]|\mathbf{r}_1 - \mathbf{r}_2|^6} \tag{3.40}$$

where

$$\omega_p(\mathbf{r}_i) = \sqrt{4\pi\rho(\mathbf{r}_i)} \tag{3.41}$$

is the local plasma frequency at the position of electron i.

Integrating Eq. 3.40 over $\mathbf{r}_1$ and $\mathbf{r}_2$, the correlation energy of two widely separated fragments of matter is obtained:

$$E_{\rm xc}^{\rm l-r} = -\frac{3}{\pi}\int_0^\infty du \int_{V_1} d\mathbf{r}_1 \int_{V_2} d\mathbf{r}_2 \frac{\chi_1(iu)\chi_2(iu)}{|\mathbf{r}_1 - \mathbf{r}_2|^6} \tag{3.42}$$

where $\chi(\omega)$ is the electric susceptibility (or polarization response) of a uniform electron gas of density $\rho(\mathbf{r})$, given by

$$\chi(\omega) = \frac{1}{4\pi}\frac{\omega_p^2}{\omega_p^2 - \omega^2}. \tag{3.43}$$

Writing $E = -\frac{C_6}{R^6}$ for Eq. 3.42, the Casimir-Polder expression from Eq. 3.28 is recovered for the C_6 coefficient, after making use of the definition of the atomic polarizabilities $\alpha_i(\omega) = \int d\mathbf{r}_i \chi_i(\omega)$. It is noted that the approximation for the polarizability is a local one. Finally, by integrating Eq. 3.42 over the complex frequencies u and combining Eq. 3.41 with Eq. 3.43, the following density-dependent expression for the long-range interaction between two separated fragments of matter is obtained:

$$E_{\rm xc}^{\rm l-r} = \frac{6}{4(4\pi)^{3/2}}\int_{V_1} d\mathbf{r}_1 \int_{V_2} d\mathbf{r}_2 \frac{\sqrt{\rho_1(\mathbf{r}_1)\rho_2(\mathbf{r}_2)}}{\sqrt{\rho_1(\mathbf{r}_1)} + \sqrt{\rho_2(\mathbf{r}_2)}} \frac{1}{|\mathbf{r}_1 - \mathbf{r}_2|^6}. \tag{3.44}$$

A short-range cutoff has to be imposed in this integral, obtained by equating the length scale for density change to the electron gas screening length. Using the expressions for the Fermi velocity and plasma frequency, $v_{\rm F} = \hbar(3\pi^2\rho_n(r))^{1/3}$ and $\omega_{\rm p} = (4\pi\rho_n(r))^{1/2}$ respectively, the cutoff radius can be determined from the fact that

$$\frac{6\rho_n(r)}{|\nabla\rho_n(r)|} = \frac{v_{\rm F}}{\omega_p}. \tag{3.45}$$

The performance of this method in terms of calculating interatomic and intermolecular C_6 coefficients is good overall yielding, 6-10% for some cases and up to 40% disagreement in the worst cases, against reference values; the results are sometimes sensitive to the cutoff. Another disadvantage of this method is the high computational cost of the integral in Eq. 3.42 if evaluated directly.

Silvestrelli's method

Silvestrelli's method [1, 7, 93] follows the ALL approach and further simplifies the calculation of the integral in Eq. 4.13. It involves partitioning the density in terms of Maximally Localized Wannier Functions (MLWFs), and then replacing each of those with a hydrogenic orbital with a well-defined analytic form that is parametrized by the centre and spread of the MLWF it replaces. The ALL integral is then reduced to a simple two-dimensional integral evaluated up to a radial cutoff, thus greatly reducing the computational cost of the method. The vdW energy is then calculated by pairwise summation over all the "fragments" of the system, namely the charge densities associated with each orbital, and is added to the total energy computed by the underlying DFT calculation.

Advantages of this method are computational efficiency and simplicity of the physical picture. However, some disadvantages are that the *real* density of the system is not used in the calculation of the vdW contribution to the total energy, since the total charge density associated with the hydrogenic orbitals is not equal to the electronic density of the system, an extra parameter (a radial cutoff) is introduced, and there can be an ambiguity associated with symmetry-equivalent choices of MLWFs for systems exhibiting some degree of rotational symmetry. Its accuracy is not particularly good for simple dimer systems compared to CCSD(T) values. A very detailed analysis of the method, as well as a number of improvements to it are given in Ch. 4.

Tkatchenko-Scheffler methods

2009 The Tkatchenko-Scheffler [94] (TS) approach starts from the exact expression of the Casimir-Polder formula (Eq. 3.28) and expands the polarizabilities in a Padé series. They make use of free-atom reference values for interatomic C_6 coefficients and static polarizabilities (it therefore has some empirical character). For two atoms, A and B, they obtain an expression for the inter-atomic dispersion coefficients, C_{6AB}, in relation to the homoatomic coefficients C_{6AA} and C_{6BB}:

$$C_{6AB} = \frac{2C_{6AA}C_{6BB}}{\frac{\alpha^0_B}{\alpha^0_A}C_{6AA} + \frac{\alpha^0_A}{\alpha^0_B}C_{6BB}} \tag{3.46}$$

where $\alpha^0_{A/B}$ are the static polarizabilities of A/B. Both dispersion coefficients and static polarizabilities are taken from time-dependent DFT calculations. By utilizing Hirshfeld partitioning [95] for the density, they obtain expressions for *effective* homoatomic coefficients in a molecule, C^{eff}_{6AA}. Using Eq. 3.46 they

obtain the interatomic effective coefficients, which are used in an expression as Eq. 3.37 along with an appropriate damping function to calculate the extra vdW energy. A Fermi-like damping function is used, with vdW radii defined by the effective volume (and therefore implicitly dependent on the electronic density). This method performs very well, with an error of 8% for binding energies and 0.1 Å for equilibrium separations. Molecular C_6 coefficients are also calculated by adding all the inter-atomic effective dispersion coefficients; comparison of atomic and molecular coefficients calculated with the TS approach against reference data yields a mean average relative error 5.5%. This method has the same computational cost of the underlying DFT calculation.

2012 A more recent method developed by Tkatchenko and Sheffler [96] further improves the accuracy of calculations by taking into account many-body effects [97] and going beyond just pairwise summation, using the coupled fluctuating dipole model [71] and treating coupled quantum harmonic oscillators. This improves its accuracy since screening and interacting pairs of fluctuating dipoles are also taken into account. This method is now regarded as one of the most accurate methods in DFT, without any significant additional computational cost of a standard DFT calculation. Mean absolute relative errors compared to CCSD(T) are at or less than 5% for all types of systems, even outside the S22 set [69], making this method an excellent candidate for studying a broad range of systems. Both type A and B non-additivity are included in this scheme, which is a very encouraging direction towards establishing a family of methods that are well physically motivated, accurate and efficient.

3.4.4 vdW-DF

The class of methods known as vdW-DF [98–103] consist of finding a non-local contribution to the exchange-correlation functional used in a DFT calculation.

These methods are based on making various approximations to the adiabatic connection formula (Eq. 3.34) written as [101].Calculating Eq. 3.34 is a computationally heavy operation, so approximations have to be made. More details on the physical justifications behind the approximations, as well as the approximations themselves will be discussed in Ch. 5. As for most methods, while type A non-additivity is encompassed in vdW-DF, type B and C non-additivity are not, since this is a two-body method and many-body effects are absent.

Many vdW-DF methods were developed on this basis, initially for specific

types of systems, such as surfaces and slabs, and in general layered structures [101, 104]. Recently a van der Waals functional for general geometries was proposed [9] which includes vdW interactions in a seamless way, that is for both short distances where the overlaps of charge density between the interacting fragments should be taken into account, and also for long distances in which the non-local long-range effects not typically represented in traditional DFT should be considered. The 2004 version by Dion *et al.* [9] is the well-recognized "vdW-DF", which many more recent variations that followed are based on. The initial version did not include the potential for the functional, but the implementation by Thonhauser *et al.* [105] made the method self-consistent; in fact, it was found that for the systems studied, the self-consistency had very little impact on binding curves of vdW-bound dimers.

The correlation energy is divided into two parts:

$$E_{\mathrm{c}}[\rho] = E_{\mathrm{c}}^{0}[\rho] + E_{\mathrm{c}}^{\mathrm{nl}}[\rho] \tag{3.47}$$

with the simplest form of the non-local correlation energy being

$$E_{\mathrm{c}}^{\mathrm{nl}} = \frac{1}{2}\int\int d\mathbf{r}d\mathbf{r}'\rho(\mathbf{r})\rho(\mathbf{r}')\phi(\mathbf{r},\mathbf{r}') \tag{3.48}$$

where $\phi(\mathbf{r},\mathbf{r}')$ is called the *kernel*, and depends on $\mathbf{r}-\mathbf{r}'$ and the densities ρ in the vicinity of $\mathbf{r}$ and $\mathbf{r}'$. This form is clearly not exact, and treats all interactions pairwise, which, as mentioned earlier, is the basis of most methods for dispersion in DFT. The two parts to the correlation energy are treated in different approximations; E_{c}^{0} is treated within the LDA. Exchange is treated within GGA, so the total exchange-correlation functional becomes:

$$E_{\mathrm{xc}}[\rho(\mathbf{r})] = E_{\mathrm{x}}^{\mathrm{GGA}}[\rho(\mathbf{r})] + E_{\mathrm{c}}^{\mathrm{LDA}}[\rho(\mathbf{r})] + E_{\mathrm{c}}^{\mathrm{nl}}[\rho(\mathbf{r})] \tag{3.49}$$

Only type A non-additivity is encompassed by vdW-DF methods, since by construction only two-body effects are taken into account.

The great advantage of this method is that it is *ab initio* with no empirical parameters required and provides a seamless treatment of dispersion interactions. However, the accuracy of the original form of vdW-DF is not particularly good compared to other methods, with errors of 20-30% for intermolecular energies and 0.3-0.4 Å for equilibrium separations. This is largely due the fact that the exchange functional used in Eq. 3.49 is revPBE [106] in the original Dion

et al. [9] method, and revPBE is known to overbind, due to its repulsive nature near the equilibrium separation. Attempting to correct this unsatisfactory behaviour of the original vdW-DF, a number of modifications of vdW-DF in terms of the exchange, as well as the non-local part of correlation were developed, with significant improvements for a range of systems. The following modifications to the method appeared in 2010:

• Cooper *et al.* [107] proposed an alternative GGA functional which reduces the short-range exchange repulsion. It yields great improvements both on intermolecular separations and energies.

• Lee *et al.* [10] proposed an alternative exchange and non-local correlation functional. Significant improvements over the original vdW-DF were brought by this alternative version of the vdW-DF, named vdW-DF2. The agreement with CCSD(T) quantum chemical calculations is much better for most systems studied with the vdW-DF2. The vdW-DF2 scheme differs only in terms of the energy, given by:

$$E_{\rm xc}[\rho(\mathbf{r})] = E_{\rm x}^{\rm rPW86}[\rho(\mathbf{r})] + E_{\rm c}^{\rm PW92}[\rho(\mathbf{r})] + E_{\rm c}^{\rm nl}[\rho(\mathbf{r})] \tag{3.50}$$

The exchange functional used is the refitted version of PW86 (Perdew-Wang 1986) [108], by Murray *et al.* [109], but now the non-local correlation functional is also changed; details are discussed in Ch. 5, Sec. 5.4.

• Klimeš *et al.* [11] explored a variety of exchange functionals, to be used in Eq. 3.49, with "chemical" accuracy (within 1 kcal/mol for energies) for a wide range of systems, both dispersion and hydrogen bonded. The functionals were optimized for the S22 set. They termed the various functionals as "F-vdW" where F is the name of the optimized exchange energy, e.g. optPBE-vdW, optB88-vdW etc. These alternative vdW-DF flavours will be discussed in detail in Ch. 5.

One question that may arise is how appropriate is it to use pseudopotentials generated with a particular exchange-correlation functional with a particular type of vdW-DF that uses a different exchange functional. Ikutaro *et al.* [110] found that while this may yield slightly different binding energy curves, it is not a significant difference and does not present a major problem. It is, however, suggested that pseudopotentials generated with a GGA are used, since in the various vdW-DF versions, the exchange functionals are obtained from a GGA.

The initial implementations [9, 105] of the method (both non self-consistent and self-consistent), were still computationally expensive, since Eq. 3.48 involves

a six-dimensional spatial integral. Román-Pérez and Soler's implementation [2] made the calculation of this integral, as well as the calculation of the non-local potential much more efficient, at virtually the same accuracy as the original functional. This algorithm is currently being used for most implementations of the vdW-DF in various packages. A more complete overview of Soler's implementation will be given in Ch. 5.

Vydrov and Van Voorhis

Vydrov and van Voorhis have also worked on vdW-DF type approaches [111–114], leading up to the so-called VV10 [115], that uses more complicated expressions for the kernel ϕ in Eq. 3.48. An efficient implementation of VV10, following a Soler-type of implementation has been proposed by Sabatini *et al.* [116]. In the VV implementation, a more complicated and sophisticated expression for the kernel from Eq. 3.48 is calculated.

There exist two VV10 variants that were compared in a recent benchmarking assessment [117]; comparisons showed improved binding energies for various types of weak bonding, as well as hydrogen bonds, using the alternative variant. This suggests that the alternative VV10 may be a better option overall if one chooses to use this method. Potential implementation of this method in ONETEP will be discussed in Ch. 7.

In conclusion, the nature of dispersion interactions was discussed, and various ways to understand them were presented. An overview of methods to include vdW in DFT was given, and a brief assessment of their efficiency, accuracy and applicability was given. In general, very accurate methods are computationally expensive, but a very good level of accuracy can be achieved with methods that are computationally efficient. Two of the methods discussed here (the method of Silvestrelli and vdW-DF) will be discussed in more detail in Ch. 4 and Ch. 5, respectively.

Chapter 4

Dispersion interactions with maximally localized Wannier functions

In this chapter, we explore the parameters and approximations involved in Silvestrelli's method [93] and improve its results where possible by modifying various aspects of the method [7]. We apply the method and our proposed modifications to a series of test systems, then to two more challenging systems, a phthalocyanine and a copper phthalocyanine dimer. We thus demonstrate that although this method can offer an easily implementable and computationally efficient way of calculating the dispersion correction to the energy with the possibility of improved accuracy (once some modifications are applied to it), it is largely dependent on a number of parameters and choices one can make.

In Sec. 4.1 we review the necessary background theory relating to MLWFs and Silvestrelli's method; in Sec. 4.3 we highlight some of the problems with the method as it stands and describe our improvements; in Sec. 4.4 we present and discuss results for vdW-corrected total energies and equilibrium geometries obtained by applying these methods to a series of dimer systems and compare to quantum chemical coupled-cluster (CCSD(T)) and semi-empirical vdW (DFT+D) approaches; finally, in Sec. 4.6 we draw our conclusions.

4.1 Wannier functions

Wannier functions [118] are orthogonal localized functions that span the same space as the eigenstates of a single particle Hamiltonian. They are particularly useful as they provide a better understanding of the chemical properties of a system related to bonding. Consider the set of N_{occ} occupied (valence) eigenstates $\{|u_m\rangle\}$ of a molecule (c.f. Eq. 2.44). The total energy of the system is invariant with respect to unitary transformations among the eigenstates

$$|w_n\rangle = \sum_{m=1}^{N_{\text{occ}}} U_{mn}|u_m\rangle. \tag{4.1}$$

If the unitary matrix $\mathbf{U}$ is chosen such that the resulting N_{occ} orbitals $\{w_n(\mathbf{r})\}$ minimize their total quadratic spread, given by

$$\Omega = \sum_n \left(\langle w_n|r^2|w_n\rangle - \langle w_n|\mathbf{r}|w_n\rangle^2\right) = \sum_n \left(\langle r^2\rangle_n - \bar{\mathbf{r}}_n^2\right), \tag{4.2}$$

then they are said to be maximally-localized Wannier functions [6] (MLWFs). Each MLWF has an associated quadratic spread, S_n^2, and a centre, $\bar{\mathbf{r}}_n$.

In the construction of MLWFs it is sometimes useful to consider not only the valence manifold but also a range of unoccupied eigenstates above the Fermi level — often those constituting the antibonding counterparts to the valence states. This not only allows the MLWFs to be more localized [119, 120] but can also restore symmetries that would otherwise be broken arbitrarily through the construction of MLWFs for the valence manifold only; we will revisit this point later.

In order to do so, one defines an outer energy window, E_{win}, consisting of $N_{\text{win}} \geq N_{\text{occ}}$ states, from which one may extract or "disentangle" an optimal N_{dis}-dimensional subspace ($N_{\text{win}} \geq N_{\text{dis}} \geq N_{\text{occ}}$) using the disentanglement approach described in Ref. [121], to find the relation between the optimal states of the disentangled manifold, to the original KS states:

$$|u_m^{\text{opt}}\rangle = \sum_{p=1}^{N_{\text{win}}} U_{pm}^{\text{dis}}|u_p\rangle, \tag{4.3}$$

where $\mathbf{U}^{\text{dis}}$ is a rectangular $N_{\text{win}} \times N_{\text{dis}}$ unitary matrix. N_{dis} MLWFs may then

be localized by suitable rotation of the optimal subspace in the usual manner:

$$|w_n^{\rm dis}\rangle = \sum_{m=1}^{N_{\rm dis}} U_{mn}|u_m^{\rm opt}\rangle. \tag{4.4}$$

or, in terms of the Bloch states:

$$|w_n^{\rm dis}\rangle = \sum_{m=1}^{N_{\rm dis}}\sum_{p=1}^{N_{\rm win}} U_{mn}U_{pm}^{\rm dis}|u_p\rangle. \tag{4.5}$$

Furthermore, an inner, or *frozen*, energy window may be defined if one wishes to make certain that a range of low-lying eigenstates is included in the optimal subspace, for example, the occupied states. Algorithms for determining ML-WFs from the eigenstates obtained from electronic structure calculations are implemented within the Wannier90 software package [122].

The single-particle density operator is given by

$$\hat{\rho} = \sum_{n=1}^{N_{\rm occ}} |u_n\rangle\langle u_n|. \tag{4.6}$$

It can also be written in terms of the $N_{\rm occ}$ fully-occupied valence MLWFs $|w_n\rangle$ or, equivalently, in terms of a larger set of $N_{\rm dis}$ disentangled MLWFs, $|w_n^{\rm dis}\rangle$. This set of disentangled MLWFs span more than just the occupied subspace, but by using a suitable frozen/inner window in the disentanglement procedure, they can be made to span the occupied subspace only. We can then write

$$\hat{\rho} = \sum_{n=1}^{N_{\rm occ}} |w_n\rangle\langle w_n|, \tag{4.7}$$

$$= \sum_{k,l=1}^{N_{\rm dis}} f_{kl}^w |w_k^{\rm dis}\rangle\langle w_l^{\rm dis}|, \tag{4.8}$$

where we have substituted Eq. 4.1 and Eq. 4.5, respectively, into Eq. 4.6, and where the occupancy matrix is given by

$$f_{kl}^w = \sum_{p=1}^{N_{\rm occ}}\sum_{m,s=1}^{N_{\rm dis}} U_{ml}U_{pm}^{\rm dis}U_{sk}^{*}U_{ps}^{*\rm dis}. \tag{4.9}$$

Note that these occupancies are non-diagonal.

Now defining the density $\rho(\mathbf{r}) = \langle\mathbf{r}|\hat{\rho}|\mathbf{r}\rangle$, we can write it as a sum of diagonal

$(l = k)$ and off-diagonal $(l \neq k)$ terms,

$$\begin{aligned}\rho(\mathbf{r}) &= \sum_{l=1}^{N_{\text{dis}}} f_{ll}^{w} |w_l^{\text{dis}}(\mathbf{r})|^2 + \sum_{l \neq m}^{N_{\text{dis}}} f_{lm}^{w} w_l^{*\text{dis}}(\mathbf{r}) w_m^{\text{dis}}(\mathbf{r}), \\ &\equiv \rho_{\text{D}}(\mathbf{r}) + \rho_{\text{OD}}(\mathbf{r}). \end{aligned} \tag{4.10}$$

It is important to note that in this form, $\rho_D(\mathbf{r})$ alone integrates to the number of valence electrons N, because the mutual orthogonality of the MLWFs ensures $\int \rho_{\text{OD}}(\mathbf{r}) d\mathbf{r} = 0$.

In the case of MLWFs obtained from the manifold of occupied states only $(N_{\text{dis}} = N_{\text{occ}})$, the occupancy matrix is simply the identity matrix, $f_{kl} = \delta_{kl}$, and the charge density in terms of the MLWFs is simply given by

$$\rho(\mathbf{r}) = \sum_{n=1}^{N_{\text{occ}}} |w_n(\mathbf{r})|^2. \tag{4.11}$$

It is worth noting that in the case of spin-degenerate systems, the occupancies must be scaled by a factor of 2.

We have adapted the Wannier90 code to calculate the occupation matrices, and can choose to make a *diagonal* approximation to the density by retaining only the first term of Eq. 4.10. The effect of approximating the true density with the diagonal approximation will be discussed later in Sec. 4.4.9 in the context of the improvements, described in Sec. 4.3, to Silvestrelli's method.

4.2 Silvestrelli's method

The main idea behind the method by Silvestrelli consists of first decomposing the density into fragments via MLWFs (note that this is not a unique decomposition), and then approximating them with hydrogenic s-orbitals of the same centre and spread as the real MLWFs, which then interact pairwise.

4.2.1 Original MLWF approach

Silvestrelli's approach [1,93] is based on the Andersson, Langreth and Lundqvist [90] (ALL) expression for the vdW energy in terms of pairwise interactions

between density fragments $\rho_n(\mathbf{r})$ and $\rho_l(\mathbf{r}')$, separated by a distance r_{nl},

$$E_{\mathrm{vdW}} = -\sum_{n>l} g_{nl}(r_{nl}) \frac{C_{6nl}}{r_{nl}^6}, \tag{4.12}$$

where $g_{nl}(r_{nl})$ is a damping function [93] which screens the unphysical divergence of Eq. 4.12 at short range, and

$$C_{6nl} = \frac{3}{4(4\pi)^{3/2}} \int_V d\mathbf{r} \int_{V'} d\mathbf{r}' \frac{\sqrt{\rho_n(\mathbf{r})\rho_l(\mathbf{r}')}}{\sqrt{\rho_n(\mathbf{r})} + \sqrt{\rho_l(\mathbf{r}')}}, \tag{4.13}$$

in atomic units. It should be noted that these expressions are only strictly valid in the limit of non-overlapping density fragments. There are various forms for the damping function [123, 124] that might have a slight short-range effect but should not affect the long-range behaviour of the vdW energies. Here we choose to use the damping function as proposed in the original paper by Silvestrelli [1].

Now, in accord with Eq. 4.11, the MLWFs obtained from the valence orbitals of a system provide a localized decomposition of the electronic charge density, such that $\rho_n(\mathbf{r}) = |w_n(\mathbf{r})|^2$, so that Eq. 4.13 becomes

$$C_{6nl} = \frac{3}{32\pi^{3/2}} \int_{|\mathbf{r}|\leq r_c} d\mathbf{r} \int_{|\mathbf{r}'|\leq r_c'} d\mathbf{r}' \frac{|w_n(\mathbf{r})||w_l(\mathbf{r}')|}{|w_n(\mathbf{r})| + |w_l(\mathbf{r}')|}, \tag{4.14}$$

where r_c is a suitably chosen cutoff radius obtained by equating the length scale for density change to the electron gas screening length [93]:

$$\frac{6\rho_n(r_c)}{|\nabla\rho_n(r_c)|} = \frac{v_F[\rho_n(r_c)]}{\omega_p[\rho_n(r_c)]} \tag{4.15}$$

which leads to

$$r_c = S_n\sqrt{3}(0.769 + \frac{1}{2}\ln(S_n)). \tag{4.16}$$

In order to make the calculation of the integrals more tractable, the charge density is approximated by replacing each MLWF $w_n(\mathbf{r})$ with a hydrogenic s-orbital that has the same centre $\bar{\mathbf{r}}_n$ and spread S_n as the MLWF, and whose analytic form is is given by

$$w_n^{\mathrm{H}}(\mathbf{r}) = \frac{3^{3/4}}{\sqrt{\pi}S_n^{3/2}} e^{-\sqrt{3}|\mathbf{r}-\bar{\mathbf{r}}_n|/S_n}, \tag{4.17}$$

which, on substitution into Eq. 4.14 and after some algebra, gives

$$C_{6nl} = \frac{S_n^{3/2} S_l^3}{2 \cdot 3^{5/4}} F(S_n, S_l), \tag{4.18}$$

where

$$F(S_n, S_l) = \int_0^{x_c} dx \int_0^{y_c} dy \frac{x^2 y^2 e^{-x} e^{-y}}{e^{-x}/\beta + e^{-y}}, \tag{4.19}$$

$\beta = (S_n/S_l)^{3/2}$, $x_c = \sqrt{3} r_c / S_n$ and $y_c = \sqrt{3} r_c' / S_l$. Whereas evaluating Eq. 4.14 using the true MLWFs requires a computationally demanding six-dimensional numerical integration, Eq. 4.19 may be evaluated easily since it is only a two-dimensional integral that depends solely on the MLWF spreads and centres, not on their detailed shapes or orientations.

We note that in the case of a spin-degenerate system, since every MLWF is doubly occupied, the density of each fragment must be multiplied by a factor of 2 and, therefore, the C_{6nl} integral in Eq. 4.14 must be scaled by a factor of $\sqrt{2}$.

4.2.2 Recent work

This method has been applied to a variety of systems, from small molecules [1], small molecules on surfaces [125], small water clusters [126] to studying adsorption of rare-gas atoms on surfaces [127]. Recently, a number of improvements to the method have been implemented. In 2012, Ambrosetti and Silvestrelli [128] used an alternative expression for the C_6 coefficients. The rest of the method is then in the same spirit as the original one described here, in that it uses MLWFs to partition the density and pairwise interactions are summed. Overall improvement of C_6 coefficients against experimental results is reported compared to the original method for a number of dimers. In 2013, they proposed a scheme whereby screening effects were included [129]. They report greatly improved C_3 coefficients for the adsorption of small molecules on metal surfaces compared to experimental data when screening effects are taken into account. In the most recent method, Silvestrelli [130] adopts a much more sophisticated approach, in the spirit of the recent Tkatchenko-Scheffler scheme [96] that includes many-body effects by treating coupled harmonic oscillators. With the new method, errors for the S22 set are significantly reduced compared to previous versions of the method, and performance on other systems is overall improved.

4.3 Improvements

The approximations that go into the method described in the previous Section will clearly not always hold, and the need to examine them is clear. In this Section, we introduce our enhancements [7] to the original method by Silvestrelli [93] that address some of its drawbacks and analyse limitations carefully.

4.3.1 Partly Occupied Wannier Functions

Using a manifold of eigenstates that includes but is larger than the subspace spanned by just the valence states results in partly-occupied MLWFs that are generally more localized and that better reflect the symmetries of the system, as opposed to MLWFs obtained by rotation of the valence subspace only, which arbitrarily break the symmetry (we will demonstrate examples of this phenomenon in Sec. 4.4).

In order to account for the partial occupancy of the MLWFs, we make a slight modification to Silvestrelli's approach, explicitly introducing occupancies in the definition of the C_{6nl} integral from Eq. 4.18; since in the diagonal approximation, the density of each fragment is now given by $\rho_n(\mathbf{r}) = f^w_{nn}|w_n(\mathbf{r})|^2$, the expression for $F(S_n, S_l)$ in Eq. 4.19 becomes

$$F(S_n, S_l) = \int_0^{x_c} dx \int_0^{y_c} dy \frac{x^2 y^2 e^{-x} e^{-y}}{e^{-x}/(\beta\sqrt{f^w_{nn}}) + e^{-y}/\sqrt{f^w_{ll}}}, \tag{4.20}$$

where the f^w_{nn} are given by Eq. 4.9. We will see in Sec. 4.4 that this seemingly simple idea can give rise to a marked improvement in the accuracy of the method.

4.3.2 Modification to describe p-like states

MLWFs describing only the valence manifold often take the form of well-localized sigma-orbitals centred on a bond between two atoms, and are thus reasonably well-described by the approximation of replacing them with a suitable s-orbital. When anti-bonding states are included in the construction of the MLWFs, the resulting orbitals have more atomic-orbital character. This is demonstrated by the atom-centred p-like MLWF shown in Fig. 4.1. It is clear that the density associated with such an MLWF will not be very well represented by a single s-like function at its centre. In order to approximate p-like orbitals appropriately when calculating the vdW coefficients, C_6, one could imagine using a suitably-oriented analytic expression for a hydrogenic p-orbital, for example, a canonical

p_z-orbital given by

$$p_z(\mathbf{r}) = \frac{30^{5/4} r \cos\theta}{\sqrt{32\pi} S^{5/2}} e^{-\sqrt{30}r/2S}, \tag{4.21}$$

which has been normalized such that its quadratic spread is $\langle p_z|(\mathbf{r}-\bar{\mathbf{r}})^2|p_z\rangle = S^2$; θ is the polar angle in spherical polar coordinates. As a consequence of the explicit angular dependence, using this function in Eq. 4.14 would give rise to four-dimensional integrals for which analytic solutions are not readily available. Numerical evaluation of these integrals for realistic systems would be prohibitively computationally expensive. We solve this problem by identifying the p-like MLWFs in the system and replacing them with the hydrogenic form given in Eq. 4.21. Then, we further approximate each lobe (lower and upper) of this p-like orbital with two separate hydrogenic s-orbitals of the form of Eq. 4.17. In order to do so, for each of the upper (+) and lower (−) lobes of the orbital, it is necessary to know the spread $S_\pm$ and centre $\bar{\mathbf{r}}_\pm$, given by the following integral, where ϕ is the azimuthal and θ the polar angles in polar coordinates:

$$S_\pm^2 = \int_0^\infty \int_0^{\pi/2} \int_0^{2\pi} r^4 p_z^2(\mathbf{r}) \sin\theta dr d\theta d\phi, \tag{4.22}$$

$$\bar{\mathbf{r}}_\pm = \bar{\mathbf{r}} \pm \int_0^\infty \int_0^{\pi/2} \int_0^{2\pi} r^3 \cos\theta\, p_z^2(\mathbf{r}) \sin\theta dr d\theta d\phi\, \hat{\mathbf{z}}, \tag{4.23}$$

which, after some algebra, simplifies to

$$S_\pm = \frac{7S}{8\sqrt{2}}, \tag{4.24}$$

$$\bar{\mathbf{r}}_\pm = \bar{\mathbf{r}} \pm \frac{15S}{8\sqrt{30}}\, \hat{\mathbf{z}}, \tag{4.25}$$

where $\bar{\mathbf{r}}$ and S are the original centre and spread, respectively, of the true MLWF. The choice of the upper and lower limit on θ in 4.24 is such that only the upper (or, equivalently, lower because of symmetry) lobe centre and spread are calculated. These expressions may be easily generalized to arbitrary orientations of the symmetry axis of a p-like state by rotating the offset vectors $(\bar{\mathbf{r}}_\pm - \bar{\mathbf{r}})$ accordingly.

Thus, we have developed a formalism whereby the charge density due to MLWFs with p-like character can be represented by a pair of s-like hydrogenic orbitals with appropriate centres and spreads. In Sec. 4.4 we will show how this works in practice for calculating vdW energy corrections.

In the high-symmetry systems studied in this work, the p-like orbitals are

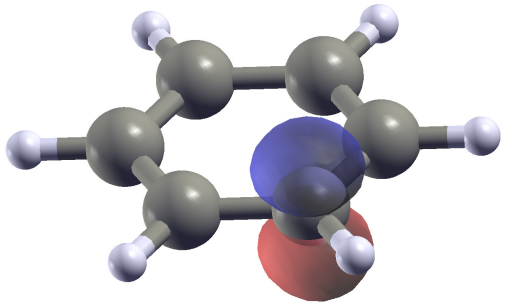


Figure 4.1: Partly occupied p-like orbital on benzene molecule. In the method described here, each of the two lobes (coloured red and blue) is replaced by an s orbital and considered a separate fragment.

easily distinguished from other orbitals by their partial occupancies, given by Eq. 4.9, which are typically closer to 0.5 rather than 1. Alternatively, and especially for structurally more complex systems, the shape of each MLWF could be characterized using the efficient method described in App. A of Ref. [131] as another means of automating the procedure of identifying p-like functions.

4.3.3 Symmetry Considerations

Minimizing the total spread Ω with respect to the elements of the unitary matrix $\mathbf{U}$, and thus producing MLWFs, has the effect of picking from the space of all possible unitary matrices one which produces the most localized Wannier functions accessible through optimization from a chosen initial guess. This is often enough to uniquely determine the MLWFs. In some cases, however, it does not give rise to a unique choice, even if the optimization procedure is perfect. For example, the atomic positions and electron density of the system may possess certain symmetry elements, such as rotations about a particular axis. Then there will exist a number of equally valid and degenerate representations of the MLWFs and their centres, which give the same spread, and are related by symmetry. The minimization procedure breaks the symmetry by choosing one of these representations; in other words there will be a degree of arbitrariness in the final MLWFs. It is clear from Eq. 4.12 that any degree of non-uniqueness of the centres will cause an undesirable variability of the vdW energy calculated in Silvestrelli's method. This is indeed what we observe in some of the examples shown in the following sections. Moving away from a description of the MLWFs

using the valence states only, and towards using partly occupied MLWFs that include anti-bonding states and which retain the symmetries of the system, enables us to overcome these problems, as we demonstrate in Sec. 4.4.2.

4.4 Applications

4.4.1 Calculation Details

For the application of Silvestrelli's method to the following atomic and molecular dimer systems we used the Quantum Espresso (QE) package [132] to perform the ground-state DFT calculations, and Wannier90 [122] to obtain the centres and spreads of the MLWFs, in a post-processing step. Our results are compared to both the semi-empirical DFT+D method [84, 133] as implemented in QE, which is expected to give good asymptotic behaviour, and CCSD(T) calculations, which are considered the 'gold-standard' of quantum chemistry, by Janowski *et al.* [68].

The PBE [22] generalized-gradient approximation for exchange and correlation was used for all cases, except in the case of argon where the revPBE [106] functional was used. Norm-conserving pseudopotentials and Γ-point sampling of the Brillouin zone were used throughout. We note that we have chosen to use revPBE for the argon system since PBE produces significant binding in rare gas dimers as it overestimates the long-range part of the exchange contribution [9, 134, 135]. For all the other systems studied here, however, PBE does not cause spurious binding and would therefore normally be considered an appropriate functional. A plane-wave basis set cut-off energy of 80 Ry was used in all calculations with QE except for the case of the phthalocyanine and copper phthalocyanine where a 50 Ry energy cutoff was used. For the dimers of argon, methane, ethene, phthalocyanine and copper phthalocyanine, cubic simulation cells of length 15.87 Å, 15.87 Å, 21.16 Å and 23.81 Å, respectively, were used. For the dimers of benzene, a hexagonal cell with $a = 15.87$ Å and $c = 31.75$ Å was used. For all the systems, the choice of energy windows when using the disentanglement procedure in Wannier90 for our modified method was as follows: inner (frozen) energy windows were chosen to include all the valence states; outer energy windows ranged from the lowest eigenvalue of the system, ε_0, to a maximum of $E_{\text{win}} = \varepsilon_{\text{LUMO}} + \alpha(\varepsilon_{\text{HOMO}} - \varepsilon_0)$, where $\varepsilon_{\text{HOMO}}$ is the energy of the highest occupied valence Kohn-Sham (KS) state and $\varepsilon_{\text{LUMO}}$ is the energy of the lowest unoccupied KS state. The factor $\alpha = 0.4$ was chosen to

scale down the valence energy bandwidth, used to estimate the energy difference required above the LUMO when including anti-bonding states. We discuss the sensitivity of the method to this factor in Sec. 4.4.10.

Initial guesses, or "projections" for the MLWF centres and orbital characters are typically specified in Wannier90 to ensure realistic centres, as it is sometimes possible that the spread is minimized, but centres are delocalized over the cell. This relates to the issues discussed in Sec. 4.3.3.

4.4.2 Argon

We will first investigate the severity of the aforementioned issues relating to symmetry (Subs. 4.3.3), by considering the case of an argon dimer. Optimization of the MLWFs describing a single argon atom produces four doubly occupied MLWFs arranged tetrahedrally around the atom (Fig. 4.2). Due to spherical symmetry, the orientation of these MLWFs with respect to a given coordinate system is arbitrary for an isolated atom and the final MLWFs obtained will depend on the initial guess used. In the dimer, this arbitrariness is removed, at least in principle, since the spherical symmetry is broken by the presence of the other atom at a specific orientation. At large separations, this is not in practice necessarily the case: the electron density overlap between the Ar atoms is vanishingly small, since the wavefunctions decay exponentially away from the atom. Therefore, to within attainable numerical precision, the orientation of the MLWFs on each atom is uncorrelated with the orientation of the other atom: the MLWFs can be freely rotated with respect to the atom without affecting the total spread. Note, however, that since the vdW energy only decays as R^{-6}, its value *is* influenced by the orientation of the MLWF centres (and hence their separation) out to distances beyond which the calculated spread (and thus the optimized MLWF orientation) has ceased to be sensitive to separation.

This dependence can be investigated in a two-atom system by fixing the relative orientations of the MLWF centres between the two atoms in the dimer. This is achieved by first calculating the MLWF centres for a single atom of argon and then translating and rotating these centres to the second Ar atom with various choices of alignment. We will refer to this approach as the *fragment method*. In this method, we calculate the dispersion correction to the energy for a dimer system using various possible arrangements of MLWF centres on the other atom. Three possible high-symmetry choices are shown in Fig. 4.2. For each of these orientations, Fig. 4.4 (top) shows the binding energy of the Ar

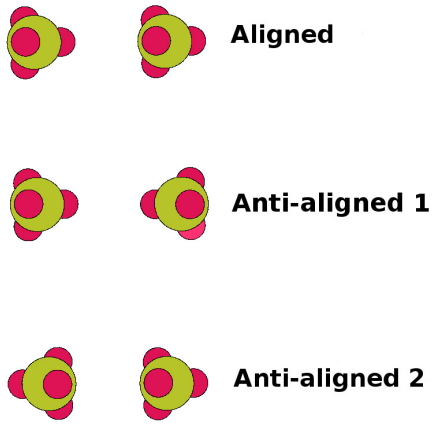


Figure 4.2: Illustration of three of the many possible configurations of MLWF centres (small pink spheres) for the two argon atoms (large yellow spheres) in the fragment method.

dimer as the separation of the atoms varies. We see that there is considerable displacement of the curves, and the binding energy and the equilibrium separation change according to the alignment chosen by up to 0.04 kcal/mol and 0.08 Å, respectively.

In contrast to this fragment approach, in Fig. 4.4 (bottom) we show the binding energy as calculated with the normal approach of using the optimized MLWFs of the entire dimer system. However, here we have used varying initial guesses corresponding to the set of possible alignments shown in Fig. 4.2. We see that at small separations, the MLWF centres always converge to the same positions, regardless of the initial guess, and the binding energy curve is nearly independent of the choice of initial guess ($\sim 10^{-3}$ kcal/mol variation).

At larger separation, however, the spread minimization is insufficiently sensitive to the relative orientation of the MLWFs on different atoms, and does not necessarily alter it from the initial guess, resulting in several different possible results depending on the initial orientation of the centres. If a random initial guess is chosen, then the energy varies discontinuously, as a function of separation, within the bounds imposed by the limiting cases described using the fragment method. This is because the MLWF centres converge to different orientations depending on their starting positions (curve labelled 'random' in Fig. 4.4 (bottom)). It should be noted that there are no variational principle ar-

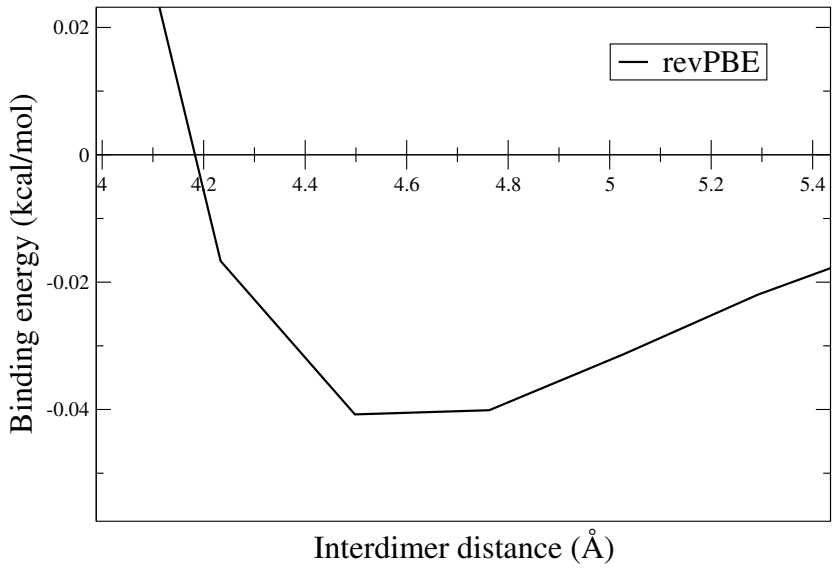


Figure 4.3: Binding energy curve for the argon dimer with revPBE. Note that revPBE barely binds, yielding a very low energy of -0.04 kcal/mol and a large equilibrium separation compared to CCSD(T) values, so inclusion of dispersion corrections is necessary.

guments that would ensure that lower energies are any more correct than higher ones.

In order to avoid this problem of non-uniqueness of binding energy curves, a random initial guess is used first for a configuration at small separation, in the knowledge that the result will be independent of the guess used. Then the MLWF centres computed at the previous, smaller separation are used as the initial guess for the calculation at a larger separation. In this manner, a unique continuous curve is obtained (labelled 'continuous' in Fig. 4.4 (bottom)). This is the approach that we adopt for all subsequent calculations in this work.

From the continuous curve, we obtain 3.97 Å for the equilibrium separation and -0.28 kcal/mol for the binding energy. This is in good agreement with the coupled cluster CCSD(T) calculations of Ref. [136], which give 3.78 Å and -0.28 kcal/mol, respectively, whereas revPBE without dispersion corrections gives 4.61 Å and -0.04 kcal/mol (Fig. 4.3).

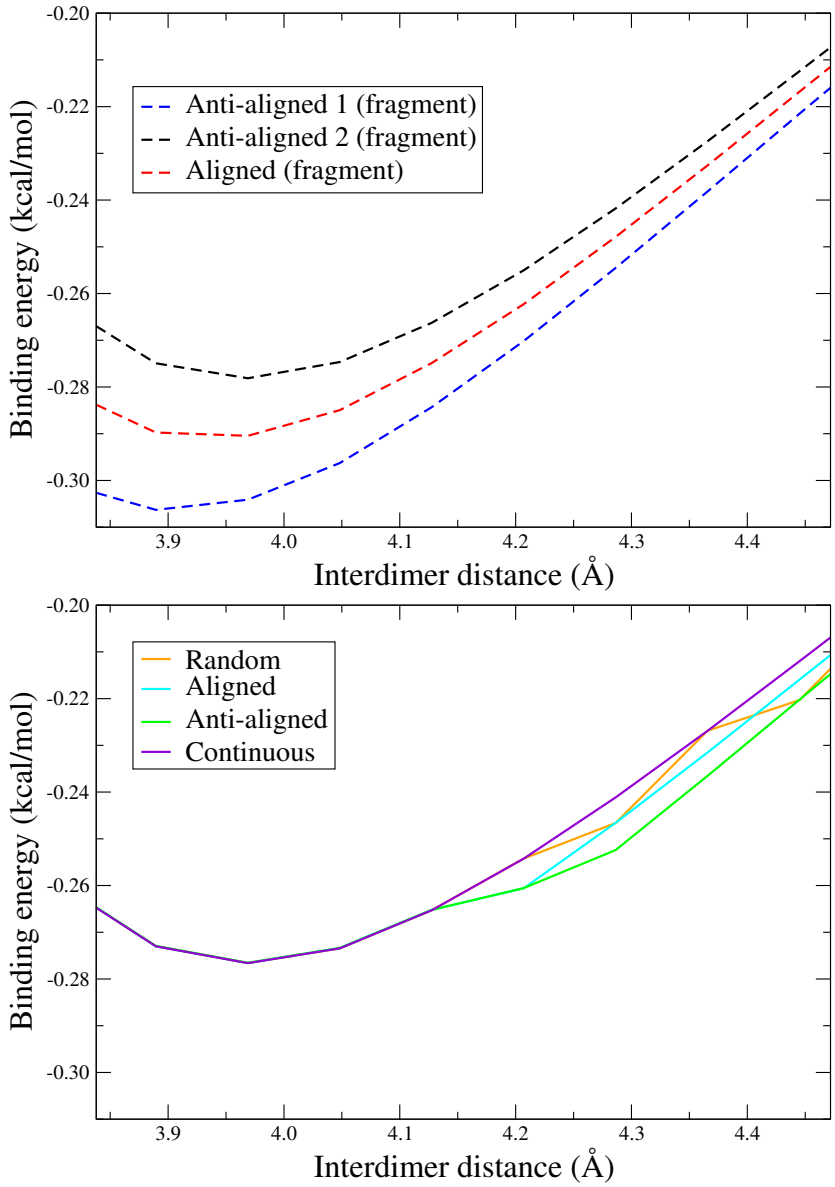


Figure 4.4: Binding energy versus interatomic separation for the argon dimer, for varying relative orientations of the MLWF centres surrounding each atom (see Fig. 4.2). Top panel: results obtained using the fragment method, in which the MLWF centres are calculated for a lone Ar atom and then translated and rotated to the second Ar atom. Bottom panel: results obtained using the true MLWF centres with various initial guesses for their positions. The curve labelled 'continuous' is obtained by using the MLWF centres from a configuration at small separation as the initial guess for the centres at larger separations. In this way, the discontinuities in the curve are avoided and a unique curve is obtained (see text for details).

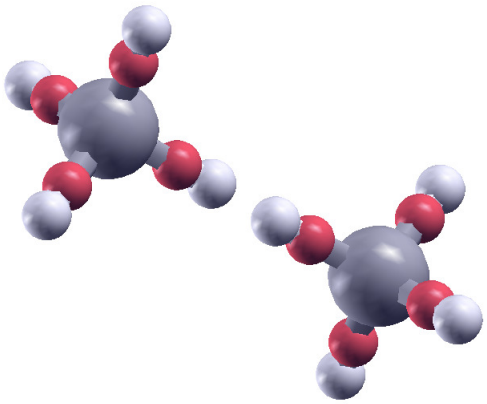


Figure 4.5: Illustration of the methane dimer. Carbon atoms are shown by large grey spheres, hydrogen by small white spheres, and the valence MLWF centres are shown by small pink spheres.

4.4.3 Methane

The methane dimer is a straightforward application of the Silvestrelli method: the positions of the 8 MLWF centres (four per molecule), which lie on the four tetrahedral C-H bonds of each CH_4 molecule (see Fig. 4.5), obey the same symmetries as the atomic positions, so there exists no arbitrariness of orientation.

In Fig. 4.6, we compare to the results of both DFT+D and CCSD(T) calculations. Our geometries and CCSD(T) results were drawn from the Benchmark Energy and Geometry Database (BEGDB) [66].

The accuracy of Silvestrelli's method in the case of the methane dimer is good compared to CCSD(T): the former gives an equilibrium separation of 3.66 Å and binding energy of -0.69 kcal/mol, and the latter 3.72 Å and -0.53 kcal/mol, respectively. DFT+D is in somewhat worse agreement with CCSD(T), yielding 3.54 Å and -0.76 kcal/mol, respectively.

4.4.4 Ethene

We now turn our attention to the ethene dimer, which includes a C-C double bond. We compare results for the original and modified methods against

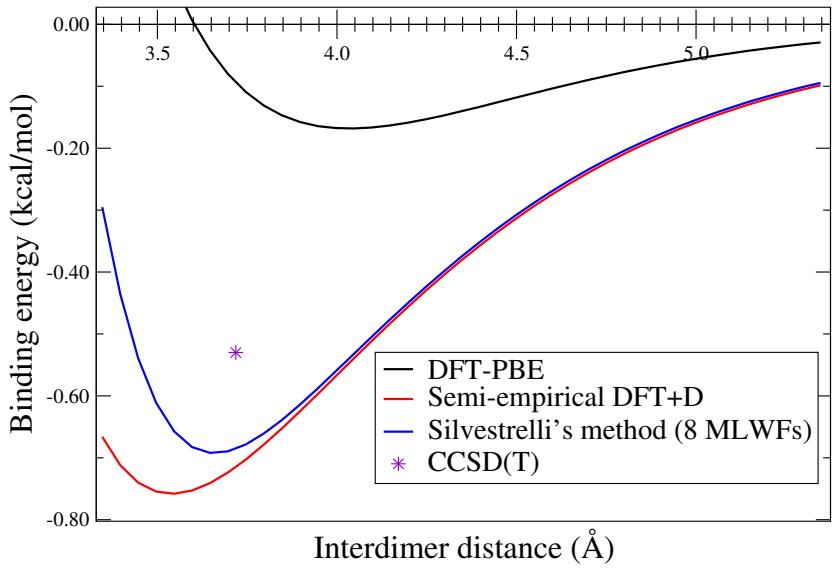


Figure 4.6: Binding energy curves for the methane dimer with various methods. In this system we do not apply our modifications as the centres of the valence MLWFs do not break any symmetry of the molecule.

CCSD(T) and DFT+D results. We have again used the geometries for each molecule taken from the BEGDB.

To use Silvestrelli's original method in this case, we include only the valence manifold in the creation of the MLWFs, giving six MLWFs per molecule arranged as shown in Fig. 4.7 (left). In our modified method we use seven MLWFs per molecule, with p-like, partly occupied orbitals on each carbon atom (Fig. 4.7 (right)).

As seen in Fig. 4.8, neither the original Silvestrelli method (blue) nor DFT+D (red) reproduce the CCSD(T) values very accurately. By expanding the manifold of eigenstates used in the construction of the MLWFs and applying our modified method to include partial MLWF occupancies and splitting of the p-like functions (see Sec. 4.3), we find an excellent agreement (green line) with the CCSD(T) equilibrium values of 3.72 Å for the separation and -1.51 kcal/mol for the binding energy; our method gives 3.73 Å and -1.60 kcal/mol, respectively; Silvestrelli's method gives 3.83 Å and -1.69 kcal/mol; DFT+D yields 3.55 Å and -2.04 kcal/mol.

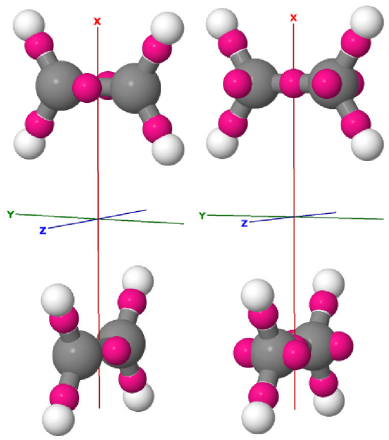


Figure 4.7: Colours as in Fig. 4.5. Left: Ethene dimer with six MLWFs per molecule. Right: Ethene dimer with seven MLWFs per molecule. The centres of the original p-like MLWFs are placed on the carbon atoms, but here we show the centres of the individual lobes after splitting each p-like orbital into two s-like functions calculated by our approach (pink spheres).

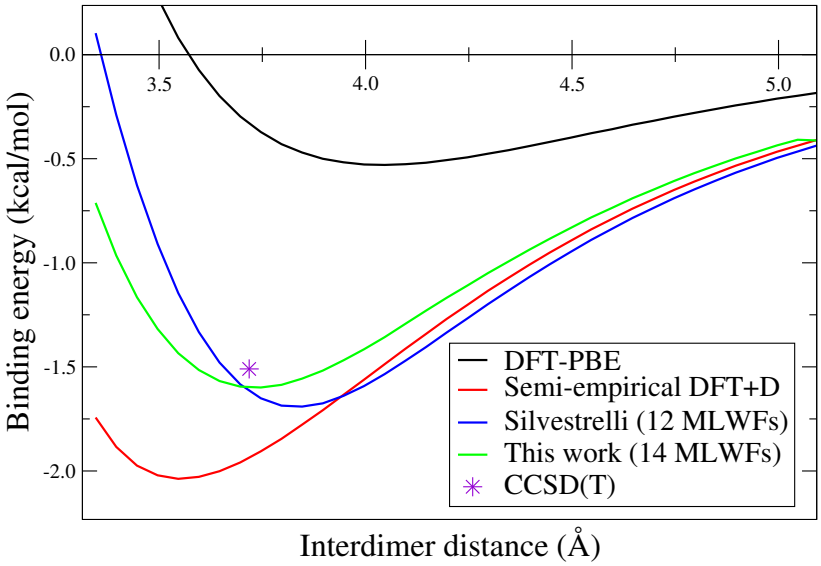


Figure 4.8: Binding energy for an ethene dimer with various methods. The agreement with the CCSD(T) value [68] is greatly improved using our modifications to the original method by Silvestrelli.

4.4.5 Benzene

For benzene, the valence states can be represented by 15 doubly-occupied Wannier functions. The MLWF optimization procedure in this case therefore breaks the D_{6h} symmetry of the benzene ring: the end result is that there are three C-C 'double' bonds and three C-C 'single' bonds in the MLWF representation. Those alternating double and single C-C bonds represent a delocalized π-bond around the ring. Each double bond is represented by MLWFs located above and below the plane of the molecule, while each single bond is represented by one MLWF on the bond. When two molecules are put in proximity (see Fig. 4.9) and the vdW energy is calculated by Silvestrelli's method, the breaking of the symmetry affects the vdW energy in an arbitrary manner, dependent on how the two rings are aligned (i.e. whether the pairs of double bonds in adjacent molecules are aligned or anti-aligned). This alignment is templated by the initial guesses used for the centres of the Wannier functions. It should be noted, however, that despite the MLWF *centres* breaking the molecule symmetry, the charge density from the MLWFs still does satisfy the symmetry, as it must.

The case of the benzene dimer therefore illustrates again the need to include the unoccupied antibonding states in the construction of the MLWFs: doing so increases the number of MLWFs to 18 and introduces partial occupancies, but restores the D_{6h} symmetry of the MLWF centres and also localizes the MLWFs more. This then makes the vdW contribution independent of the initial guess for the Wannier function centres with regards to the benzene ring alignment.

We applied our implementation of the original Silvestrelli's method (with 15 MLWFs), and then our modified method (with 18 MLWFs, partial occupancies and splitting of p-like states) to determine the binding energy as a function of displacement for three types of displacement (labelled S, PD, and T), illustrated in Fig. 4.10. We compare this to DFT+D and to the CCSD(T) calculations of Ref. [68]. We note that we used the same bond lengths for C-C and C-H as Ref. [68] to construct perfectly symmetric benzene rings for our calculations.

The binding energy curves for the various methods for the three configurations are shown in Fig. 4.10. Silvestrelli's method (blue line) does not agree very well with CCSD(T) calculations, overestimating equilibrium separations by 0.07-0.25 Å (Table 4.1) and overestimating binding energies by 0.28-1.25 kcal/mol (Table 4.2). In particular, the dispersion curve obtained from Silvestrelli's method does not agree asymptotically with the DFT+D curve (red line). In the T configuration Silvestrelli's method performs better in terms of equilib-

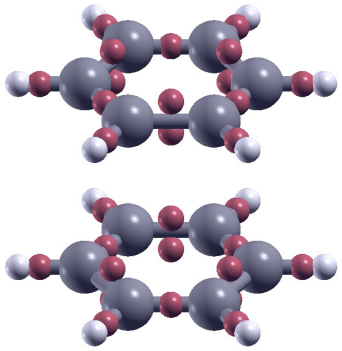


Figure 4.9: The S (vertical displacement), configuration for a benzene dimer, with MLWF centres shown by pink spheres. Notice how the centres of the MLWFs arbitrarily break the symmetry of the molecule. This symmetry breaking can have an effect on the vdW correction, since it depends on the MLWF centres.

rium separation, binding energy and asymptotics, as can be seen in Fig. 4.10 (bottom).

For the S configuration we also show the binding curve obtained when the anti-bonding states are included in the construction of the MLWFs, but p-like MLWFs are not split (orange line); it is clear that in this case the method does not perform well, because, as discussed in Sec. 4.3.2, replacing a p-like orbital by a single s-orbital is a very poor approximation.

Our full modified method, including both the larger manifold and the splitting of p-like partly occupied MLWFs, on the other hand, has excellent agreement in terms of equilibrium distances and binding energies (black line in Fig. 4.10) with the DFT+D curves and the CCSD(T) values, for all three configurations, to within 0.05 Å and 0.33 kcal/mol (Table 4.1 and 4.2); the asymptotic behaviour of the energy is also better captured.

4.4.6 H_2Pc and CuPc

To examine the difficulties encountered applying the MLWF approach for the calculation of vdW interactions to larger systems, we have investigated the phthalocyanine (H_2Pc) dimer in the simplest configuration (S, vertically displaced) first by applying Silvestrelli's method and then by applying our modifications it, and comparing the binding energy curve to one obtained using DFT+D. The

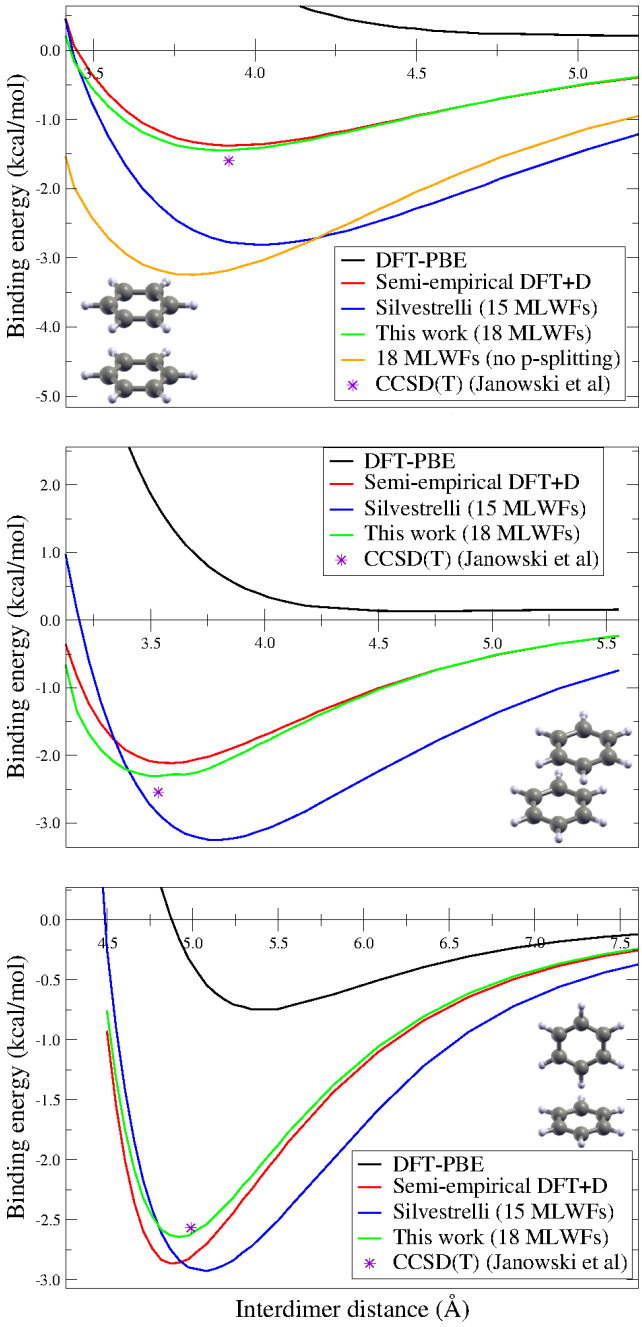


Figure 4.10: Binding energy (kcal/mol) curves for the various methods for the benzene dimer in the S, PD and T configurations (top, middle and bottom respectively). For the S configuration we also show the curve using 18 MLWFs per molecule if no p-splitting is used; in this case the method overbinds. CCSD(T) benchmark values are from Janowski *et al.* [68]. The configurations of benzene rings are shown on each graph.

Method	S	PD	T
Silvestrelli (15 MLWFs)	4.01	3.78	5.06
This work (18 MLWFs)	3.89	3.55	4.88
Semi-empirical DFT+D	3.93	3.58	4.89
CCSD(T) (Janowski *et al.* [68])	3.92	3.53	4.99

Table 4.1: Equilibrium separation in Å for the benzene dimers in the three configurations (Fig. 4.10) using the various methods. For all DFT calculations the PBE functional was used.

Method	S	PD	T
Silvestrelli (15 MLWFs)	−2.85	−3.23	−2.85
This work (18 MLWFs)	−1.47	−2.31	−2.64
Semi-empirical DFT+D	−1.38	−2.11	−2.87
CCSD(T) (Janowski *et al.* [68])	−1.60	−2.55	−2.57

Table 4.2: Binding energies (kcal/mol) at the equilibrium geometry for the benzene dimers in the three configurations (Fig. 4.10) using the various methods. For all DFT calculations the PBE functional was used.

optimized MLWF centres constructed from the valence manifold for a single H_2Pc are shown in Fig. 4.11 (top). We see that as with the benzene molecule, there are alternating single and double MLWF centres on the C-C bonds of the six-membered rings, representing delocalized π-bonds. We also find, however, that using only the 93 valence MLWFs (186 valence electrons) is problematic, since the MLWF centres break the symmetry of the system. Most importantly, this choice of using the valence manifold only in this case yields one lone MLWF of unrealistically large spread (∼2.5 Å) located some distance from any atoms (Fig. 4.11 (top)). We note again that the real density is the same under any representation, as it should, and it is the MLWF centres that break the symmetry of the system. Using a larger and even number of MLWFs (112 per molecule) we can restore this D_{2h} symmetry of the molecule (Fig. 4.11 (bottom)) and by obtaining MLWF centres that respect the symmetry of the molecule. This number of MLWFs (112) was chosen on the basis of counting the various types of bonds on the molecule.When anti-bonding states are included, it is important to make a chemically intuitive initial guess for the centres and forms of the MLWFs. We make initial guesses as follows: we place p-like orbitals on the carbon atoms and s-like orbitals on every bond and p-like orbitals on the hydrogenated nitrogens as well as two s-like orbitals on every non-hydrogenated nitrogen atom. In this

way, we have partly occupied MLWFs that represent the 372 valence electrons of the dimer. The binding energy curves obtained by using this representation and our modifications to Silvestrelli's method are shown in Fig. 4.12 and compared to DFT+D.

The binding energy obtained from our method is -23.63 kcal/mol and the equilibrium separation 3.58 Å; with DFT+D we obtain -18.91 kcal/mol and 3.68 Å. As for benzene, we see very good agreement with DFT+D; these values roughly agree with the stacking distance of crystalline H_2Pc (around 3.2–3.4 Å) [137]. Silvestrelli's original method severely overbinds the dimer (giving a binding energy of -41 kcal/mol) because of the unphysically large spread of the lone MLWF that appears in the valence representation. This is due to the strong dependence of the vdW energy on the spreads (Eq. 4.18).

In the case of CuPc dimer (vertically displaced S configuration) we again do not use the valence manifold of 390 MLWFs per dimer (195 MLWFs per molecule: 98 spin up and 97 spin down), but instead use a larger manifold of MLWFs. We note that the dimer configuration used here does not correspond to any experimentally observed phases of CuPc [138], but was used to illustrate the methods we have developed. This is a spin-polarized system, so a different set of MLWFs is required for spin up/down electrons, yielding a total of 234 singly occupied MLWFs per molecule (117 for every spin channel) in the disentangled manifold. There are 10 *d*-like MLWFs (five for every spin channel) centred on each copper atom, and *s*-like MLWFs on bonds and nitrogens. The MLWFs corresponding to spin up and spin down electrons have essentially the same centres for the same bonds or atoms (Fig. 4.13).

In cases where some Wannier functions centres are very close together, it would be incorrect to consider them as separate fragments since this would violate the fundamental assumption of the ALL method, that it is valid for non-overlapping fragments only. This can be understood from the fact that Eq. 4.13 is strongly non-linear, so adding the contributions of overlapping density fragments does not give the same result as summing the densities beforehand. As a result, Silvestrelli's method severely overbinds the dimer yielding a binding energy of ~ -108 kcal/mol, which compared to other *ab initio* results for different phthalocyanine metals (~ 50 kcal/mol for NiPc and MgPc from Ref. [139]), demonstrates that the method breaks down for overlapping fragments.

We alleviate this problem by amalgamating all the centres and spreads of the cocentric MLWFs (in this case the *d*-like MLWFs on Cu) into one MLWF with a centre and spread given by the arithmetic mean of the cocentric MLWFs,

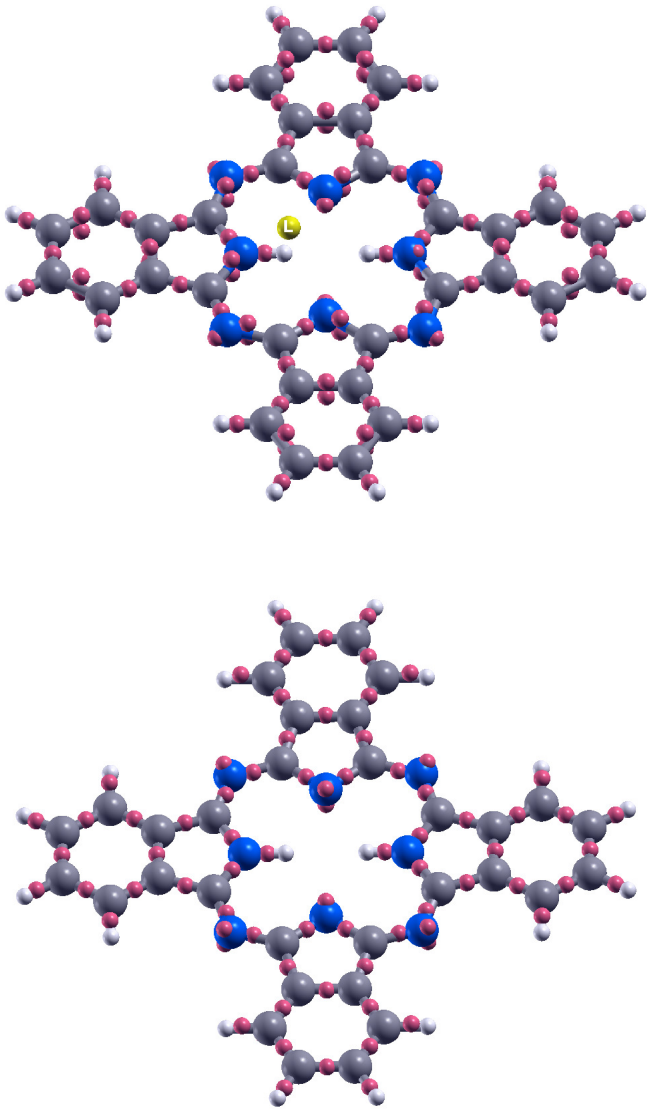


Figure 4.11: Top: Phthalocyanine (H_2Pc) molecule and its valence MLWF centres (small pink spheres). Hydrogen atoms are by small white spheres, carbon atoms by large grey spheres and nitrogen atoms by large blue spheres. Using only the valence MLWFs does not give a satisfactory description of the system since it yields a lone MLWF of unphysically large spread (shown by large yellow sphere and labelled by the letter L). Bottom: H_2Pc molecule and its 112 MLWF centres, now including anti-bonding states. With this representation the MLWF centres satisfy the D_{2h} symmetry of the molecule and a better chemical picture is given. There are s-like orbitals on every bond and the non-hydrogenated nitrogens, and p-like partly occupied orbitals on every carbon the two hydrogenated nitrogens (not shown here as these are located inside the corresponding atoms).

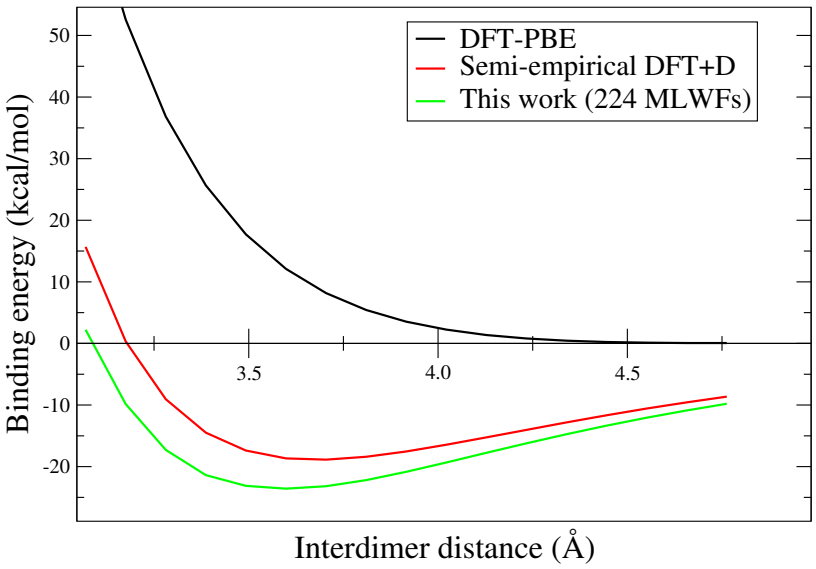


Figure 4.12: Binding energy curves for H_2Pc dimer in the S configuration (vertically displaced) versus intermolecular distance obtained with the various methods.

and occupancies given by the sum of the separate MLWFs. Physically, this corresponds to treating one larger blob of density rather than five separate ones. The criterion for amalgamating MLWFs can be automated such that MLWFs less than a particular threshold distance apart are combined. In our case, we used a value of 0.1 Å for this threshold, which had the desired effect of including the *d*-like orbitals on Cu and cocentric MLWFs in the amalgamation procedure, while leaving all other non-cocentric MLWFs in the system unaffected.

In Fig. 4.14 we compare the binding energy curves obtained using DFT+D to our modified method (now including the amalgamation of cocentric MLWFs) using a disentangled manifold of 468 MLWFs per dimer. This gives a binding energy of -27.22 kcal/mol and an equilibrium separation of 3.57 Å, in fair agreement with DFT+D, which gives -22.21 kcal/mol and 3.63 Å, respectively. These values are in reasonable agreement with those for H_2Pc (as obtained using our method above). They are also sensibly close to binding energies for other metal phthalocyanines (NiPc and MgPc) calculated with the TS-vdW scheme [139] adding vdW corrections to the PBE and B3LYP functionals, which yields values in the range $\sim 40 - 50$ kcal/mol for their binding energies.

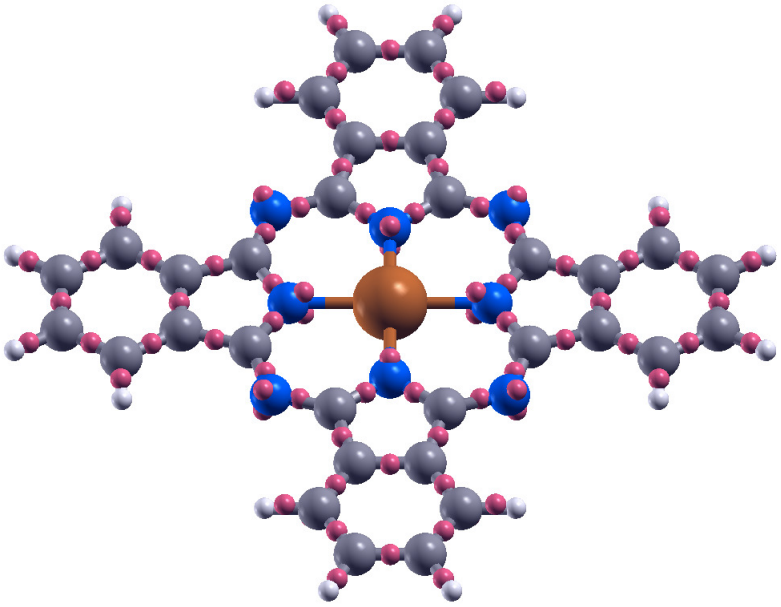


Figure 4.13: Copper phthalocyanine (CuPc) molecule and its 234 MLWF centres, again including anti-bonding states. Colours as in Fig. 4.11, with copper shown by the large brown sphere in the centre. There are *s*-symmetry MLWFs on every bond and atom except for copper, *p*-like MLWFs on the carbons and 10 *d*-symmetry MLWFs on the copper atom. Now there are no *p*-like orbitals on any nitrogen atom as for H_2Pc.

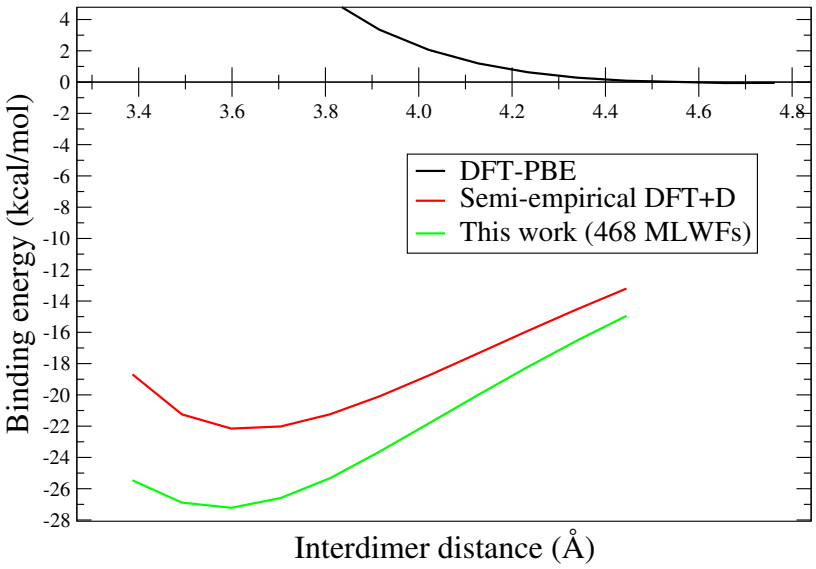


Figure 4.14: Binding energy curves for the CuPc dimer in the S configuration (vertically displaced) obtained using the various methods.

4.4.7 Intermolecular C_6 coefficients

It is expedient to define effective intermolecular C_6 coefficients,

$$C_{6\text{eff}} = \frac{1}{2}\sum_{n,l} C_{6nl}, \tag{4.26}$$

where only intermolecular terms are summed over, i.e., n and l correspond to MLWFs on different molecules, and the factor of $1/2$ accounts for double-counting. In Table 4.3, we compare our values to those of the original method of Silvestrelli, benchmark dispersion-corrected MP2 calculations (MP2+ΔvdW) and reference results obtained using the Dipole Oscillator Strength Distribution (DOSD) approach, given in the database of Ref. [70].

As previously discussed in Ref. [93], comparison with reference values is made somewhat difficult by the fact that they are obtained by fitting to experimental data and hence also include higher-order terms (C_8, C_{10}) in an effective manner.

Taking the reference values as a benchmark, it can be seen from Table 4.3 that, for the systems under consideration, there is no clear or systematic improvement in calculated effective C_6 coefficients with our modifications to Sil-

System	C_6 ($E_h a_0^6$)			
	Silvestrelli	This work	MP2+ΔvdW	pseudo-DOSD
Argon	92.4	92.4	76.1	64.3
Methane	99.1	99.1	119	130
Ethene	275	261	328	300
Benzene S	2727	1288	2364	1723
Benzene PD	2727	1284	2364	1723
Benzene T	2769	1262	2364	1723

Table 4.3: Effective intermolecular C_6 coefficients. Dispersion-corrected MP2 (MP2+ΔvdW) and reference values are drawn from Ref. [70]. For the argon and methane dimers, our approach is identical to the original method of Silvestrelli. The differences between the values reported in the first column (Silvestrelli) and those in the original paper by Silvestrelli (Ref. [93]) are attributable to the different calculational details such as choice of exchange and correlation functional, simulation cell size and plane-wave energy cutoff.

vestrelli's approach as compared to Silvestrelli's original approach: in the case of ethene the original method compares more favourably, while in the case of the benzene dimers our approach performs much better. In spite of this, however, it is worth noting that our approach (as shown earlier) significantly improves the values obtained for equilibrium separations and binding energies, as compared to CCSD(T), for all systems considered for which we have access to CCSD(T) results.

4.4.8 Sensitivity to cutoff radius r_c

The sensitivity of the binding energy on the cutoff radius r_c, given by Eq. 4.16, is investigated here. The cutoff radius is used in the integral of Eq. 4.18 as the upper boundary; its physical motivation is that it is the distance at which the the length scale for density change is equal to the electron gas screening length. Sensitivity was tested on the S configuration of the benzene dimer with 18 MLWFs per molecule (Fig. 4.15). As can be seen from Fig. 4.4.8, even small changes of 1% in the cutoff radius result in significant changes in the binding energy curves, with the binding energy and equilibrium distance varying by 6-8% and 0.2-0.8% respectively. For larger changes in r_c, the method breaks down, as the energy changes are unphysically large. Although the cutoff radius is physically justified [90], this strong dependence of the vdW correction on it is a weakness of the method.

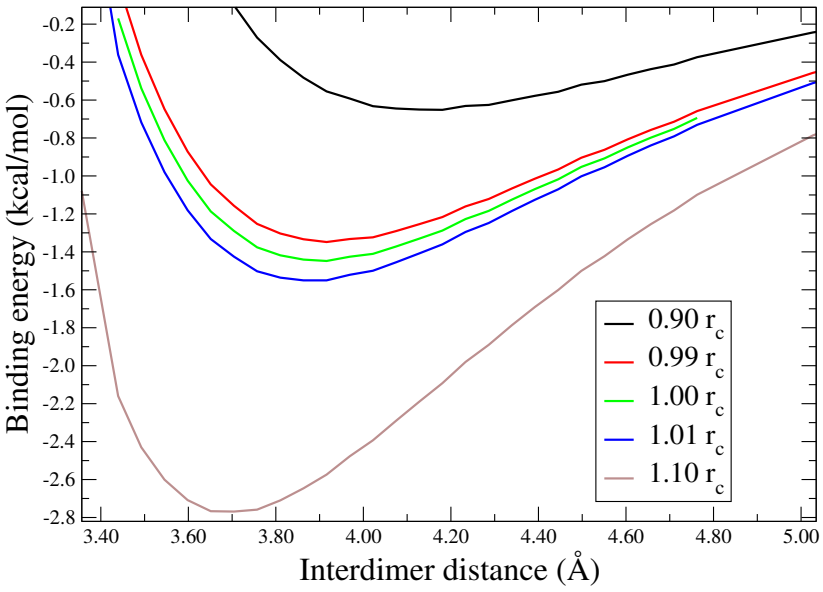


Figure 4.15: Binding energy curve for the benzene dimer in the S configuration for various values of r_c using our modified method with 18 MLWFs per molecule.

4.4.9 Approximations to the density

It is clear that the approximations to the real density will play an important role in how accurate the method is in terms of describing vdW interactions, Consequently, it is important to be aware of the various approximations that are used for the density. In the original method of Silvestrelli, the KS density is approximated by replacing all real MLWFs with hydrogenic s wavefunctions $w_n^{\mathrm{H}}(\mathbf{r})$ given by Eq. 4.17; for the purpose of calculating the C_6 coefficients, the electronic charge density of the system is, therefore, effectively approximated as

$$\rho_{\mathrm{s}}(\mathbf{r}) = \sum_{n=1}^{N_{\mathrm{occ}}} |w_n^{\mathrm{H}}(\mathbf{r})|^2. \tag{4.27}$$

In the modified method presented here, in which the MLWFs are constructed using a manifold of the KS states beyond just the occupied orbitals, there are two levels of approximation to the charge density. First, the off-diagonal component $\rho_{\mathrm{OD}}(\mathbf{r})$ is neglected from Eq. 4.10 as it is much smaller in magnitude compared to the diagonal part. Second, the "hydrogenic" approximation of the original approach is applied, whereby the disentangled Wannier functions, $w_n^{\mathrm{dis}}(\mathbf{r})$, are

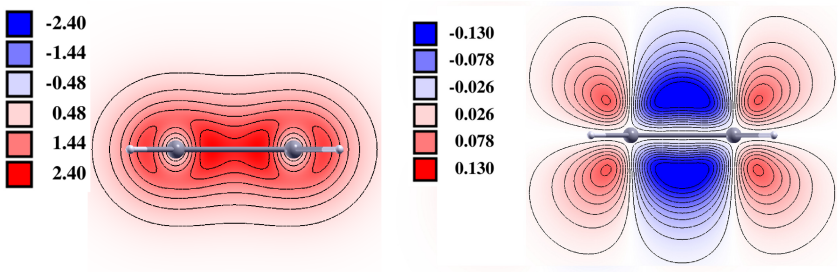


Figure 4.16: Density profile on a plane parallel to a C-C bond (xz-plane) in a benzene molecule. Left: the original Kohn-Sham density $\rho(\mathbf{r})$ from the plane-wave DFT calculation. Right: The off-diagonal component $\rho_{\rm OD}(\mathbf{r})$ of the density (see Eq. 4.10) when a disentangled manifold is used to construct $N_{\rm dis} = 18$ MLWFs. Note the much-reduced scale compared to that of the total density. The units are Å^{-3}.

replaced by hydrogenic orbitals, $w_n^{\rm H}(\mathbf{r})$, of the same centre and spread. In our method, therefore, the density is approximated as

$$\rho_{\rm dis}(\mathbf{r}) = \sum_{n=1}^{N} f_{nn}^{w} |w_n^{\rm H}(\mathbf{r})|^2, \tag{4.28}$$

where N is now the of total number of fragments, after the splitting of p-like orbitals or amalgamation of co-centric MLWFs has been performed. We consider each of these approximations in turn for a system that exhibits some typical features, the benzene molecule. The XCrySDen [140] package was used to generate the isosurface plots referred to in this Section.

In Fig. 4.16 we show density isosurface plots for the KS density $\rho(\mathbf{r})$ (left) and the off-diagonal density $\rho_{\rm OD}(\mathbf{r})$ (right), which emphasises that the latter is uniformly small in magnitude, comprising only a small fraction of the total density ($\sim 5-7\%$), as a result of the exponential localisation of the MLWFs, which results in small overlap between the MLWFs, and thus any off-diagonal elements do not contribute significantly to the total density.

In Fig. 4.17 we show the difference between the KS density $\rho(\mathbf{r})$ and the "hydrogenic" approximation $\rho_{\rm s}(\mathbf{r})$ of the original Silvestrelli method (Eq. 4.27) for two of the C-C bonds in benzene: on the left a "single" bond; on the right a "double" bond. These two bonds only differ because of the symmetry-breaking inherent in the MLWF construction when just the valence states are used. We see that the density associated with the π-bond is not well represented in either

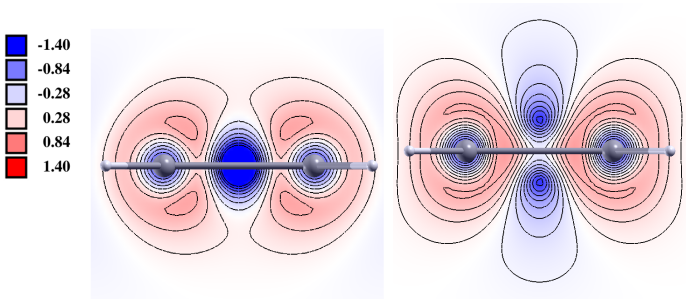


Figure 4.17: Density difference isosurface plots showing the difference $\rho(\mathbf{r})-\rho_{\mathrm{s}}(\mathbf{r})$ between the KS density and the approximate "hydrogenic" density of the original Silvestrelli approach (Eq. 4.27). Left: cross-section through a "single" bond. Right: cross-section through a "double" bond.

case. Note that the decomposed charge density is the same as the KS density, and it is only when we look at the density associated with individual MLWFs which have been approximated, that the symmetry is broken.

Finally, in Fig. 4.18, we show the difference between the KS density $\rho(\mathbf{r})$ and that of our modified method, $\rho_{\mathrm{dis}}(\mathbf{r})$ (Eq. 4.28), with 18 MLWFs obtained by disentanglement from a larger manifold. The left-hand plot is without splitting the p-like states, and the right-hand plot is with splitting (as described in Sec. 4.3). We see that while this introduces small regions where the density differs significantly (right at the MLWF centres), everywhere else it is overall an improvement, producing a better representation of the density compared to the original method of Silvestrelli, especially in the case of systems with p-orbitals.

In summary, discarding the off-diagonal component of the density (in the case of disentangled MLWFs) is a relatively minor approximation, and has a considerably smaller effect than approximating the density in various ways using hydrogenic orbitals, the latter being inherent to both our approach and the original approach of Silvestrelli. The maximum difference between the KS density $\rho(\mathbf{r})$ and the density in our method is reduced by $\sim 23\%$ and the minimum difference by $\sim 5\%$, compared to the difference between the KS density and the density in Silvestrelli's method.

4.4.10 Sensitivity to energy window E_{win}

To use our modifications to Silvestrelli's method, the disentanglement procedure has to be used in the construction of Wannier functions, as outlined in the

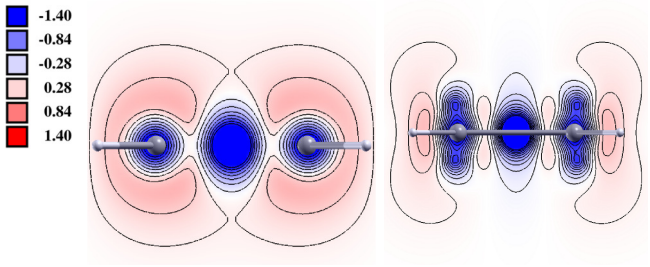


Figure 4.18: Density difference isosurface plots, on the same plane as in Fig. 4.16, showing the difference $\rho(\mathbf{r})-\rho_{\rm dis}(\mathbf{r})$ between the KS density and the "hydrogenic" density of our method when a disentangled set of MLWFs is used (Eq. 4.28). Left: without splitting of p-like states; right: with splitting of p-like states into two s-like states. The mean difference with the KS density compared to the original Silvestrelli's method is reduced overall for both cases, but even more in the case of p-splitting.

Methods section 4.1. Because including ever more high-energy plane-wave states inevitably allows extra variational freedom in the construction of the MLWFs, we find that the precise values of the MLWF spreads are sensitive to the outer energy window used for the disentanglement. Specifically, as $E_{\rm win}$ is increased, the MLWFs become more localized (their spreads decrease). As a result, the vdW energy is also affected by the choice of $E_{\rm win}$.

In this work we have chosen throughout to estimate an appropriate energy window using

$$E_{\rm win} = \varepsilon_{\rm LUMO} + \alpha(\varepsilon_{\rm HOMO} - \varepsilon_0) \tag{4.29}$$

where α is a factor used to scale the valence energy bandwidth. This is motivated by the idea that to enable us to restore the symmetry, we need to include the antibonding counterparts to the valence states, without including too large a number of irrelevant higher-lying unbound states. Eq. 4.29 is an attempt to estimate the range of energies spanned by these antibonding states. In Fig. 4.19 we show the dependence of the vdW binding energy curves for the benzene dimer in the S configuration on α. While there is considerable variation for small α, we find that for values beyond 0.4, the curves vary by only a rather small amount with α; As long as a value of α around this value is chosen, it should yield reasonable results, suggesting the extra degree of empiricism introduced by this procedure is relatively limited in scale. The value of α was set to 0.4 in all the other calculations in this work.

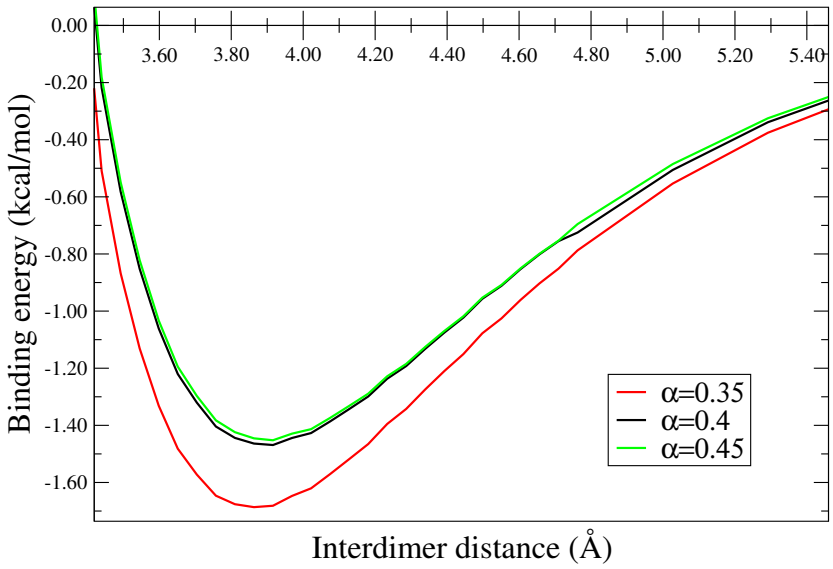


Figure 4.19: Binding energy curve for the benzene dimer in the S configuration for various values of α using our modified method with 18 MLWFs per molecule.

4.5 vdW interactions with NGWFs

As we saw earlier, MLWFs are constructed in a post-processing fashion after a full electronic structure calculation, for example with the plane-wave DFT code Quantum Espresso in this case. The system size accessible to any vdW approach involving MLWFs will be limited by the DFT calculation. The scaling of traditional plane-wave DFT is $O(N^3)$, which allows for a maximum of a few hundreds of atoms. In applications of Silvestrelli's method or its modified version, the size of the system one can study is further limited by the fact that MLWFs become challenging to disentangle for large, structurally complex systems. Motivated by these facts, we attempted to use the non-orthogonal generalized Wannier functions (NGWFs) that arise naturally from the linear-scaling DFT approach implemented in ONETEP as fragments of density, which would then be replaced by hydrogenic orbitals treated as in the original method by Silvestrelli. The main benefit of this would be that within the framework of linear-scaling DFT, this would allow calculations on large systems without the manual effort of determining an appropriate choice of localized orbitals, since, as mentioned before, these naturally arise within ONETEP. Here we show details

of this attempt and explain why it was not pursued.

First we briefly introduce NGWFs, but these will be revisited in more detail in Ch. 5. The NGWFs are related to the Kohn-Sham eigenstates by a linear transformation:

$$|\psi_n\rangle = M^{\alpha}_{\ n}|\phi_\alpha\rangle \tag{4.30}$$

where the Einstein summation convention is used for the Greek indices.

Using the orthonormality of KS states we can write

$$\begin{aligned}\langle\psi_n|\psi_m\rangle &= M^{*\alpha}_{\ n}M^{\beta}_{\ m}\langle\phi_\alpha|\phi_\beta\rangle \\ &= M^{*\alpha}_{\ n}M^{\beta}_{\ m}S_{\alpha\beta} = \delta_{nm}\end{aligned} \tag{4.31}$$

where the overlap matrix $S_{\alpha\beta} = \langle\phi_\alpha|\phi_\beta\rangle$ has been defined. The overlap matrix is the metric and it is used to lower indices as $S_{\beta\alpha}|\phi^\alpha\rangle = |\phi_\beta\rangle$, where $|\phi^\alpha\rangle$ are the contravariant NGWFs, orthogonal to the covariant ones. The inverse of $S_{\alpha\beta}$, defined as $S^{\alpha\beta}$ satisfies $S_{\beta\alpha}S^{\alpha\gamma} = \delta^{\alpha}_{\ \gamma}$. It can be shown (App. A) that the inverse overlap can be written as

$$S^{\alpha\beta} = \sum_m M^{*\alpha}_{\ k}M^{\beta}_{\ m}. \tag{4.32}$$

This expression will be used extensively in the calculations to follow.

The MLWFs are related to the KS orbitals in the following way:

$$|w_n\rangle = \sum_m U_{mn}|\psi_m\rangle$$

where $\mathbf{U}$ is a unitary transformation as we saw in Sec. 4.1. Using Eq. 5.7, the MLWFs can be expressed in terms of the NGWFs as:

$$|w_n\rangle = \sum_m U_{mn}M^{\beta}_{m}\,|\phi_\beta\rangle \tag{4.33}$$

We recall that the expression for the spread in terms of MLWFs is:

$$\Omega = \sum_n \Omega_n = \sum_n \langle w_n|(\mathbf{r} - \langle\mathbf{r}\rangle_n)^2|w_n\rangle = \sum_n [\langle\mathbf{r}^2\rangle_n - \langle\mathbf{r}\rangle_n \cdot \langle\mathbf{r}\rangle_n]. \tag{4.34}$$

This expression can be decomposed as $\Omega = \Omega_I + \Omega_{OD}$ where

$$\Omega_I = \sum_n [\langle \mathbf{r}^2 \rangle_n - \sum_m |\langle w_m|\mathbf{r}|w_n\rangle|^2] \tag{4.35}$$

$$\begin{aligned}\Omega_{OD} &= \sum_n \sum_{m\neq n} |\langle w_m|\mathbf{r}|w_n\rangle|^2 \\ &= \sum_n \sum_{m\neq n} \langle w_m|\mathbf{r}|w_n\rangle \cdot \langle w_n|\mathbf{r}|w_m\rangle\end{aligned} \tag{4.36}$$

Now trying to find expressions for Ω_I and Ω_{OD} in terms of NGWFs, we use Eq. 4.33 and the fact that $\sum_n U_{mn}U^*_{kn} = \delta_{mk}$ to find, for the first term of Ω_I:

$$\sum_n \langle w_n|r^2|w_n\rangle = \sum_{n,k,m} U_{mn}U^*_{kn} M^{\alpha}_{*\ k} M^{\beta}_{\ m} \langle \phi_\alpha|r^2|\phi_\beta\rangle = S^{\beta\alpha} r^2_{\alpha\beta}$$

The second term from the Ω_I expression becomes:

$$\begin{aligned}&\sum_n \sum_m \sum_{pqrs} \langle \phi_\alpha|\mathbf{r}|\phi_\beta\rangle \cdot \langle \phi_\gamma|\mathbf{r}|\phi_\delta\rangle U_{qn}U^*_{pm}U_{sm}U^*_{rn} M^{*\alpha}_p M_q{}^{\beta} M_s{}^{\delta} M^{*\gamma}_r \\ &\sum_{pqrs} \langle \phi_\alpha|\mathbf{r}|\phi_\beta\rangle \cdot \langle \phi_\gamma|\mathbf{r}|\phi_\delta\rangle \delta_{ps}\delta_{qr} M^{*\alpha}_p M_q{}^{\beta} M_s{}^{\delta} M^{*\gamma}_r = \\ &\sum_{pq} \langle \phi_\alpha|\mathbf{r}|\phi_\beta\rangle \cdot \langle \phi_\gamma|\mathbf{r}|\phi_\delta\rangle M^{*\alpha}_p M_q{}^{\beta} M_p{}^{\delta} M^{*\gamma}_q = \mathbf{r}_{\alpha\beta} \cdot \mathbf{r}_{\gamma\delta} S^{\delta\alpha} S^{\beta\gamma}\end{aligned}$$

Definining the centres of the NGWFs as:

$$\mathbf{r}_\alpha{}^{\alpha} = \langle \phi_\alpha|\mathbf{r}|\phi^\alpha\rangle = \langle \phi_\alpha|\mathbf{r}|\phi_\beta\rangle S^{\beta\alpha} \tag{4.37}$$

we may then define the NGWF spread as:

$$\begin{aligned}\Omega_\alpha{}^{\alpha} &= \langle \phi_\alpha|(\mathbf{r} - \mathbf{r}_\alpha{}^{\alpha})^2|\phi^\alpha\rangle \\ &= r^{2\alpha}_\alpha - \mathbf{r}_\alpha{}^{\alpha} \cdot \mathbf{r}_\alpha{}^{\alpha} \\ &= S^{\beta\alpha} r^2_{\alpha\beta} - \mathbf{r}_{\alpha\beta} \cdot \mathbf{r}_{\alpha\delta} S^{\beta\alpha} S^{\delta\alpha}\end{aligned} \tag{4.38}$$

Now the invariant part of the spread can be written as:

$$\begin{aligned}\Omega_I &= \sum_{\alpha\beta} S^{\beta\alpha} r^2_{\alpha\beta} - \sum_{\alpha\beta\delta} \mathbf{r}_{\alpha\beta} \cdot \mathbf{r}_{\alpha\delta} S^{\beta\alpha} S^{\delta\alpha} - \sum_{\alpha\neq\gamma} \sum_{\beta\delta} \mathbf{r}_{\alpha\beta} \cdot \mathbf{r}_{\gamma\delta} S^{\delta\alpha} S^{\beta\gamma} \\ &= \sum_\alpha \Omega_\alpha{}^{\alpha} - \sum_{\alpha\neq\gamma} \sum_{\beta\delta} \mathbf{r}_{\alpha\beta} \cdot \mathbf{r}_{\gamma\delta} S^{\delta\alpha} S^{\beta\gamma}\end{aligned}$$

The off-diagonal part of the spread, when expressed in terms of the NGWFs becomes (Einstein summation convention used for greek indices):

$$\begin{aligned}\Omega_{OD} &= \sum_{n}\sum_{m\neq n}\sum_{pqrs}\langle\phi_\alpha|\mathbf{r}|\phi_\beta\rangle\cdot\langle\phi_\gamma|\mathbf{r}|\phi_\delta\rangle U_{qn}U^*_{pm}U_{sm}U^*_{rn}M_p^{*\alpha}M_q{}^{\beta}M_s{}^{\delta}M_r^{*\gamma}\\ &= \sum_{n}\sum_{m\neq n}\sum_{pqrs}\langle\phi_\alpha|\mathbf{r}|\phi_\beta\rangle\cdot\langle\phi_\gamma|\mathbf{r}|\phi_\delta\rangle U_{qn}U^*_{pm}U_{sm}U^*_{rn}M_p^{*\alpha}M_q{}^{\beta}M_s{}^{\delta}M_r^{*\gamma}\end{aligned}$$

The form of the off-diagonal spread now poses a problem: it cannot be expressed in terms of overlap matrices as the other expression shown, and there is no apparent cancellation of the unitary transformation matrices $\mathbf{U}$. Using an orthogonal basis for the expression of the spread clearly does not allow us to write it purely in terms of NGWFs. Therefore, to be able to use this type of partitioning of the density, an alternative expression for the spread is needed. There are tensorial correctness issues that arise when one attempts to find an expression for the spread purely in terms of NGWFs because the covariant and contravariant spaces complicate the definition of tensors. As a result, care has to be taken when attempting to express a physical quantity with respect to covariant and contravariant indices. Finding a way to express the spread in such a way is an interesting problem which can be further explored.

4.6 Conclusion

We conclude that Silvestrelli's method is computationally efficient and very easy to implement for small systems where initial guesses for the Wannier centres can be specified. However, there is a very strong dependence of the calculated vdW energy on the position and spread of the Wannier centres, and these are not always as unique as one might hope. Symmetry-breaking, often induced by considering only the valence manifold in the construction of the MLWFs, may introduce arbitrary dependence on initial guesses in a way that significantly affect the vdW energy. We have shown that arbitrarily-broken symmetries may often be restored by increasing the number of Wannier functions used and generating them with a suitably-chosen range of the conduction states as well as the valence states. This necessitates the inclusion of occupancies in the formalism. We note that in cases where no symmetries are restored when we use more MLWFs, as in the example of ethene, it is the better localisation of the MLWFs that may be responsible for improved vdW energies, since the method is based

on pairwise summation of well-separated fragments.

Particularly, in cases with a larger number of Wannier functions, we have shown that the approximation implicit in replacing the true Wannier functions with hydrogenic s-orbitals may not always yield an accurate representation of the electronic density, and have shown how in cases where there is p-like symmetry, it is better to substitute the p-symmetry functions with two s-like functions. By considering the problems associated with applying these adapted methods to larger systems such as H_2Pc and CuPc, we have demonstrated that the approach is not necessarily a good candidate for studying larger systems, where specifying initial guesses for a large number of non-trivial MLWFs may be difficult; chemical insight for the form of these higher-lying states has to be employed, but becomes more difficult for even larger systems. In the case of copper phthalocyanine, we showed that MLWFs that are centred effectively at the same point (such as the five d-like MLWFs on each Cu atom) cannot be treated as separate fragments of density; they should instead be amalgamated into one fragment of density of an averaged centre and spread and summed occupancies. The reason for this is that the method is valid only in the limit of well-separated fragments. Finally, we have demonstrated that there is also a strong dependence of the vdW energy on the cutoff radius used in the integral of Eq. 4.18, and although the value used is justified on physical grounds, it nevertheless represents something of an adjustable parameter with considerable influence on the results obtained. Overall, we conclude that while Silvestrelli's method suffers from several drawbacks, it can be made rather accurate once modifications are applied to it (albeit with the introduction of further empirical character); these improvements, and Silvestrelli's method in general, however, may be less suitable for more structurally complex, large-scale systems, for which alternative methods that are more fully *ab initio* may be desirable. Recent developments to Silvestrelli's method [128, 130] have addressed the issue of overlapping fragments that we point out in this work, and have also implemented many other changes in other directions, overall improving the sophistication of the method and obtaining better agreement with experimental data on a number of systems. Ideally, one would like to test the method with our improvements on the whole S22 set, but the manual effort required to correct the shortcomings of the method on a case-by-case basis made this problematic. A fully automated implementation of this method, however, could make that possible and this might be a possibility for future work. The idea of applying this method with its modifications to ONETEP might be feasible if an alternative expression for

the spread is found. However, a seamless, fully automated *ab initio* scheme to include vdW in ONETEP in particular was a much more attractive solution that allow larger-scale simulations to be performed.

Chapter 5

The vdW-DF method in ONETEP

In this chapter, linear-scaling DFT is briefly discussed. Next, an overview of ONETEP, a linear-scaling DFT package, is given. Finally, the mathematical details of Soler's efficient algorithm [2] for calculating the vdW-DF non-local correlation energy and potential are presented; we implemented the algorithm in ONETEP, allowing self-consistent *ab initio* calculations with dispersion interactions included, as opposed to semi-empirical methods where the dispersion interaction energy is merely added to the total DFT energy. While three semi-empirical schemes [88,141,142] for dispersion have been implemented [89] within ONETEP, an *ab initio* method was lacking, therefore the incorporation of vdW-DF into the code was sought.

For a system with N number of atoms, Soler's algorithm scales as order $N \log N$, which makes it an extremely useful addition to a linear-scaling code such as ONETEP because it opens the possibility of simulating large-scale systems where dispersion interactions play an important role.

Scaling tests are given, which show that the total computational time in ONETEP with vdW-DF scales linearly, with the additional time for vdW-DF being dominated by the linear part of the calculation.

5.1 Linear-scaling DFT

In this section we discuss the key concepts and principles behind linear-scaling DFT. A number of DFT codes use a plane-wave (PW) basis (CASTEP [143], ABINIT [144], Quantum Espresso [132]) to calculate total energies and forces and to geometry optimize structures to find the ground state configuration. Working with the KS formalism, where a fictitious system of non-interacting particles with associated single-particle eigenstates is treated requires the orthonormality conditions, $\langle\psi_m|\psi_n\rangle = \delta_{mn}$, to be satisfied; this imposes $O(N^2)$ constraints where the number of atoms in the system is N. Furthermore, because of the KS orbitals being delocalized over the system, the number of operations to maintain that orthonormality condition by calculating the overlap integral is $O(N^3)$. There are computational bottlenecks that arise because of this, and, as a result there has been an increasing interest in linear-scaling DFT [145–147]. For a given pair of methodologies there exists a crossover point for the number of atoms in a given system where the computational time will be less with linear-scaling method than with a cubic-scaling one. The real potential of linear-scaling DFT lies in the ability to perform calculations beyond that crossover point. The aforementioned computational bottlenecks start being an issue for systems of a few hundreds of atoms.

It was shown by Kohn [148] that electronic structure is near-sighted. This near-sightedness, which applies to the electronic density, has the implication that it is possible to have a linear-scaling approach in DFT, since, from the original HK theorems we know that density is the fundamental variable and only contains $O(N)$ information. While the single-particle Bloch eigenstates are delocalized over the system, both the single particle density matrix and the Wannier functions (Ch. 4, Sec. 4.1) are in fact exponentially localized in systems with a band gap (Kohn [149], des Cloizeaux [150]); that is $\rho(\mathbf{r}, \mathbf{r}') \propto e^{-\gamma|\mathbf{r}-\mathbf{r}'|}$. The localization of the density matrix is in fact related to the exponential localization of Wannier functions [151]. The localization properties of the density allow us to truncate a real-space representation of the density matrix, thus achieving linear-scaling.

There exist various linear-scaling DFT approaches [152–157]. One class of approaches relies on variationally minimizing an energy functional, which is expressed in terms on Wannier orbitals or the density operator. In these methods, orthogonality is satisfied by construction, and not imposed.

Another class of methods use non-orthogonal localized orbitals (as opposed

to orthogonal Wannier functions). There are advantages to using such an approach, since the non-orthogonal orbitals are generally more localized than the orthogonal ones, and also imposing orthogonality is no longer required as an operation. One such method is the approach used in ONETEP, the details of which will be discussed in the next section.

There have also been attempts to develop orbital-free approaches [158, 159], but they have been generally unsuccessful in describing tightly-bound covalent systems.

5.2 ONETEP

ONETEP [8, 160, 161] is a DFT package that combines the benefits of linear-scaling computational effort, plane-wave accuracy, and efficient parallel scaling. Linear scaling is achieved both with number of atoms and number of processors used for the computation.

In order to outline the formalism used in ONETEP, first we introduce the single-particle non-interacting density operator $\hat{\rho}$ (assuming Γ-point sampling only):

$$\hat{\rho} = \sum_n |\psi_n\rangle f_n \langle\psi_n| \tag{5.1}$$

where f_n is the occupancy of state n and $|\psi_n\rangle$ are one-electron orthogonal orbitals. The density matrix is then defined as:

$$\rho(\mathbf{r}, \mathbf{r}') = \langle \mathbf{r}|\hat{\rho}|\mathbf{r}'\rangle = \sum_n f_n \psi_n^*(\mathbf{r})\psi_n(\mathbf{r}'). \tag{5.2}$$

The density operator (and equivalently the density matrix) is required to be idempotent, that is $\hat{\rho}^2 = \hat{\rho}$. This constraint is imposed by the fact that at zero temperature the occupancies f_n of the states are either 0 or 1 and the orthonormality of the KS eigenstates. The idempotency requirement

$$\hat{\rho}^2 = \sum_{n,m} |\psi_n\rangle f_n \langle\psi_n|\psi_m\rangle f_m \langle\psi_m| = \sum_n |\psi_n\rangle f_n^2 \langle\psi_n| \tag{5.3}$$

indeed yields $f_n^2 = f_n$, which can only hold if the initial constraint of 0 or 1 occupancies is valid. Moreover, the orthonormality condition was used, so we can see that idempotency enforces these two conditions.

The electron number, N, required to impose the normalization constraint,

can be calculated from

$$N = 2 \int \rho(\mathbf{r}, \mathbf{r}) d\mathbf{r}. \tag{5.4}$$

The sum of the energy eigenvalues of the KS non-interacting eigenstates, which can be used to calculate the total ground state energy after subtracting some double counting terms as we have seen in Sec. 2.2, is given by

$$E = 2 \sum_n f_n \varepsilon_n = 2 \sum_n f_n \langle \psi_n | \hat{H} | \psi_n \rangle \tag{5.5}$$

where $\hat{H}$ is the Kohn-Sham Hamiltonian from Eq. 2.29. The factor of two is due to spin degeneracy.

As mentioned in Sec. 5.1, for insulating systems, the density matrix is exponentially localized, $\rho(\mathbf{r}, \mathbf{r}') \propto e^{-\gamma|\mathbf{r}-\mathbf{r}'|}$. By exploiting the exponential localisation of the density matrix in a system with non-vanishing band gap we can set the density matrix to zero for separations greater than some chosen cutoff radius R_c:

$$\rho(\mathbf{r}, \mathbf{r}') = 0 \text{ for } |\mathbf{r}' - \mathbf{r}| > R_c \tag{5.6}$$

ONETEP makes use of highly-localized orbitals, the Non-orthogonal Generalised Wannier Functions (NGWF) [162], the concept of which is shown in Fig. **??**. These are related to the Kohn-Sham eigenstates by a linear transformation:

$$|\psi_n\rangle = M_n^{\alpha} |\phi_\alpha\rangle \tag{5.7}$$

where the Einstein summation convention is used for repeated Greek indices.

By orthonormality of the KS eigenstates,

$$\langle \psi_n | \psi_m \rangle = M_n^{*\alpha} M_m^{\beta} \langle \phi_\alpha | \phi_\beta \rangle = \delta_{mn} \tag{5.8}$$

We define the overlap matrix as $S_{\alpha\beta} = \langle \phi_\alpha | \phi_\beta \rangle$, which is the metric, and can be used to raise and lower Greek indices. For the covariant space of functions, there exists a contravariant space. The dual functions $\{\phi^\alpha\}$ are related to the $\{\phi_\alpha\}$ through the inverse of $S_{\alpha\beta}$:

$$\phi^\alpha(\mathbf{r}) = (S^{-1})^{\beta\alpha} \phi_\beta(\mathbf{r}) \tag{5.9}$$

The dual set $\{\phi^\alpha\}$ then satisfies the orthonormality condition with respect

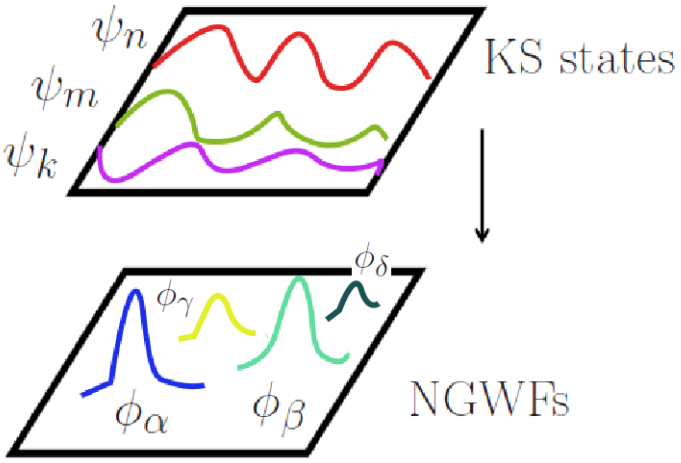


Figure 5.1: Simplified two-dimensional picture of Top: Kohn-Sham (KS) orbitals, delocalized over the system Bottom: NGWF orbitals, highly localized.

to $\{\phi_\alpha\}$:

$$\langle \phi^\alpha | \phi_\beta \rangle = \delta^\alpha{}_\beta \tag{5.10}$$

The NGWFs are expanded in a periodic cardinal sine (psinc) function set [163], which are essentially bandwidth-limited representations of delta functions on each grid point:

$$\phi_\alpha(\mathbf{r}) = \sum_i C_{i,\alpha} D_i(\mathbf{r}) \tag{5.11}$$

This allows for the truncation of any contributions of the NGWFs outside their localization spheres (Fig. 5.2).

Using Eq. 5.7, the density operator may be written in terms of NGWFs:

$$\hat{\rho} = \sum_n |\psi_n\rangle f_n \langle \psi_n| = \sum_n (M^\dagger)_n^\beta M^\alpha_n |\phi_\alpha\rangle f_n \langle \phi_\beta| = \sum_n |\phi_\alpha\rangle K^{\alpha\beta} \langle \phi_\beta| \tag{5.12}$$

where

$$K^{\alpha\beta} = \sum_n M^\alpha_n f_n (M^\dagger)^\beta{}_n \tag{5.13}$$

is the matrix representation of the density operator and is called the *density kernel*.

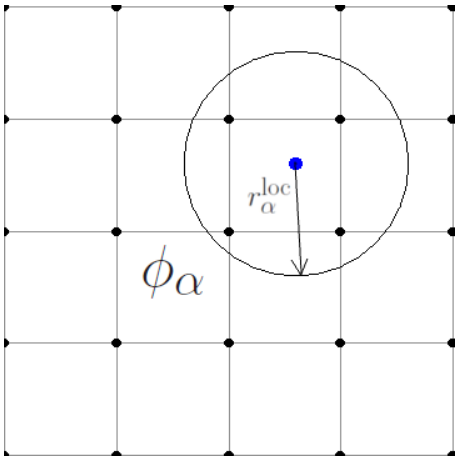


Figure 5.2: Illustration of the psinc grid (black dots) in the simulation cell, as well as a NGWF and its localization region. The blue dot shows the centre of the NGWF. A radial cutoff, r_α^{loc} is imposed on the NWGFs.

Keeping in mind the exponential localization of the density matrix (Eq. 5.6) and the fact that the density kernel is a representation of the density matrix in terms of the NGWFs, we require that the elements of the density kernel, $K^{\alpha\beta}$, vanish beyond a localisation radius:

$$K^{\alpha\beta} = 0 \text{ for } |\mathbf{r}_\alpha - \mathbf{r}_\beta| > R_c \tag{5.14}$$

where $\mathbf{r}_\alpha$ and $\mathbf{r}_\beta$ are the centres of ϕ_α and ϕ_β, respectively. Imposing a radial cutoff, R_c, on the density kernel, along with a radial cutoff imposed on the NGWFs, r_α^{loc}, makes the density kernel sparse, meaning that a significant number of its elements are zero. As a result, the information contained in the density matrix scales linearly with system size.

By enforcing the idempotency condition from Eq. 5.3, we find that, in this representation

$$\begin{aligned}\hat{\rho}^2 &= \sum_{\alpha\beta\gamma\delta} |\phi_\alpha\rangle K^{\alpha\beta} K^{\gamma\delta} \langle\phi_\beta|\phi_\gamma\rangle\langle\phi_\delta| \\ &= \sum_{\alpha\beta\gamma\delta} |\phi_\alpha\rangle K^{\alpha\beta} S_{\beta\gamma} K^{\gamma\delta} \langle\phi_\delta|\end{aligned} \tag{5.15}$$

which leads to

$$\mathbf{KSK} = \mathbf{K} \tag{5.16}$$

Imposing idempotency on the density kernel in the way expressed in Eq. 5.16 would require direct diagonalization. This is an operation that scales as $O(N^3)$ for an $N \times N$ matrix, and $O(N^2)$ if the matrix is sparse, as it is in this case. This poses a problem as linear-scaling is the purpose of this formulation. There are various methods for optimizing the density matrix [164], that make use of *penalty functionals*, which are transformations applied to the density matrix while still satisfying the imposed constraints. The Li, Nunes and Vanderbilt (LNV) [165] method uses a penalty functional by McWeeney [166] and is constructed to minimize the total energy with *implicit* idempotency for the density matrix at the minimum. The LNV method has been generalized for use with a non-orthogonal basis [167] and is commonly used in ONETEP. We note here that a minimal basis of NGWFs is used, and the NGWFs are optimized self-consistently during a calculation, as well as the density kernel [168].

In the position representation and using the NGWF representation, the density matrix is given by

$$\rho(\mathbf{r}, \mathbf{r}') = \sum_{\alpha\beta} \phi_\alpha(\mathbf{r}) K^{\alpha\beta} \phi^*_\beta(\mathbf{r}'). \tag{5.17}$$

Combining Eq. 5.17 with Eq. 5.4 we see that

$$\int \rho(\mathbf{r}, \mathbf{r}) d\mathbf{r} = \int \sum_{\alpha\beta} \phi_\alpha(\mathbf{r}) K^{\alpha\beta} \phi^*_\beta(\mathbf{r}) d\mathbf{r} = \sum_{\alpha\beta} K^{\alpha\beta} S_{\beta\alpha} \tag{5.18}$$

where we used that $S_{\beta\alpha} = \langle \phi_\beta | \phi_\alpha \rangle$. This leads to

$$N = 2\mathrm{Tr}(\mathbf{KS}) \tag{5.19}$$

for the number of electrons in the system. In the same spirit, combining Eq. 5.5, 5.7 and 5.13, the sum of energy eigenvalues may be written as

$$E = 2H_{\alpha\beta} K^{\beta\alpha} = 2\mathrm{Tr}(\mathbf{KH}) \tag{5.20}$$

where

$$H_{\alpha\beta} = \langle \phi_\alpha | \hat{H} | \phi_\beta \rangle. \tag{5.21}$$

We also define the kinetic energy as

$$E_{\mathrm{T}} = T_{\alpha\beta} K^{\beta\alpha} \tag{5.22}$$

where $T_{\alpha\beta} = \langle \phi_\alpha | \hat{T} | \phi_\beta \rangle$.

By using the exponential localization of the density matrix and imposing a cutoff as in Eq. 5.6, the density kernel and overlap matrices are made sparse. Fast Fourier transforms (FFT) are used in the code to calculate the total energy by calculating the components of the Hamiltonian matrix from Eq. 5.21. This operation is carried out in an "FFT box" [169], independent of simulation cell size: a box, smaller than the simulation cell, is defined in such a way that it only encloses the atoms in the system. This is done by using the fact that the NGWFs are highly localized and set to zero beyond a given radius. By performing the FFTs in this restricted region, we can therefore cast all the operations required to optimize $K^{\alpha\beta}$ and determine the kinetic energy, E_{T}, in terms of sparse matrix algebra operations, which can be carried out in linear-scaling computational effort.

As a linear-scaling code, ONETEP allows for large-scale simulations [170] that a lot of traditional DFT codes would not be able to perform. Some recent works with ONETEP have been applied to a variety of large-scale systems ranging from nanosystems [171, 172] to biomolecular systems with many potential applications [173–175].

5.3 Overview of Soler's method

5.3.1 Original vdW-DF formulation

The form for the exchange-correlation functional proposed by Dion *et al.* [9] is:

$$E_{\mathrm{xc}} = E_{\mathrm{x}}^{\mathrm{revPBE}} + E_{\mathrm{c}}^{\mathrm{PW92}} + E_{\mathrm{c}}^{\mathrm{nl}} \tag{5.23}$$

where $E_{\mathrm{x}}^{\mathrm{revPBE}}$ is the exchange energy from revPBE [106], $E_{\mathrm{c}}^{\mathrm{PW92}}$ is the correlation energy from Perdew-Wang (PW92) [176] and the non-local exchange-correlation energy is given by:

$$E_{\mathrm{c}}^{\mathrm{nl}} = \frac{1}{2} \int \int d\mathbf{r} d\mathbf{r}' \rho(\mathbf{r}) \phi(\mathbf{r}, \mathbf{r}') \rho(\mathbf{r}') \tag{5.24}$$

where $\rho(\mathbf{r})$ is the electron density at $\mathbf{r}$ and $\phi(\mathbf{r}, \mathbf{r}')$ is the vdW-DF kernel, the form of which will be discussed in Sec 5.3.3.

Dion *et al.* start from the following expression for the non-local correlation:

$$E_c^{nl} = \int_0^\infty \frac{du}{2\pi} \mathrm{Tr}\left[\ln(1 - \mathrm{V}\tilde{\chi}) - \ln\epsilon\right] \tag{5.25}$$

where $\tilde{\chi}$ is the density response, V is the electronic Coulomb potential, ϵ is a dielectric function and u an imaginary frequency. This expression for the non-local correlation has its roots in the adiabatic connection - fluctuation dissipation theorem discussed in Sec. 3.2. Eq. 5.25 is then expanded to second order in $S := 1 - 1/\epsilon$:

$$E_c^{nl} = \int_0^\infty \frac{du}{4\pi} \mathrm{Tr}\left[\mathrm{S}^2 - \left(\frac{\nabla \mathrm{S} \cdot \nabla \mathrm{V}}{4\pi}\right)\right]. \tag{5.26}$$

The S is then approximated and written as a functional of the density $\rho(\mathbf{r})$; after a series of of physically justified approximations and mathematical manipulations, they express Eq. 5.26 in a plane-wave basis, which can then be cast into the form of Eq. 5.24. Details on this form and the quantities involved are given in the next sections.

5.3.2 Non-local correlation energy

The direct calculation of the integral in the form of Eq. 5.24 is very computationally expensive, as it involves a six-dimensional spatial integral.

The algorithm proposed later by Roman-Pérez and Soler [2] greatly improves the efficiency of the calculation. They recall that with the form used by Dion *et al.* for ϕ, the above expression can be re-written as:

$$E_c^{nl} = \frac{1}{2} \int\int d\mathbf{r} d\mathbf{r}' \rho(\mathbf{r}) \phi(q, q', r) \rho(\mathbf{r}') \tag{5.27}$$

where $r = |\mathbf{r} - \mathbf{r}'|$, and q and q' are values of the function $q_0[\rho(\mathbf{r}), |\nabla\rho(\mathbf{r})|]$ at $\mathbf{r}$ and $\mathbf{r}'$ respectively. They thus proposed a way to expand the kernel ϕ using interpolating polynomials $p_\alpha(q)$ for chosen values q_α of q, and tabulated functions $\phi_{\alpha\beta}(r)$ for the kernel corresponding to each pair of interpolating polynomials. The interpolating polynomials p_α are cubic splines that evaluate to a Kronecker delta on each respective interpolating point, so $p_\alpha(q_\beta) = \delta_{\alpha\beta}$. A non-uniform mesh of 20 interpolation points is used in Soler's implementation. The Soler

form of the nonlocal energy can be written as:

$$\phi(q_1, q_2, r) = \sum_{\alpha\beta} \phi_{\alpha\beta}(r) p_\alpha(q_1) p_\beta(q_2) \tag{5.28}$$

The universal function $q_0(\mathbf{r})$ is in practice given by:

$$q_0(\mathbf{r}) = \left(1 + \frac{\varepsilon_c^{\mathrm{PW92}}}{\varepsilon_x^{\mathrm{LDA}}} - \frac{Z_{ab}}{9}\Big(\frac{\nabla\rho}{2\rho k_F}\Big)^2\right) k_F \tag{5.29}$$

with $k_F = (3\pi^2\rho)^{1/3}$ and $Z_{ab} = -1.8870$. The quantity q_0 is first "saturated" to limit its maximum value, according to:

$$q_0^{\mathrm{sat}}(\rho, |\nabla\rho|) = q_c\left(1 - \exp\Big(-\sum_{m=1}^{m_c} \frac{(q/q_c)^m}{m}\Big)\right) \tag{5.30}$$

where q_c is the maximum value of the mesh of q_α. The saturation is physically motivated by the fact that q_0 takes high values for large densities, close to the nucleus, in which case the non-local correlation becomes negligible compared to other energy terms.

To evaluate the non-local energy $E_{\mathrm{c}}^{\mathrm{nl}}$, we first define a quantity $\theta_\alpha(\mathbf{r}) = \rho(\mathbf{r}) p_\alpha(q(\rho(\mathbf{r}), \nabla\rho(\mathbf{r}))$ in real space. In terms of this, Eq. 5.24 can be written as:

$$E_{\mathrm{c}}^{\mathrm{nl}} = \frac{1}{2}\sum_{\alpha\beta}\int\int d\mathbf{r} d\mathbf{r}' \theta_\alpha(\mathbf{r})\theta_\beta(\mathbf{r}')\phi_{\alpha\beta}(r) \tag{5.31}$$

It can be shown (App. B) that this can be written as a single reciprocal space integral:

$$E_c^{\mathrm{nl}} = \frac{1}{2}\sum_{\alpha\beta}\int d\mathbf{k}\theta_\alpha^*(\mathbf{k})\theta_\beta(\mathbf{k})\phi_{\alpha\beta}(k). \tag{5.32}$$

This is now much more efficient to calculate. Since the kernel is radially dependent in real space, it is only dependent on the magnitude of the **G**-vectors, hence the kernel need only be evaluated as a one-dimensional function $\phi_{\alpha\beta}(k)$ for each α, β. The kernel ϕ and its second derivatives are transformed to reciprocal space and tabulated for a specific set of radial points. These values are then used to interpolate the kernel at every point $\mathbf{k}$ in reciprocal space required to calculate Eq. 5.32.

5.3.3 Kernel

This section details the evaluation of the vdW-DF kernel. The kernel $\phi(\mathbf{r}, \mathbf{r}')$ as specified by Dion *et al.* [9] is given by (in atomic units):

$$\phi(\mathbf{r}, \mathbf{r}') = \frac{1}{\pi^2} \int_0^\infty a^2 da \int_0^\infty b^2 db W(a,b) T(\nu(a), \nu(b), \nu'(a), \nu'(b)) \tag{5.33}$$

where

$$T(w,x,y,z) = \frac{1}{2}\Big[\frac{1}{w+x} + \frac{1}{y+z}\Big]\Big[\frac{1}{(w+y)(x+z)} + \frac{1}{(w+z)(y+x)}\Big], \tag{5.34}$$

and

$$\begin{aligned} W(a,b) = \frac{2}{a^3 b^3}\Big[&(3-a^2) b \cos b \sin a + (3-b^2) a \cos a \sin b \\ &+ (a^2+b^2-3)\sin a \sin b - 3ab \cos a \cos b\Big] \end{aligned} \tag{5.35}$$

and

$$\nu(y) = 1 - e^{-\gamma y^2/d^2}; \quad \nu'(y) = 1 - e^{-\gamma y^2/d'^2}; \tag{5.36}$$

where $d = |\mathbf{r} - \mathbf{r}'| q_0(\mathbf{r})$, $d' = |\mathbf{r} - \mathbf{r}'| q_0(\mathbf{r}')$

Following this chain of logic, it is clear that this the kernel can in fact be considered as a function only of $|\mathbf{r} - \mathbf{r}'|$, $q_0(\mathbf{r})$ and $q_0(\mathbf{r}')$, since all other variables are dummy variables which are integrated over. The kernel can therefore be written as

$$\phi(r, q_0(\mathbf{r}), q_0(\mathbf{r}')) \tag{5.37}$$

This makes it possible to evaluate the integrals above so as to tabulate the kernel values numerically for a pre-chosen set of radial points and q_0 values, which are then used to interpolate it at intermediate values, in this way avoiding the calculation of the kernel at each grid point. This process is key to the efficient implementation of the vdW-DF.

5.3.4 Non-local potential

Starting from Eq. 5.32, one can evaluate the potential $v^{\mathrm{nl}}(\mathbf{r})$ corresponding to this energy, by evaluating all terms in $\frac{\partial E_{\mathrm{nl}}}{\partial n(\mathbf{r})}$. The non-local potential v_i^{nl} at point $\mathbf{r}_i$ on the grid is thus written explicitly in terms of the derivatives of the

θ_α quantities with respect to the values ρ_j at all other points on the grid:

$$v_i^{\mathrm{nl}} = \sum_\alpha (u_{\alpha i} \frac{\partial \theta_{\alpha i}}{\partial \rho_i} + \sum_j u_{\alpha j} \frac{\partial \theta_{\alpha j}}{\partial \nabla \rho_j} \frac{\partial \nabla \rho_j}{\partial \rho_i}) \tag{5.38}$$

This makes use of the quantities $u_\alpha(\mathbf{r}) = \sum_\beta \mathcal{F}(\theta_\beta(\mathbf{k})\phi_{\alpha\beta}(k))$: which are already calculated in the evaluation of the energy.

Using the White and Bird [177] approach, Eq. 5.38 can be written as:

$$v_{\mathrm{nl}}(\mathbf{r}) = \sum_\alpha \left(u_\alpha(\mathbf{r}) \frac{\partial \theta_\alpha(\mathbf{r})}{\partial \rho(\mathbf{r})} - \int\int i\mathbf{G} \cdot \frac{\nabla\rho(\mathbf{r}')}{|\nabla\rho(\mathbf{r}')|} \frac{\partial \theta_\alpha(\mathbf{r}')}{\partial |\nabla\rho(\mathbf{r}')|} e^{i\mathbf{G}\cdot(\mathbf{r}-\mathbf{r}')} d\mathbf{r} d\mathbf{G} \right) \tag{5.39}$$

For this we need to calculate $\frac{\partial\theta}{\partial\rho}$ and $\frac{\partial\theta}{\partial|\nabla\rho|}$:

$$\begin{aligned}
&\frac{\partial \theta_\alpha}{\partial \rho} = p_\alpha + \rho \frac{\partial p_\alpha}{\partial \rho} \\
&= p_\alpha + \rho \frac{\partial p_\alpha}{\partial q} \frac{\partial q}{\partial \rho} \\
&= p_\alpha + \rho \frac{\partial p_\alpha}{\partial q} \frac{q}{k_F} \frac{\partial k_F}{\partial \rho} + \rho \frac{\partial p_\alpha}{\partial q} k_F \left(\frac{\partial \varepsilon_c}{\partial \rho} \varepsilon_x^{-1} \right. \\
&\left. - \varepsilon_c \varepsilon_x^{-2} \frac{\partial \varepsilon_x}{\partial \rho} - \frac{8}{3(3\pi^2)^{2/3}} \frac{Z}{4} (\nabla\rho)^2 \rho^{-11/3} \right) \\
&= p_\alpha + \frac{q}{3} \frac{\partial p_\alpha}{\partial q} + k_F \rho \frac{\partial p_\alpha}{\partial q} \left(\frac{\partial \varepsilon_c}{\partial \rho} \varepsilon_x^{-1} - \varepsilon_c \varepsilon_x^{-2} \frac{\partial \varepsilon_x}{\partial \rho} - \frac{2Z|\nabla\rho|^2 \rho^{-11/3}}{3(3\pi^2)^{2/3}} \right)
\end{aligned} \tag{5.40}$$

$$\frac{\partial \theta_\alpha}{\partial |\nabla\rho|} = \rho \frac{\partial p_\alpha}{\partial q} \frac{\partial q}{\partial |\nabla\rho|} = \frac{Z}{2\rho k_F} \rho \frac{\partial p_\alpha}{\partial q} |\nabla\rho| \tag{5.41}$$

Combining Eqs. 5.39, 5.40 and 5.41 gives us the final expression for the nonlocal potential.

5.4 vdW-DF flavours

The vdW-DF functionals (Sec. 3.4.4) that we implemented in ONETEP are vdW-DF [9], vdW-DF2 [10], optPBE-vdW, optB88-vdW, optPBE$_{\kappa=1}$-vdW [11], optB86b [178] and also the C09x-vdW by Cooper *et al.* [107] (for both vdW-DF and vdW-DF2 non-local correlation). The motivation for this was that these newly developed functionals offer significant improvements over the origi-

nal vdW-DF, and it is crucial to include them in ONETEP.

Here we briefly show the form for the various exchange functionals. We recall that in vdW-DF the exchange and correlation is split into three parts:

$$E_{\rm xc}[\rho(\mathbf{r})] = E_{\rm x}^{\rm F}[\rho(\mathbf{r})] + E_c^{\rm PW92}[\rho(\mathbf{r})] + E_{\rm c}^{\rm nl}[\rho(\mathbf{r})] \tag{5.42}$$

where F is the name exchange functional. The opt-vdW functionals address the exchange part of Eq. 5.42 and are obtained by calculating binding energies for the S22 set for different values of the parameters in enhancement factors of various known exchange functionals and finding which values of the parameters yield the least mean absolute deviation from the reference data; hence they are optimized. vdW-DF2 changes the exchange functional, but also the non-local correlation functional. C09x only changes the exchange energy.

In vdW-DF2 an alternative exchange is used, which is a refitted version of Perdew Wang 86 [108]. This new exchange functional is termed rPW86 and determined by the enhancement factor

$$F^{\rm rPW86}(s) = (1 + 15as^2 + bs^4 + cs^6)^{1/15} \tag{5.43}$$

with parameters $a = 0.1234$, $b = 17.33$ and $c = 0.163$. The non-local correlation functional is changed by setting the factor Z_{ab} in Eq. 5.29 to -1.8870 instead of -0.8491 as in the original vdW-DF. Mean average deviation for binding energies for the S22 is reduced from 13% (original vdW-DF) to 7.6% for vdW-DF2, with most energies being within 50 meV of the reference values.

Cooper *et al.* [107] proposed the following enhancement factor

$$F_{\rm x}^{\rm C09}(s) = 1 + \mu s^2 e^{-\alpha s^2} + \kappa(1 - e^{-\alpha s^2/2}) \tag{5.44}$$

with μ=0.0617, κ=1.245 and $\alpha = 0.0483$. They named the exchange functional C09x, and it can be used with either vdW-DF or vdW-DF2 correlation, as it was not optimized for a particular non-local correlation. Much better performance is reported, with a 5-9% deviation from CCSD(T) results for the S22 set.

The PBE$_{\kappa=1}$ functional by Klimeš *et al.* [11] is obtained by using the PBE [22, 179] enhancement factor

$$F_{\rm x}^{\rm PBE}(s) = 1 + \kappa - \frac{\kappa}{1 + \mu s^2/\kappa} \tag{5.45}$$

and varying κ (within a given range) only, by keeping μ the same as the original;

the value $\kappa = 1$ is found to give the smallest mean absolute deviation.

The optPBE exchange functional mixes $x = 94.5268\%$ PBE [22, 179] exchange with $(1-x)\%$ RPBE [180] exchange:

$$F_{\mathrm{x}}^{\mathrm{optPBE}}(s) = x\left[1+\kappa-\frac{\kappa}{1+\mu s^2/\kappa}\right]+(100-x). \tag{5.46}$$

The enhancement factor parameter is then optimized for the S22 set and found to be $\kappa = 1.04804$ and $\mu = 0.175519$.

The optB88 exchange functional uses the Becke 88 (B88) exchange [181] and optimizes the parameters in the B88 enhancement factor[1]:

$$F_{\mathrm{x}}^{\mathrm{B88}}(s) = 1+\frac{\mu s^2}{1+\beta s \mathrm{sinh}^{-1}(\mathrm{cs})} \tag{5.47}$$

finding $\mu = 0.22$ and $\beta = 0.1833$.

More recently, there has been another opt-vdW functional proposed by Klimeš *et al.* [178], the optB86b:

$$F_{\mathrm{x}}^{\mathrm{optB86b}}(s) = 1+\frac{\mu s^2}{(1+\mu s^2)^{4/5}} \tag{5.48}$$

which uses the form of the Becke 86 [182] exchange. The value $\mu = 0.1234$ is found to reduce the mean absolute deviation the most.

Out of all the opt-vdW functionals, the one that yields the smallest mean absolute deviation from the reference data of the S22 is the optB88 (10meV) with the worst case being $\mathrm{PBE}_{\kappa=1}$ with 21meV. All of the opt-vdW functionals perform well within chemical accuracy (43meV) for the S22 set.

5.5 Validation tests for vdW-DF

In order to test the validity of our implementation of the vdW-DF flavours, calculations on the S22 set were performed for vdW-DF2, optB88 and optPBE and the mean average deviation (MAD) from reference values was found. Each S22 complex was done for five different displacements, namely 0.9, 1, 1.2 1.5 and 2.0 times the bond length. Calculations were performed with a 8.0 a_0 NGWF cutoff and 1200 eV energy cutoff in ONETEP. Results are shown in Table 5.1.

[1] Actually Eq. 5.47 is not in the form of the original B88, however it can be cast in the present form as is shown in App. C

Table 5.1: Validation tests for vdW-DFs with S22. Mean average deviations (MAD) from reference values are given in meV and kcal/mol. MAD(1.0) is for the S22 complexes at given configuration, whereas MAD(x) corresponds to displacements by x times the bond length. The optPBE and optB88 functionals are within the predicted accuracy of 43meV.

Functional	MAD(1.0)		MAD(0.9,1.0,1.2,1.5,2.0)	
	kcal/mol	meV	kcal/mol	meV
LDA	2.433	105.496	1.686	73.123
PBE	2.592	112.420	1.657	71.843
PBE+D[a]	0.720	31.240	0.596	25.868
vdW-DF2	0.7486	32.460	0.694	30.08
optB88	0.580	25.132	0.512	22.202
optPBE	0.497	21.566	0.632	27.418

[a] PBE with DFT+D dispersion corrections [89]

MAD for LDA, PBE and PBE with semi-empirical dispersion added using the scheme implemented in ONETEP [89] are also given.

Note that the exact values for MAD are not the same as the ones reported by Klimeš *et al.* [11], however we still obtain good accuracy for the whole set. We also find that optPBE performs slightly better than optB88 overall.

5.6 Scaling in ONETEP

We show that scaling with number of atoms with ONETEP is linear both for the total computational time and the time for vdW-DF. We perform calculations with ONETEP using the vdW-DF functional for a fullerene crystal with randomly oriented C_{60} units at the face-centred cubic (FCC) positions in supercell of size $3 \times 3 \times N$ and vary N from 1 to 9. These calculations were performed on the Hartree Centre's BlueJoule facility, a BlueGene IQ, on 12960 cores (1620 MPI processes, each 8-way multithreaded). An NGWF radius of 8.0 a_0 and an energy cutoff of 888.177 eV were used for all the calculations. The computational time against N is shown in Fig. 5.6 for both the total computational time, as well as the computational time to perform the vdW-DF calculations. As expected, scaling with system size is linear. The blue line shows a linear fit to the

data points. Even though it is evident from the data points that this is indeed linear scaling, this fitted line is not the *ideal* scaling. Extrapolating the data points to a line of the form $y = Ax$, which corresponds to the ideal linear scaling scenario (violet line in Fig. 5.6), one can compare the two lines and obtain an idea on how much the real scaling diverges from the ideal case; it is also possible to predict the computational time required for a larger system. In case where a vdW-DF kernel file is not present and has to be created, a small additional time is required at the start of a calculation for its generation. The vdW-DF part of the calculation takes up a fraction of the total computational time but also scales linearly with the number of atoms. In conclusion, the vdW-DF has been successfully implemented in ONETEP, and is now an important function, allowing to perform large-scale calculations with vdW effects taken into account. Various flavours of the vdW-DF are available (vdW-DF2, optPBE$_{\kappa=1}$, optPBE, optB88, optB86b), enabling numerous possibilities for testing on a variety of systems.

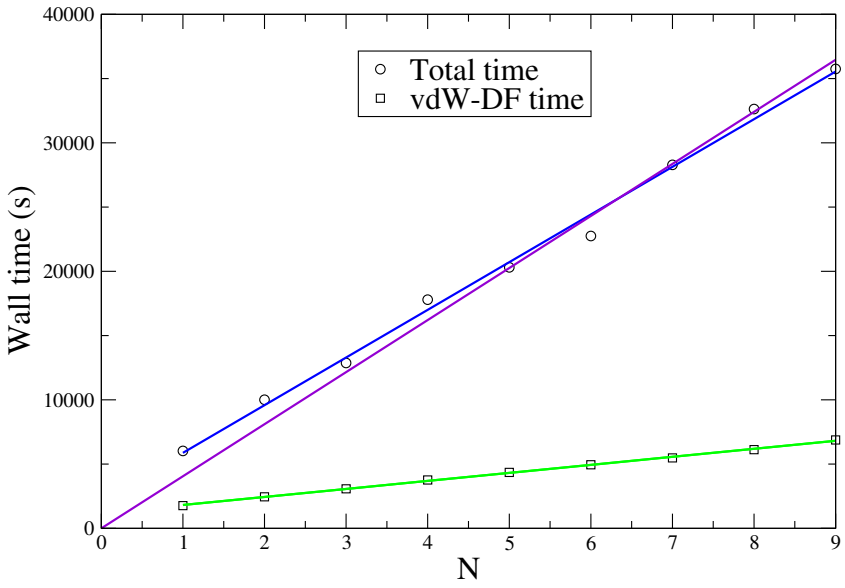


Figure 5.3: Computational time against number of atoms for a C_{60} crystal constructed with randomly rotated units at the FCC positions in a $3 \times 3 \times N$ supercell. Number of atoms per supercell ranges from $3 \times 3 \times 3 \times 60 \times 4 = 2160$ to $3 \times 3 \times 9 \times 60 \times 4 = 19440$. The blue line shows a linear fit to the data points of the total calculation time. In violet, the ideal scaling is shown. The green line shows a linear fit to the vdW-DF individual time. Note that the time for vdW-DF scales as $O(N \ln N)$ asymptotically, but it is dominated by the $O(N)$ part of the calculation.

Chapter 6

Buckminsterfullerene (C_{60})

6.1 Motivation

Having implemented various flavours of vdW-DF functionals in ONETEP, as we saw in Ch. 5, it is important to apply them to a technologically relevant system where van der Waals interactions play an important role, and which is also challenging for traditional DFT methods to simulate. C_{60} is such a system, and it is of great interest to study it with vdW-DF in order to assess the method by comparing to experimental findings, which are widely available for this system. Beyond the theoretical and testing purposes, there are additional reasons to study C_{60}, and particularly C_{60} crystals, as it has been shown that fullerene-derived materials, such as phenyl-C_{61}-butyric acid methyl ester (PCBM) can be used in photovoltaic devices and improve their efficiency [3–5]. Simulating and studying these crystals in detail may potentially be useful to applications.

C_{60}, also known as Buckminsterfullerene or bucky-ball, is a spherical closed structure made entirely of 60 carbon atoms forming pentagons and hexagons on the surface (Fig. 6.1). Specifically, there are 12 pentagons and 20 hexagons. In geometrical terms, C_{60} is a *truncated icosahedron*, which means it is a twenty-side polyhedron of which the vertices have been cut off. The bucky-ball was first produced in 1985 by Kroto *et al.* [12] during graphite vaporization by laser radiation. There was an increased interest in C_{60} crystals shortly thereafter, with extensive experimental work appearing in the early 1990s [183–189].

Because of the near-spherical symmetry of individual C_{60} molecules, there is an associated freedom of rotation of the C_{60} units in bucky-ball crystals. It was

shown in experiment [183] that at low temperatures C_{60} is found in a simple cubic (SC) lattice crystal, while at higher temperatures (> 249 K) it is found in an face-centred cubic (FCC) crystal of orientationally disordered units. The space group of the SC configuration is $Pa\bar{3}$, while the space group of the FCC is $Fm\bar{3}$. The phase transition from the disordered FCC structure to the ordered SC one corresponds to a symmetry change $Fm\bar{3} \rightarrow Pa\bar{3}$. The cubic cell lattice parameter was determined to be 14.04 Å using neutron powder diffraction [183]. The C_{60} bucky-balls in the crystal are rotated around the [111] direction by an arbitrary angle θ, and for some particular angles, this results in the alignment of a hexagon-hexagon (HH) bond on one bucky-ball with the centre of a pentagon on its neighbouring one. David *et al.* [183] find that the structure for $\theta = 98°$ is one where the aforementioned alignment conditions are satisfied. Using neutron powder diffraction, they identify the most stable structure at low temperatures as precisely the $\sim 98°$ one. Their argument as to why $\sim 98°$ is the stable structure relies on electrostatics: the electron-poor pentagons interact more strongly with electron-rich hexagon-hexagon bonds. They report bond lengths of 1.391Å for hexagon-hexagon and 1.455Å for pentagon-pentagon (PP).

Ab initio simulations in 1991, using DFT-LDA, aimed at calculating bond lengths, lattice constants and cohesive energies of C_{60} crystals in the FCC phase and comparing various findings against experimental results. Simulations of the SC crystal were computationally prohibitive at the time, so attention was turned to the FCC structure. The FCC crystal was a feasible calculation, since it only requires one unit of C_{60} in the primitive cell (60 atoms) as opposed to treating the SC structure with four C_{60} units in a cell (240 atoms). Also, availability of functionals at the time was very limited, and LDA was one of the few choices within DFT. Here we briefly summarise three notable examples of such work. Zhang *et al.* [190] find that geometry optimization does not affect the structure of each individual C_{60} unit significantly. They performed geometry optimization with LDA and molecular dynamics. Two different types of bonds are recognized: "single", present only in pentagons, and "double", present in hexagons; it is noted that double bonds alternate with single bonds in hexagons, but since a single bond on a hexagon is automatically a bond of another pentagon on the surface, this distinction comes down to HH and PP bonds. The bond lengths they find are 1.40 Å for HH and 1.45 Å for PP. Saito *et al.* [191] used LDA with Gaussian basis sets for their work to calculate cohesive energies, which they estimate as 1.6eV, close to the experimental value, 1.65eV, from Ref. [192]. Troullier and Martins [193] use LDA to study the FCC C_{60}, finding good agreement with

experiment: bond lengths are found to be 1.382 Å for HH and 1.444 Å for PP, lattice constant 14.0 Å, and cohesive energy 1.6eV per molecule. Note that all these three studies find very similar results, and all compare well against experimental data.

A quite in-depth review by Andreoni [194] in 1998 presented all the different efforts at studying C_{60} and derivatives with computational simulations up to that time. Computational simulations were also done with methods other than DFT: Hartree-Fock were also used to study C_{60} [195] but they do not perform as well as LDA.

In 2005, Tournus *et al.* [196], using the SIESTA [152] DFT code, made an orientation analysis on the C_{60} dimer to identify the energetically more stable structure. While a dimer is not an accurate representation of the full crystal, it can help in providing some very useful insight on what the ideal angle of rotation for the most energetically stable structure is. Cohesive energies and lattice parameters were also studied. In their work, they looked at how various bond-centre of pentagon (or bond-centre of hexagon) alignments affect the total energy, and find agreement with experiment. A second minimum of energy as a function of rotation angle is also found at $\sim$38°, which is less structurally stable than the $\sim$ 98° minimum. They argued that while the electrostatic arguments made by David *et al.* [183] regarding bond-pentagon alignment may be part of the reasons why the $\sim$98° is the most stable structure, it is not a complete explanation. The lattice parameter was estimated to be 14.03 Å, which is very close to the experimental value of 14.04 Å. The cohesive energy was estimated to be $\sim$ 1 eV per C_{60} unit, which is in significant disagreement with the experimental value [192] of 1.65eV that they compare against. For comparison, we note that the database for experimental sublimation energies of various systems by Chickos *et al.* [197] reports values in the range of 1.6-1.9 eV for C_{60}. Tournus *et al.* state in their work that LDA is an adequate functional for studying C_{60} as it has been successful in describing the C_{60} structure. However, even though they obtain encouraging results compared to experimental values for the lattice parameters, and structural properties of C_{60}, it could be argued that the agreement of LDA with experiment is fortuitous, since no explicit treatment of vdW interactions is present.

Recently Berland *et al.* [198] studied the SC $\sim$ 98° C_{60} crystal with various flavours of vdW-DF: the original vdW-DF, vdW-C09, optPBE-vdW and vdW-DF2. For vdW-DF they obtain 14.38 Å for the lattice constant and 1.7 eV cohesive energy; for vdW-C09 14.10 Å and 1.98 eV; for optPBE-vdW 14.22 Å

and 2.02 eV and for vdW-DF2 14.30 Å and 1.30 eV. All these values are close to the experimental ones. It was concluded that the alternative exchange vdW-DFs perform worse in terms of cohesive energies but lattice parameters are improved compared to the original vdW-DF. It was also concluded that the optPBE-vdW functional, which is based on fitting to the S22 set, does not guarantee better performance for other systems such as C_{60} in this case. Finally, the performance of vdW-DF2 was found to be satisfactory compared to experiment. More recent work by Berland *et al.* focuses on testing vdW-DFs on adsorbates of benzene and C_{60} on graphene and boron nitride, opening up another, different direction for this type of work.

In conclusion, the structural aspect of C_{60} crystals has been extensively studied both experimentally and with *ab initio* simulations, with the main finding being that there exists an energetically favoured SC structure at angle of rotation by [111] of $\sim 98°$, and another structure, less energetically favoured, at $\sim 38°$. This also agrees with theoretical works utilizing a rotational potential to identify these structures [199]. The wide availability of experimental and theoretical work on C_{60} crystals makes this system an attractive option for testing vdW-DFs. Quoting Tournus *et al.*: *"We should also try to go beyond the inaccurate description of Van der Waals interactions due to the use of LDA, but the study of such large systems is still a challenge for present day simulations."* Berland *et al.* have began this effort, but to our knowledge, vdW-DF calculations for the *whole range* of different configurations (rotation angles) on the SC structure of crystal C_{60}, have not been performed to date. In this work, we address exactly this deficiency. We will attempt to assess the adequacy and accuracy of various vdW-DF functionals for studying C_{60} crystals within linear-scaling DFT, as a first step towards the use of these methods to study a range of similar weakly-bound molecular crystals.

6.2 Structure

We now describe the structure of C_{60} in more detail. As was mentioned in Sec. 6.1, at low temperatures there is a phase transition from an FCC disordered crystal to an ordered SC structure. This transition corresponds to a $Fm\bar{3} \rightarrow Pa\bar{3}$ change of symmetry. The $Pa\bar{3}$ group is defined by the following operations (reflections, translations):

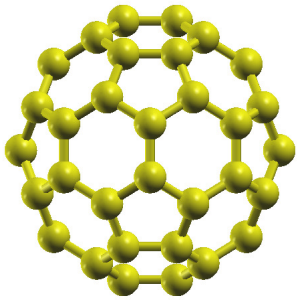


Figure 6.1: Single, perfectly symmetric truncated icosahedron, with all bond lengths equal. A bucky-ball is a truncated icosahedron with two different bond lengths. The carbon atoms form a surface comprised of pentagons and hexagons. Hexagon bonds are alternating, while pentagon bonds are the same.

$$
\begin{aligned}
&(+x,+y,+z);(+z,+x,+y);(+y,+z,+x);\\
&(1/2+x,1/2-y,-z);(1/2+z,1/2-x,-y);(1/2+y,1/2-z,-x);\\
&(-x,1/2+y,1/2-z);(-z,1/2+x,1/2-y);(-y,1/2+z,1/2-x);\\
&(1/2-x,-y,1/2+z);(1/2-z,-x,1/2+y);(1/2-y,-z,1/2+x);\\
&(-x,-y,-z);(-z,-x,-y);(-y,-z,-x);\\
&(1/2-x,1/2+y,+z);(1/2-z,1/2+x,+y);(1/2-y,1/2+z,+x);\\
&(+x,1/2-y,1/2+z);(+z,1/2-x,1/2+y);(+y,1/2-z,1/2+x);\\
&(1/2+x,+y,1/2-z);(1/2+z,+x,1/2-y);(1/2+y,+z,1/2-x);
\end{aligned}
$$

where x y and z are the cartesian coordinates of a point, and $\mathbf{r}_i + 1/2$ denotes a translation of a coordinate by $1/2a\mathbf{r}_i$ where a is the lattice parameter of the cell.

It is clear from these transformations that the units are at the face-centred cubic positions, but since the units are also rotated, as we will see later, the primitive cell contains four different units (Fig. 6.2), resulting in a simple cubic lattice.

It is useful to note that the ideal configuration for one C_{60} unit can be

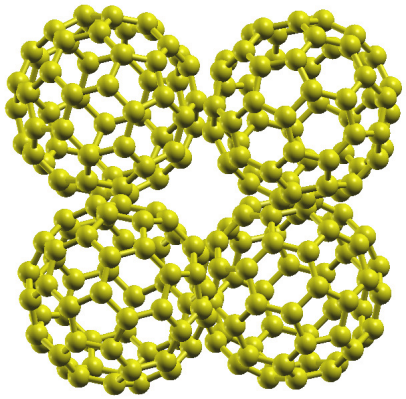


Figure 6.2: The four units of the primitive cell in a C_{60} crystal for $\theta = 98°$. This angle produces the best alignment of an HH bond of one bucky-ball to the centre of a pentagon in a neighbouring one.

reproduced using the following coordinates [183]:

$$\alpha(0, \pm\frac{1}{2}, \pm\frac{3}{2}\tau)\ \circlearrowleft; \alpha(0, \pm\frac{1}{2}, \pm\frac{3}{2}\tau)\ \circlearrowleft; \alpha(0, \pm\frac{1}{2}, \pm\frac{3}{2}\tau)\ \circlearrowleft \tag{6.1}$$

where $\tau = (1+\sqrt{5})/2$ and α is the ratio of average C-C distance to cubic lattice constant, and $\circlearrowleft$ denotes a cyclic permutation (note that the cyclic permutation in this case includes all combinations of (+) and (-) terms). This yields a *perfectly symmetric* structure, with all bond lengths being equal, and therefore does not correspond to a real bucky-ball. Keeping in mind that geometry optimization will be performed, this provides a good starting point.

To generate the crystal, we first use the single symmetric C_{60} from Eq. 6.1, rotate it anti-clockwise by the [111] direction by angle θ, and then apply the $Pa\bar{3}$ symmetry transformations, as described by David *et al.* [183]. Note that for this set of rotations, the angle 0° is equivalent to 120°, so only the range 0-120° is needed. Since the single ideal C_{60} unit inherently has some symmetries present in the $Pa\bar{3}$ group, there are many degenerate points when the $Pa\bar{3}$ transformations are applied. Consequently, only *four* (counting the unit at the origin) transformations are required to obtain the full crystal, namely:

$$(+x, +y, +z);$$
$$(1/2 + x, 1/2 - y, -z);$$
$$(-x, 1/2 + y, 1/2 - z);$$
$$(1/2 - x, -y, 1/2 + z);$$

From this set of transformations, it can be seen that the four C_{60} units in a cell each have reflections in different axes.

6.3 Applications

6.3.1 Calculation details

Calculations on the C_{60} crystal were performed using ONETEP, on 5×12-core nodes (60 cores total), using the cx1 High-performance Computing (HPC) facility. Cell size was based on the experimental lattice constant, taken from Ref. [183], $a = 14.04078$ Å, and varied in small increments in order to find the minimum value for the energy. Geometry optimization was performed at each size. Psinc grid spacing was set to ~ 0.22 Å and increments in lattice parameter were initially made in even steps of psinc spacings. Some calculations, especially near the minimum were done without this restriction. The value of the psinc spacing, however, was still close to the original one. In cases where a different psinc spacing was used, there were small egg-box effects. The egg box effects are manifested when a different space grid is used in the simulation, due to differences in sampling caused. In all cases, the cutoff energy associated with the psinc grid was no less than 1000 eV, which ensured convergence. The NGWF radii used for all calculations were 9.0 a_0. For the geometry optimization a 2×10^{-4} Ha/Bohr force tolerance was used. To calculate the energy of a single bucky-ball, a large cubic supercell was chosen (~ 36 Å) to remove interactions with periodic replicas. The other parameters were kept the same. The functionals PBE, LDA, vdW-DF2, optB88-vdW and optPBE-vdW were used to study the crystal. This choice was based on the fact that previous calculations on C_{60} by Berland *et al.* were done with the original vdW-DF, vdW-C09, optPBE and vdW-DF2; our aim was further investigate the opt-vdW and vdW-DF2 functionals, as they are more recent and have generally been successful, particularly

optB88, which is known to perform very well on the S22 set.

6.3.2 Orientational dependence of total energy

Having constructed the crystal as described in Sec. 6.2, we vary the lattice parameter and obtain curves for the cohesive energy against lattice parameter for a range of angles 0 to 120°, by the relaxed minimum energy configuration at each angle. We calculate the cohesive energy

$$E_{\mathrm{coh}}(\theta) = E_{\mathrm{tot}}^{\mathrm{crystal}}(\theta) - 4E_{\mathrm{single}} \tag{6.2}$$

where $E_{\mathrm{tot}}^{\mathrm{crystal}}(\theta)$ is the total energy of the crystal (with four units per unit cell) and depends on the angle of rotation around [111], θ, and E_{single} is the total energy of a single bucky-ball. PBE, as expected, does not bind (Fig. 6.3) and therefore a full energy vs angle curve could not be obtained since there were no minima for the energy vs lattice parameter curves. Fig. 6.4 shows two binding curves for the optPBE-vdW functional, for 43° and 98°. Angles were varied by 10° for most points, and specifically by 1° around the minima in the case of optPBE and optB88, and by 20° for all other functionals, as we chose to focus on the opt-vdW functionals. The minimum energy of each structure at different angles is then estimated by performing a quadratic fit to the points near the minimum in the binding curves. Finding the minimum energy for each angle, we then create sets of energy vs angle curves for all functionals, and identify which angle yields the global minimum energy configuration.

LDA predicts a global minimum at 98°, in agreement with experimental and theoretical research [183,199]. We find that for all the vdW-DF functionals studied here, there is another well-distinct configuration around 43.5°, which in fact has lower energy than the configuration at 98° (Fig. 6.5). The configuration at $\sim 98°$ might be expected to be energetically favoured since by construction the rotation at this particular angle aligns electron-poor pentagons with HH bonds. However, the same holds with the $\sim 43.5°$ structure, but now hexagons instead of pentagons are aligned with bonds (Fig. 6.6). Despite theoretical [199] and *ab initio* works [196] predicting another minimum at 38°, higher in energy than the 98°, we find that the 43.5° structure is favoured energetically before and after geometry optimization. The energies of the 98° and 43.5° structures differ only by about $0.17 - 0.2$ eV for optPBE and optB88, so these minima are nearly degenerate. In Fig. 6.7 we show a close-up curves of cohesive energy

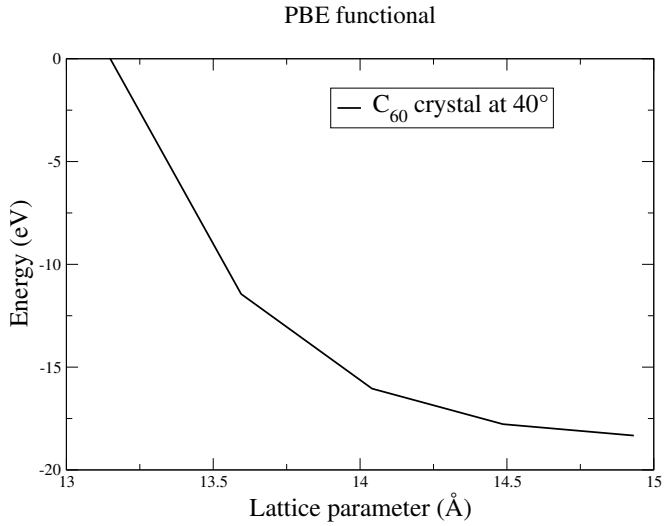


Figure 6.3: Energy vs lattice parameter for PBE. This functional does not bind, so could not be used further to produce energy vs angle curves. A zero of -1375.5749 Ha was chosen, corresponding to the largest value of energy from the data available for this curve.

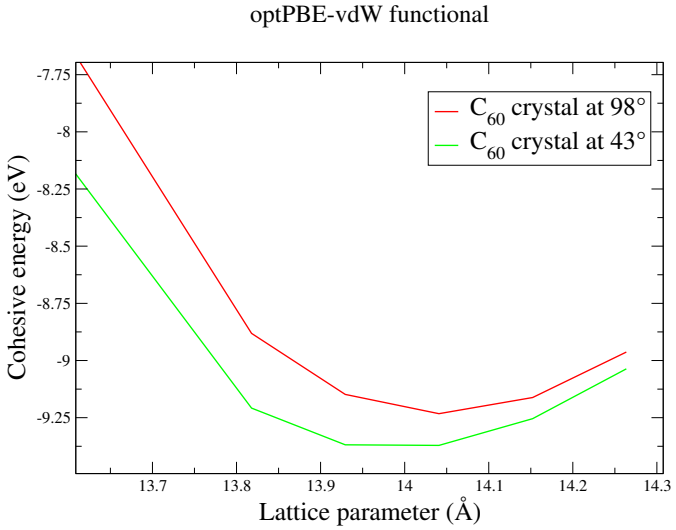


Figure 6.4: Two energy vs lattice parameter binding curves for the 43° and 98° structures. These were used to produce a minimum energy which was then used to draw a minimum energy vs angle curve, in order to assess which structure is the most stable. This was done for all functionals except PBE, which does not bind.

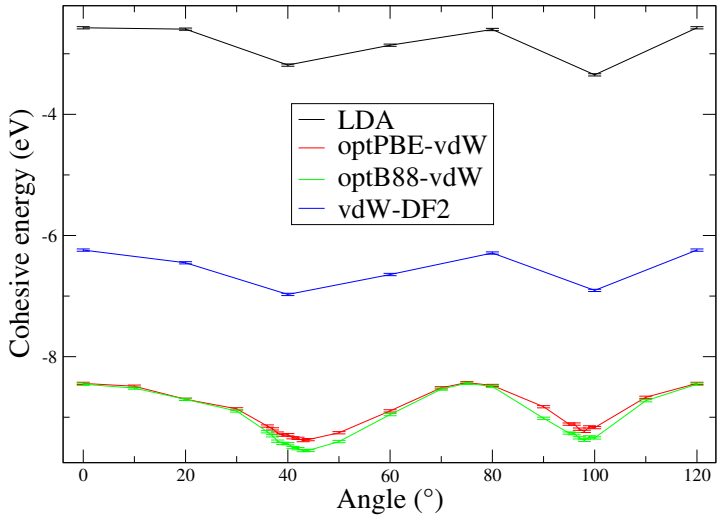


Figure 6.5: Energy vs angle of rotation by [111] for all functionals studied here. The error bars are added because there are egg-box effects that result in an error of approximately ∼0.02 eV, which was quantified by performing a calculation on a single bucky-ball under various rotations.

vs angle for the two opt-vdW functionals we studied. We note that in all the energy vs angle curves, we have added error bars to account for small egg-box effects, which were found to be of the order of ∼0.02 eV.

One way to quantify how well the centre of a hexagon (or pentagon) is aligned along the [110] [101] and [011] directions can be defined, denoted δ. δ determines the deviation from the [110] direction, since in the crystal only a [11δ] direction can occur, and it is actually impossible to have a structure where the alignment with [110] is perfect. It may be used as an indication of how well a bond aligns with the centre of a pentagon or hexagon of a neighbouring C_{60}, since the centres of bucky-balls lie on the planes defined by these vectors. We find that after geometry optimization, $\delta_{98} = -0.05249$ and $\delta_{38} = -0.29734$, are the global minimum values. This reinforces the fact that structurally the 98° structure has the best alignment possible between bonds and pentagons in neighbouring bucky-balls. The δ_{98} value is in agreement with the value $\delta = -0.05218$ from Ref. [183]. The fact that the 38° structure is one where there is an ideal alignment of bond to centre of a hexagon is in agreement with theoretical work Ref. [199]. However, the concept of δ becomes much less useful as one moves away from these two configurations, since in these cases there are large devia-

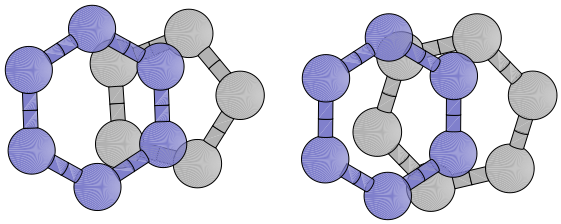


Figure 6.6: HH bond - pentagon/hexagon alignment in the cases of Left: $\theta = 98°$, Right: $\theta = 38°$. The rings out of the plane of the paper are coloured in violet.

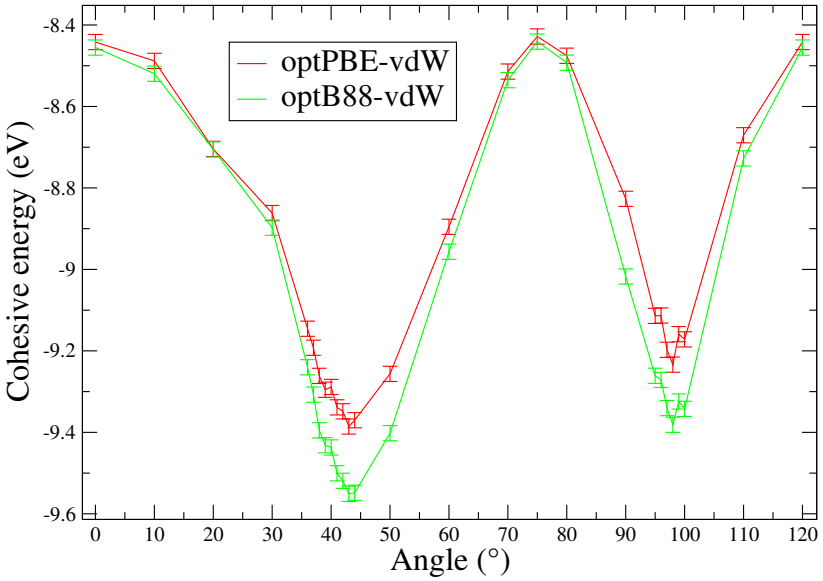


Figure 6.7: Cohesive energy vs angle of rotation by [111] for optPBE-vdW and optB88-vdW. This data is the same as Fig. 6.5; the curves are shown in close-up here. Error bars are added to account for small egg-box effects.

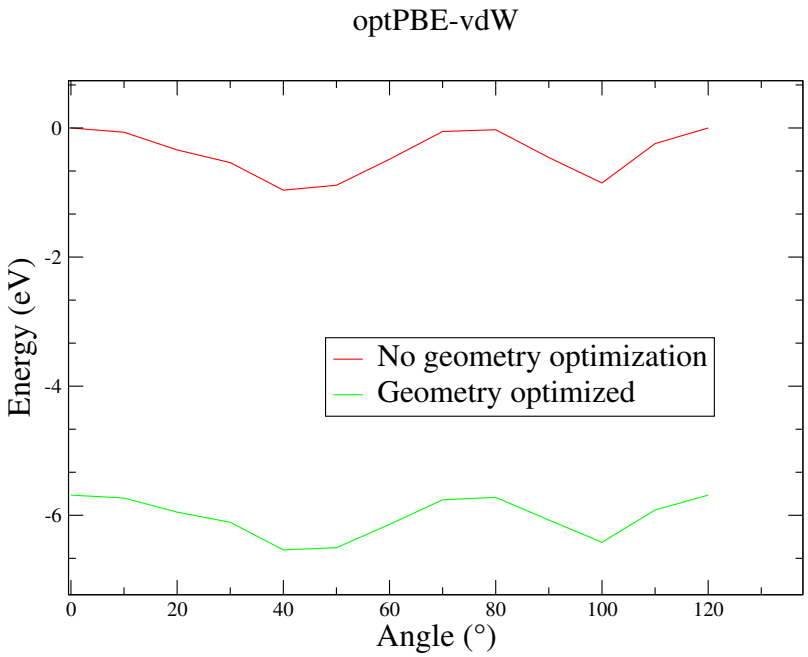


Figure 6.8: Energy vs angle curve before and after geometry optimization for optPBE-vdW. This graph illustrates how much energy is gained by a geometry optimization, typically $\sim$ 5.44 eV. A zero of -1381.1085 Ha was chosen, corresponding to the geometry unoptimized energy at angle 0.

tions even in the other axes: the centres of pentagons or hexagons are aligned along a $[1,1+\zeta,\delta]$ direction (or equivalently $[1,\delta,1+\zeta]$ etc), where ζ is another small deviation. It is possible that the electronic density of hexagons in the case of $\theta = 43.5°$ is responsible for our finding with optPBE-vdW and optB88-vdW, that $\theta = 43.5°$ is a lower-energy structure than the 98° one. Geometry optimization does not affect alignment significantly, only outward radial expansion of C_{60} buckyballs is observed, and lowering of the total energy of typically around 5.4 eV (Fig. 6.8). Broadly speaking, after geometry optimization, alignment is kept the same, but distance between atoms becomes smaller, resulting in stronger attraction of bonds with pentagons/hexagons in the minimum structure cases, or other types of interactions in other structures at other angles. Bond lengths also change with geometry optimization; details of to this will be discussed later.

6.3.3 Lattice constants, cohesive energy and bond lengths

Beyond the orientational aspect of the structure of C_{60} crystal, it is also very interesting to look at the lattice parameters, bond lengths and cohesive energies of the system for a particular configuration. As mentioned before, given that there is a wide range of data available for crystal C_{60} lattice parameters, cohesive energies and bond lengths, it is useful to compare our results for these quantities to experimental values. We also compare our results to Berland *et al.* [198], particularly for the opt-vdW functionals. We chose to do so for the 98° structure, as it is the one that was also investigated by Berland *et al.* and is also the experimentally observed structure at low temperatures. We mostly concentrate on the opt-vdW functionals, and note again that the data for our LDA and vdW-DF2 calculations is more sparse, as we only wished to obtain a general idea of how they perform.

The most direct experimental comparison is to relate the cohesive energy to the measured sublimation energy (the energy required for a gas-to-solid phase transition to occur) [197, 200, 201]. As was previously mentioned that values from experimental work on the cohesive energy mostly fall in the range 1.6-1.9 eV [192,197]. Note that all experimental studies on sublimation energies are temperature dependent and were done at high temperatures (> 540 K). However, there are works [200,201] that have extrapolated experimentally measured sublimation energies down to lower temperatures. Chirico *et al.* [200] extrapolated the sublimation energy obtained by Pan *et al.* [188] down to 298.15 K and found $E_{\text{sub}} = 234$ kJ/mol, or 2.425eV. Diogo *et al.* [201] extrapolate the sublimation energy calculated by Matthews *et al.* [202], also down to 298.15 K and found $E_{\text{sum}} = 228.7$ kJ/mol, or 2.37 eV. We compare these results against the cohesive energy we obtained with optPBE and optB88 in Table 6.1. Keeping in mind that the simulations are done in zero temperature, it may be argued that comparing against extrapolated sublimation energies to lower temperatures is a better choice to gauge performance of functionals. As it can be seen from Table 6.1, the lattice parameter we obtain with optPBE-vdW is in excellent agreement with the experimental value, while the value from optB88 is also in good agreement. In addition, comparing our cohesive energy of the 98° structure, for both optPBE and optB88, to the sublimation energy from Refs. [200, 201], we also see they agree remarkably well. For the $\theta = 100°$ structure, vdW-DF2 is also in reasonable agreement with experimental values, yielding 14.16Å for the lattice parameter and 1.73 eV for the cohesive energy. Again for the $\theta = 100°$ structure,

Table 6.1: Lattice parameters and cohesive energies per molecule for the 98° C_{60} crystal structure with the opt-vdW functionals obtained in this work and compared against previous work with optPBE only by Berland *et al.* [198], and also experimental values. The lattice parameter with optPBE in this work is in excellent agreement with the experimental value. Cohesive energies agree with the extrapolated experimental sublimation energies to 298.15 K. The discrepancies between this work with optPBE and Berland's work on the same functional are thought to be due to different calculational parameters, but mostly due to geometry optimization that was done in this work.

Method	Lattice parameter (Å)	Cohesive energy (eV)
optPBE[a]	14.05	2.31
optB88[a]	13.93	2.34
optPBE[b]	14.22	2.02
Exp.[c]	14.04	1.60-2.42

[a] This work
[b] Berland *et al.* [198]
[c] Ref. [197, 200, 201]

LDA yields a reasonable lattice parameter, 13.92 Å, however the cohesive energy is underestimated, giving 0.87 eV. Contrary to the conclusion of Berland *et al.* that opt-vdW functionals do not perform particularly well for C_{60}, we argue that optPBE may in fact be a very adequate choice for studying molecular crystals, the only drawback being that the 98° structure is not predicted as the most energetically favoured, as was mentioned in Sec. 6.3.2. We attribute the differences between the optPBE functional in our work and Berland *et al.*'s work to different calculational details, but mainly the fact that we performed geometry optimization which is also very likely the reason for much better agreement of the lattice parameter against the experimental one, suggesting that relaxation of structures is an important factor, particularly when using vdW-DFs.

Finally, we look at bond lengths. In Fig. 6.9 we show bond lengths obtained with optPBE for the 98° structure after geometry optimization, and compare against the experimental values by David *et al.* [183]. We obtain values centred around 1.38 Å for HH bonds and 1.44 Å for PP bonds; experimental values are 1.391 Å for HH and 1.455 Å for PP. The agreement is reasonable, and results

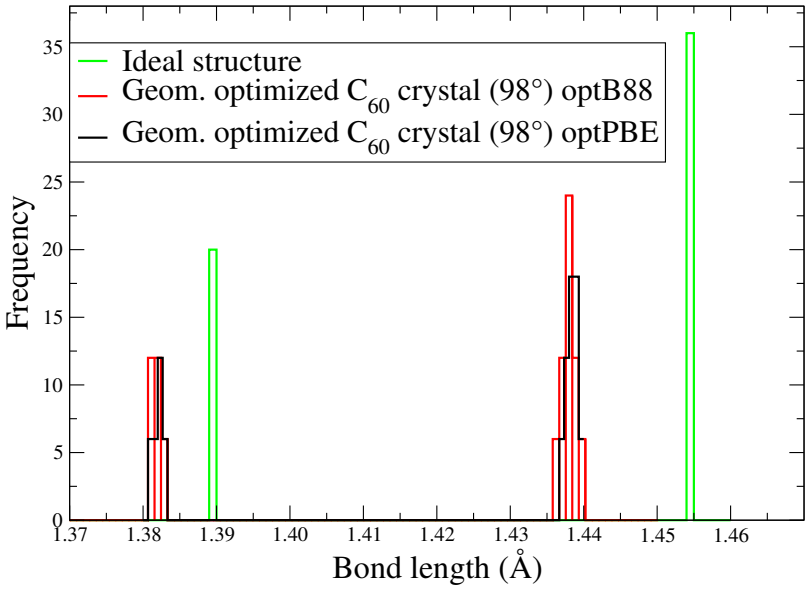


Figure 6.9: Frequency of bond lengths for the ideal structure (in which there are two different bond lengths), with average values taken from experiment [183] for the idealized structure, compared to the distribution of bond lengths after geometry optimization has been performed with the optPBE and optB88 functionals for the 98° structure.

are also on par with previous works, predicting 1.38-1.40 Å for HH bonds and 1.44-1.45 Å for PP bonds [190, 193].

6.3.4 Rotational freedom

A question that arises is how free are the bucky-balls to rotate in the crystal. Differences in energy between the different functionals are larger than differences between different angles within the same functional, which indicates that there is not much freedom since there is a relatively "flat" energy landscape. A calculation was done with vdW-DF on a $3 \times 3 \times 3$ supercell with one orientationally defective C_{60} unit rotated by 8-118° around [111] in steps of 2°. The other units were fixed as in the $\theta = 98°$ structure. The energy vs angle curve is shown in Fig. 6.10. We see that the maximum difference of energy is about 0.2 eV at around 25°. This is close to the value of energy difference between the 43.5° and 98° in the SC C_{60} crystal, which points in the direction that this is the order of energy difference between two stable configurations. We also note that there is

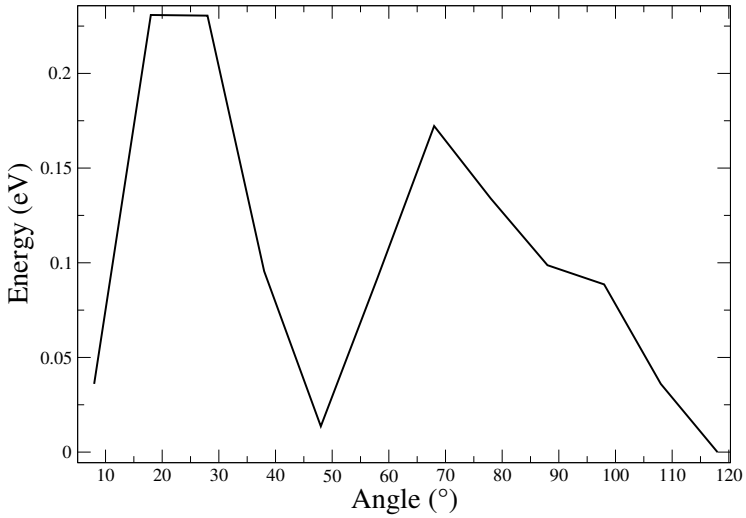


Figure 6.10: Energy curve vs angle for an orientationally defective C_{60} crystal with vdW-DF. In a $3 \times 3 \times 3$ supercell, one C_{60} unit was rotated by angle θ, while the other units were as in the $\theta = 98°$ structure. The total energy was calculated for the 8-118° range of angles. The zero was been chosen to be at the lowest energy configuration (118°), at -37385.26177 Ha.

a minimum around 48°, which is interesting to compare to the minimum energy structure we find at 43.5°. Rotational freedom of C_{60} is a topic that could be of great importance and will be explored further.

6.4 Conclusion

In conclusion, we have studied the C_{60} crystal with ONETEP, using five different functionals: LDA, PBE, vdW-DF2, optB88-vdW and optPBE-vdW; PBE does not bind the crystal, and the agreement of LDA regarding the most stable structure is fortuitous. The two opt-vdW-DF functionals performed well in terms of lattice parameters, which were found to be in good agreement with experiment. Comparing against the extrapolated data of Chirico *et al.* we also find good agreement for the cohesive energies predicted by the optPBE and optB88. Geometry optimization with vdW-DFs seems to be an important factor in predicting accurate geometries and cohesive energies. Structural properties of the crystal in terms of two well-distinct configurations that yield energetic minima were successfully predicted by all functionals. The 98° structure was

identified as a minimum by the vdW functionals, but its energy was found to be higher than the 43.5° structure, in slight disagreement with theoretical [199] and *ab initio* [196] works predicting a second, less energetically favoured structure at 38°. Other than that discrepancy, we argue that the opt-vdW functionals are well-suited for studying molecular crystals, since there is excellent agreement for the lattice constant obtained in our optPBE calculations with the experimental value [183] and good agreement is obtained with optB88. Moreover, since the angular landscape has not been explored thoroughly with *ab initio* methods, it is possible that the $\theta = 43.5°$ is indeed the most stable one. It can also be argued that the cohesive energy we obtain for the 98° structure is not an unreasonable one, since there are at least two experimental works [200, 201] that have extrapolated experimentally determined sublimation energies for gas-to-solid phase at high temperatures, down to 298.15 K, suggesting sublimation energies in the range 2.37-2.42 eV. This suggests that it is a better choice to compare against lower temperatures, since simulations are done at 0 K. One could in principle extrapolate the experimental results down to 0 K or the theoretical results to 298.15 K by calculating vibrational free energies in order to obtain a better idea of how well the simulations match the experiment. If vdW-DFs can be made sufficiently accurate to predict the correct structure, geometries and energies of molecular crystals, that can be of great interest to the pharmaceutical industry as it may aid prediction of crystal structures of candidate drug molecules.

Chapter 7

Conclusion

The aim of this thesis was to study, implement and test methods to include van der Waals interactions within the density functional theory framework. We presented our work and put it into context within the field. A theoretical background for the main methods used in our work was given and the advantages and limitations of various methods for computational simulations were discussed. Density functional theory, remarkably, allows the use the ground state density as the fundamental variable for solving for the ground state of the $3N$ many-body quantum mechanical problem instead of the full wavefunction. A series of approximations and approaches reduce this to a very tractable problem, which can be solved computationally with relative ease. DFT has been shown to perform very well for a variety of systems. The local nature of commonly used approximations to exchange and correlation within DFT, however, fails to capture a number of long-range non-local effects, such the vdW interactions.

vdW interactions arise from interacting fluctuating dipoles separated by large distances. They are of great importance for weakly bound systems such as molecular crystals, where ionic or covalent interactions are absent. The accurate description of vdW is a whole topic on its own, with a very rich literature of research attempting to answer this question. The topic of vdW interactions within the DFT framework is particularly challenging at both the methodological and computational level, since one would want a method that is developed on the basis of well-justified physical approximations, as well as being computationally efficient. Recently, there have been many new methods treating vdW in DFT with various levels of success and efficiency, moving in a constantly improving direction. In this thesis, we focused on two such methods, which we

have implemented and tested.

The first method, proposed by Silvestrelli [1] makes use of maximally localized Wannier functions (MLWFs), which are unitary transformations of the Bloch eigenstates and localized in real space, to partition the electronic density of a system, and then applies some approximations in order to efficiently calculate dispersion coefficients which are then used to calculate the vdW correction to the total ground state energy. We implemented this method and tested it on a number of vdW-bonded systems, from an argon dimer to a copper phthalocyanine dimer. We found that the method has some limitations and shortcomings, mainly arising from the breaking of symmetries inherently present in the system by the valence MLWF centres. We addressed these problems by proposing a different partitioning of the density, involving a larger manifold of MLWFs which also includes unoccupied states; in this way we are able to restore symmetries and improve binding energies significantly and find good agreement with CCSD(T) [68] for ethene and benzene dimers. Applying this method to a phthalocyanine and copper phthalocyanine dimer, we found reasonable agreement with DFT+D methods [84] and other works on metal phthalocyanines [139]. We also addressed the case of spin-polarized systems, such as copper phthalocyanine, in which case we find that cocentric MLWFs corresponding to different spin channels have to be amalgamated since this method is strictly for non-overlapping fragments of density. We concluded that even though this method can be made more accurate by using our modifications, it is limited to the study of smaller and less structurally complex systems, as it requires a high level of manual effort and chemical intuition in order to choose an appropriate set of MLWFs. This procedure could in principle be automated, however it would then be limited by the computational bottlenecks associated with cubic-scaling DFT for the original ground-state electronic structure simulation.

We then turned our attention to the vdW-DF method, proposed by Dion *et al.* [9], which calculates dispersion interactions using a non-local energy functional, allowing a fully *ab initio* treatment of vdW within DFT. We implement the vdW-DF scheme using Román-Pérez and Soler's efficient algorithm [2], which allows the calculation of the non-local correlation functional in $O(N \log N)$-scaling computational effort, within ONETEP, a plane-wave accuracy linear-scaling package. The motivation behind this was that a fully *ab initio* method for vdW was not present in ONETEP and vdW-DF has had a number of successes in treating dispersion; also, being able to simulate large dispersion-bonded systems is of great importance for expanding the scope of applications, a lot of

them being technologically relevant. Various flavours of vdW-DF that significantly improve its performance by making changes to the exchange [11] and/or non-local correlation part [10] of the vdW-DF functional were also implemented in ONETEP.

Finally we applied the vdW-DF method in ONETEP to C_{60} crystals. The choice of this system was based on the widely available experimental data determining its lattice parameters, bond lengths, sublimation energies and observed configurations, which offers a solid ground for testing. C_{60} was created in 1985 [12] and studied extensively in experiment during the 1990s. It is known that at low temperatures, C_{60} is found in the form of a simple-cubic (SC) crystal and is orientationally ordered, while at higher temperatures there is disorder and the crystal is face-centred cubic (FCC). The space group of the SC crystal is $Pa\bar{3}$ where the individual C_{60} units are rotated around the [111] direction by angle θ, reflected under different axes and translated at the FCC positions. The unit cell then has four C_{60} molecules. Using ONETEP and the LDA [176], PBE [179], vdW-DF2 [10], optPBE and optB88 [11] functionals, we studied the crystal in its various configurations and calculated cohesive energies, lattice parameters and bond lengths. Geometry optimization was performed at each configuration. We found that LDA predicts the $\theta = 98^\circ$ structure as the most stable, in agreement with experiment, but this agreement is largely fortuitous. PBE did not bind the crystal. All the vdW-DF functionals we looked at predicted another, more stable structure at $\theta = 43.5^\circ$. A $\theta = 38^\circ$ structure, less energetically stable is instead predicted by other *ab initio* [196] and theoretical works [199]. However, the entire landscape of angularly dependent energies hadn't previously been explored with *ab initio* methods, and it is possible that our predicted $\theta = 43.5^\circ$ structure is indeed the most stable one. For the optPBE functional, we found excellent agreement for the lattice parameter with the experimental value [183], and good agreement with optB88. Cohesive energies of optPBE and optB88 agree well with experimental values extrapolated to 298.15 K [200, 201], which we argue is a better comparison than values at higher temperatures, since simulations are done at 0 K. Bond lengths were in reasonable agreement with experiment [183], and within the range of previous *ab initio* calculations [190, 193]. We concluded that the optPBE and optB88 functionals are an appropriate choice for studying molecular crystals and argue that the discrepancies of our work against Berland *et al.* [198] with optPBE and vdW-DF2 are due to the fact that we performed geometry optimization, which seems to be an important factor in getting better energies and geometries. With the advantage of having the vdW-DF available

in a linear-scaling code, one can look at orientationally defective crystals of very large size. As the accuracy of newly-developed vdW-DFs increases, it will be possible to accurately predict structure and energetics for molecular crystals which can be of great importance to the pharmaceutical industry.

In general, the field of vdW interactions in electronic structure consists of a variety of methods that can be used to study a broad range of systems, with some methods being more geared towards specific applications, so sometimes care has to be taken when choosing a method. It is a fast-evolving and constantly improving field with significant efforts being made to develop more accurate and more efficient methods at an impressive rate.

Future work on vdW within linear-scaling DFT with ONETEP may involve the implementation of the Vydrov and Van Voorhis functional, VV10, which is based on the vdW-DF formulation but makes use of a more complicated expression for the kernel. The method has been shown to perform well for a number of systems [117]. It would be an ideal addition to ONETEP and would expand the number of testing and application possibilities. Another excellent candidate for implementation within ONETEP are the Tkatechnko-Scheffler schemes [94, 96] which at present are the best performing functionals while being as efficient as the underlying DFT calculation. Both schemes use Hirshfeld partitioning for the density to calculate dispersion coefficients and add a correction to the ground state energy. A Hirshfeld partitioning scheme exists in the development stages in ONETEP, so implementation of the Tkatchenko-Scheffler methods would be fairly straightforward in the relatively near future. A possibility for future work in the area of molecular crystals could be to follow a Klimeš *et al.* [11] approach and attempt to find optimized exchange functionals specifically for molecular crystals by applying vdW-DFs to a wide range of these types of systems. Overall, the use of linear-scaling DFT with vdW is soon to become standard practice, offering countless possibilities of applications to realistic systems such as biological systems, molecular crystals for the pharmaceutical industry and organic/inorganic interfaces for photovoltaics.

Bibliography

[1] Pier Luigi Silvestrelli. Van der Waals Interactions in DFT made easy by Wannier Functions. *Physical Review Letters*, 100(5):053002, February 2008.

[2] Guillermo Román-Pérez and José M. Soler. Efficient Implementation of a van der Waals Density Functional: Application to Double-Wall Carbon Nanotubes. *Physical Review Letters*, 103(9):096102, 2009.

[3] O. Boiko and A. Verbitsky. Photovoltaic properties of C_{60}/liquid crystal composites and heterostructures. *Molecular Crystals and Liquid Crystals*, 384(1), 2002-01-01T00:00:00.

[4] Ajanta Haldar, Subhasis Maity, and N.B. Manik. Effect of C_{60} on methyl red and crystal violet dye-doped photovoltaic device. *Ionics*, 14(3):263–267, 2008.

[5] S. W. Tsang, H. Fu, R. Wang, J. Lu, K. Yu, and Y. Tao. Highly efficient cross-linked PbS nanocrystal/C_{60} hybrid heterojunction photovoltaic cells. *Applied Physics Letters*, 95(18):183505, 2009.

[6] Nicola Marzari and David Vanderbilt. Maximally localized generalized wannier functions for composite energy bands. *Physical Review B*, 56(20):12847, November 1997.

[7] Lampros Andrinopoulos, Nicholas D. M. Hine, and Arash A. Mostofi. Calculating dispersion interactions using maximally localized Wannier functions. *The Journal of Chemical Physics*, 135(15):154105, 2011.

[8] Chris-Kriton Skylaris, Peter D. Haynes, Arash A. Mostofi, and Mike C. Payne. Introducing ONETEP: linear-scaling density functional sim-

ulations on parallel computers. *The Journal of Chemical Physics*, 122(8):084119, 2005.

[9] M. Dion, H. Rydberg, E. Schröder, D. C. Langreth, and B. I. Lundqvist. Van der Waals density functional for general geometries. *Physical Review Letters*, 92(24):246401, June 2004.

[10] Kyuho Lee, Éamonn D. Murray, Lingzhu Kong, Bengt I. Lundqvist, and David C. Langreth. Higher-accuracy van der Waals density functional. *Physical Review B*, 82(8):081101, 2010.

[11] Jiří Klimeš, David R. Bowler, and Angelos Michaelides. Chemical accuracy for the van der Waals density functional. *Journal of Physics: Condensed Matter*, 22(2):022201, 2010.

[12] Heath J. R. O'Brien S. C. Curl R. F. Smalley R. E. Kroto, H. W. C_{60}: Buckminsterfullerene. *Nature*, 318:162, 1985.

[13] M. Born and R. Oppenheimer. Zur quantentheorie der molekeln. *Annalen der Physik*, 389(20):457–484, 1927.

[14] Jürgen Hafner, Christopher Wolverton, and Gerbrand Ceder. Toward computational materials design: The impact of density functional theory on materials research. *MRS Bulletin*, 31(9):659–668, 2006.

[15] P. Hohenberg and W. Kohn. Inhomogeneous electron gas. *Physical Review*, 136(3B):B864, November 1964.

[16] Jorge Kohanoff. *Electronic Structure Calculations for Solids and Molecules: Theory and Computational Methods*. Cambridge University Press, 2006.

[17] W. Kohn and L. J. Sham. Self-Consistent equations including exchange and correlation effects. *Physical Review*, 140(4A):A1133, November 1965.

[18] D. M. Ceperley and B. J. Alder. Ground state of the electron gas by a stochastic method. *Phys. Rev. Lett.*, 45:566–569, Aug 1980.

[19] Murray Gell-Mann and Keith A. Brueckner. Correlation energy of an electron gas at high density. *Phys. Rev.*, 106:364–368, Apr 1957.

[20] J. P. Perdew and Alex Zunger. Self-interaction correction to density-functional approximations for many-electron systems. *Phys. Rev. B*, 23:5048–5079, May 1981.

[21] R. O. Jones and O. Gunnarsson. The density functional formalism, its applications and prospects. *Reviews of Modern Physics*, 61(3):689, July 1989.

[22] John P. Perdew, Kieron Burke, and Matthias Ernzerhof. Generalized gradient approximation made simple. *Physical Review Letters*, 77(18):3865, October 1996.

[23] John P. Perdew, J. A. Chevary, S. H. Vosko, Koblar A. Jackson, Mark R. Pederson, D. J. Singh, and Carlos Fiolhais. Atoms, molecules, solids, and surfaces: Applications of the generalized gradient approximation for exchange and correlation. *Phys. Rev. B*, 46:6671–6687, Sep 1992.

[24] Chengteh Lee, Weitao Yang, and Robert G. Parr. Development of the colle-salvetti correlation-energy formula into a functional of the electron density. *Phys. Rev. B*, 37:785–789, Jan 1988.

[25] Zhigang Wu and R. E. Cohen. More accurate generalized gradient approximation for solids. *Phys. Rev. B*, 73:235116, Jun 2006.

[26] John P. Perdew, Adrienn Ruzsinszky, Gábor I. Csonka, Oleg A. Vydrov, Gustavo E. Scuseria, Lucian A. Constantin, Xiaolan Zhou, and Kieron Burke. Restoring the density-gradient expansion for exchange in solids and surfaces. *Phys. Rev. Lett.*, 100:136406, Apr 2008.

[27] John P. Perdew and Karla Schmidt. Jacob's ladder of density functional approximations for the exchange-correlation energy. *AIP Conference Proceedings*, 577(1):1–20, 2001.

[28] Felix Bloch. Über die quantenmechanik der elektronen in kristallgittern. *Zeitschrift für Physik*, 52(7-8):555–600, 1929.

[29] Charles Kittel. *Introduction to Solid State Physics*. Wiley & Sons, 8th edition, 2005.

[30] Hendrik J. Monkhorst and James D. Pack. Special points for brillouin-zone integrations. *Phys. Rev. B*, 13:5188–5192, Jun 1976.

[31] James C. Phillips. Energy-band interpolation scheme based on a pseudopotential. *Phys. Rev.*, 112:685–695, Nov 1958.

[32] D. R. Hamann, M. Schlüter, and C. Chiang. Norm-conserving pseudopotentials. *Phys. Rev. Lett.*, 43:1494–1497, Nov 1979.

[33] N. Troullier and José Luriaas Martins. Efficient pseudopotentials for plane-wave calculations. *Phys. Rev. B*, 43(3):1993–2006, Jan 1991.

[34] David Vanderbilt. Soft self-consistent pseudopotentials in a generalized eigenvalue formalism. *Phys. Rev. B*, 41:7892–7895, Apr 1990.

[35] P. E. Blöchl. Projector augmented-wave method. *Phys. Rev. B*, 50:17953–17979, Dec 1994.

[36] J. F. Dobson. *Fundamentals of Time-Dependent Density Functional Theory (Springer Lecture Notes in Physics, V. 837)*. Springer, 2012.

[37] A Tkatchenko, L Romaner, OT Hofmann, E Zojer, C Ambrosch-Draxl, and M Scheffler. Van der Waals interactions between organic adsorbates and at Organic/Inorganic interfaces. *MRS BULLETIN*, 35(6):435–442, June 2010.

[38] V.R. Cooper, L. Kong, and D.C. Langreth. Computing dispersion interactions in density functional theory. *Physics Procedia*, 3(3):1417–1430, February 2010.

[39] Jiří Klimeš and Angelos Michaelides. Perspective: Advances and challenges in treating van der Waals dispersion forces in density functional theory. *The Journal of Chemical Physics*, 137(12):120901, 2012.

[40] H.C. Hamaker. The london-van der Waals attraction between spherical particles. *Physica*, 4(10):1058.

[41] F. London. Zur theorie und systematik der molekularkräfte. *Zeitschrift für Physik*, 63(3-4):245–279, 1930.

[42] John F. Dobson, Keith McLennan, Angel Rubio, Jun Wang, Tim Gould, Hung M. Le, and Bradley P. Dinte. Prediction of dispersion forces: Is there a problem? *Aust. J. Chem.*, 54(8):513–527, January 2001.

[43] John F. Dobson and Tim Gould. *J. Phys.: Condens. Matter*, 24:073201, 2012.

[44] D. Langbein. *Theory of van der Waals Attraction (Springer Tracts in Modern Physics)*, volume 72. 1974.

[45] Ilya Kaplan. *Intermolecular Interactions: Physical Picture, Computational Methods, and Model Potentials*. Wiley & Sons, 2006.

[46] J. Mahanty and B. W. Ninham. *Dispersion Forces*. Academic Press, London-New York-San Francisco, 1976.

[47] J.O. Hirschfelder. Perturbation theory for exchange forces, i. *Chemical Physics Letters*, 1(8):325 – 329, 1967.

[48] Bogumil Jeziorski, Robert Moszynski, and Krzysztof Szalewicz. Perturbation theory approach to intermolecular potential energy surfaces of van der Waals complexes. *Chemical Reviews*, 94(7):1887–1930, 1994.

[49] Konrad Patkowski, Bogumil Jeziorski, and Krzysztof Szalewicz. Unified treatment of chemical and van der Waals forces via symmetry-adapted perturbation expansion. *The Journal of Chemical Physics*, 120(15):6849–6862, 2004.

[50] John C. Slater and John G. Kirkwood. The van der Waals forces in gases. *Phys. Rev.*, 37(6):682–697, Mar 1931.

[51] H. B. G. Casimir and D. Polder. The influence of retardation on the london-van der Waals forces. *Physical Review*, 73(4):360, February 1948.

[52] David C. Langreth and John P. Perdew. Exchange-correlation energy of a metallic surface: Wave-vector analysis. *Physical Review B*, 15(6):2884, March 1977.

[53] D. C. Langreth and J. P. Perdew. The exchange-correlation energy of a metallic surface. *Solid State Communications*, 17(11):1425–1429, December 1975.

[54] B. I. Lundqvist, Y. Andersson, H. Shao, S. Chan, and D. C. Langreth. Density functional theory including Van Der Waals forces. *International Journal of Quantum Chemistry*, 56(4):247–255, 1995.

[55] Walter Kohn, Yigal Meir, and Dmitrii E. Makarov. van der Waals energies in density functional theory. *Physical Review Letters*, 80(19):4153, May 1998.

[56] David Bohm and David Pines. A collective description of electron interactions: III. coulomb interactions in a degenerate electron gas. *Physical Review*, 92(3):609, November 1953.

[57] John F. Dobson and Jun Wang. Successful test of a seamless van der Waals density functional. *Physical Review Letters*, 82(10):2123, March 1999.

[58] Martin Fuchs and Xavier Gonze. Accurate density functionals: Approaches using the adiabatic-connection fluctuation-dissipation theorem. *Physical Review B*, 65(23):235109, June 2002.

[59] Huy-Viet Nguyen and Giulia Galli. A first-principles study of weakly bound molecules using exact exchange and the random phase approximation. *The Journal of Chemical Physics*, 132(4):044109, 2010.

[60] Alexandre Tkatchenko, Alberto Ambrosetti, and Jr. Robert A. DiStasio. Interatomic methods for the dispersion energy derived from the adiabatic connection fluctuation-dissipation theorem. *The Journal of Chemical Physics*, 138(7):074106, 2013.

[61] Judith Harl, Laurids Schimka, and Georg Kresse. Assessing the quality of the random phase approximation for lattice constants and atomization energies of solids. *Physical Review B*, 81(11):115126, March 2010.

[62] Henk Eshuis, JeffersonE. Bates, and Filipp Furche. Electron correlation methods based on the random phase approximation. *Theoretical Chemistry Accounts*, 131(1):1–18, 2012.

[63] N. S. Ostlund A. Szabo. *Modern Quantum Chemistry: Introduction to Advanced Electronic Structure Theory*. McGraw Hill: New York, 1989.

[64] Rodney J. Bartlett. Coupled-cluster approach to molecular structure and spectra: a step toward predictive quantum chemistry. *The Journal of Physical Chemistry*, 93(5):1697–1708, 1989.

[65] Chr. Møller and M. S. Plesset. Note on an approximation treatment for many-electron systems. *Phys. Rev.*, 46:618–622, Oct 1934.

[66] J. Řezáč, P. Jurečka, K. E. Riley, J. Černý, H. Valdes, K. Pluháčkovă, K. Berka, J. Řezáč, M. Pitoňák, J. Vondrášek, and P. Hobza. *Collect. Czech. Chem. Commun.*, 73:1261–1270, 2008.

[67] Young Choon Park and Jae Shin Lee. Accurate *ab initio* binding energies of the benzene dimer. *The Journal of Physical Chemistry A*, 110(15):5091–5095, 2006.

[68] Tomasz Janowski and Peter Pulay. High accuracy benchmark calculations on the benzene dimer potential energy surface. *Chemical Physics Letters*, 447(1-3):27 – 32, 2007.

[69] Petr Jurecka, Jiri Sponer, Jiri Cerny, and Pavel Hobza. Benchmark database of accurate (MP2 and CCSD(T) complete basis set limit) interaction energies of small model complexes, dna base pairs, and amino acid pairs. *Phys. Chem. Chem. Phys.*, 8:1985–1993, 2006.

[70] Alexandre Tkatchenko, Robert A. DiStasio, Martin Head-Gordon, and Matthias Scheffler. Dispersion-corrected Moller-Plesset second-order perturbation theory. *The Journal of Chemical Physics*, 131(9):094106, 2009. http://www.fhi-berlin.mpg.de/th/C6-MP2-REF-database.txt.

[71] Velegol Darrell Kim Hye-Young Lucas Amand A. Cole, Milton W. Nanoscale van der Waals interactions. *Molecular Simulation*, 35(10):849–866, 2009.

[72] Axel D. Becke and Erin R. Johnson. Exchange-hole dipole moment and the dispersion interaction. *The Journal of Chemical Physics*, 122(15):154104, 2005.

[73] Axel D. Becke and Erin R. Johnson. Exchange-hole dipole moment and the dispersion interaction revisited. *The Journal of Chemical Physics*, 127(15):154108, 2007.

[74] Erin R. Johnson and Axel D. Becke. A post-Hartree-Fock model of intermolecular interactions: Inclusion of higher-order corrections. *The Journal of Chemical Physics*, 124(17):174104, 2006.

[75] Stephan N. Steinmann and Clemence Corminboeuf. Comprehensive benchmarking of a density-dependent dispersion correction. *Journal of Chemical Theory and Computation*, 7(11):3567–3577, 2011.

[76] Miguel A. L. Marques, Alberto Castro, Giuliano Malloci, Giacomo Mulas, and Silvana Botti. Efficient calculation of van der Waals dispersion coefficients with time-dependent density functional theory in real time:

Application to polycyclic aromatic hydrocarbons. *The Journal of Chemical Physics*, 127(1):014107, 2007.

[77] Silvana Botti, Alberto Castro, Xavier Andrade, Angel Rubio, and Miguel A. L. Marques. Cluster-surface and cluster-cluster interactions: *Ab initio* calculations and modeling of asymptotic van der Waals forces. *Physical Review B*, 78(3):035333, July 2008.

[78] Micael J. T. Oliveira, Silvana Botti, and Miguel A. L. Marques. Modeling van der Waals interactions between proteins and inorganic surfaces from time-dependent density functional theory calculations. *Phys. Chem. Chem. Phys.*, 13:15055–15061, 2011.

[79] O. Anatole von Lilienfeld, Ivano Tavernelli, Ursula Rothlisberger, and Daniel Sebastiani. Optimization of effective atom centered potentials for london dispersion forces in density functional theory. *Phys. Rev. Lett.*, 93(15):153004, Oct 2004.

[80] I-Chun Lin, Maurício D. Coutinho-Neto, Camille Felsenheimer, O. Anatole von Lilienfeld, Ivano Tavernelli, and Ursula Rothlisberger. Library of dispersion-corrected atom-centered potentials for generalized gradient approximation functionals: Elements H, C, N, O, He, Ne, Ar, and Kr. *Phys. Rev. B*, 75(20):205131, May 2007.

[81] Enrico Tapavicza, I-Chun Lin, O. Anatole von Lilienfeld, Ivano Tavernelli, Maurício D. Coutinho-Neto, and Ursula Rothlisberger. Weakly bonded complexes of aliphatic and aromatic carbon compounds described with dispersion corrected density functional theory. *Journal of Chemical Theory and Computation*, 3(5):1673–1679, 2007.

[82] J. F. Dobson. Queen Mary vdW Masterclass. May 2013.

[83] Takeshi Sato, Takao Tsuneda, and Kimihiko Hirao. A density-functional study on π -aromatic interaction: Benzene dimer and naphthalene dimer. *The Journal of Chemical Physics*, 123(10):104307, 2005.

[84] S. Grimme. Semiempirical GGA-type density functional constructed with a long-range dispersion correction. *Journal of Computational Chemistry*, 27(15):1787–1799, 2006.

[85] Stefan Grimme. Semiempirical hybrid density functional with perturbative second-order correlation. *The Journal of Chemical Physics*, 124(3):034108, 2006.

[86] F. Ortmann, F. Bechstedt, and W. G. Schmidt. Semiempirical van der Waals correction to the density functional description of solids and molecular structures. *Phys. Rev. B*, 73(20):205101, May 2006.

[87] Stefan Grimme, Jens Antony, Stephan Ehrlich, and Helge Krieg. A consistent and accurate *ab initio* parametrization of density functional dispersion correction (DFT-D) for the 94 elements H-Pu. *The Journal of Chemical Physics*, 132(15):154104, 2010.

[88] Qin Wu and Weitao Yang. Empirical correction to density functional theory for van der Waals interactions. *The Journal of Chemical Physics*, 116(2):515, 2002.

[89] Quintin Hill and Chris-Kriton Skylaris. Including dispersion interactions in the ONETEP program for linear-scaling density functional theory calculations. *Proceedings of the Royal Society A: Mathematical, Physical and Engineering Science*, 465(2103):669 –683, March 2009.

[90] Y. Andersson, D. C. Langreth, and B. I. Lundqvist. van der Waals interactions in Density-Functional theory. *Physical Review Letters*, 76(1):102, January 1996.

[91] A. C. Maggs and N. W. Ashcroft. Electronic fluctuation and cohesion in metals. *Physical Review Letters*, 59(1):113, July 1987.

[92] K. Rapcewicz and N. W. Ashcroft. Fluctuation attraction in condensed matter: A nonlocal functional approach. *Physical Review B*, 44(8):4032, 1991.

[93] Pier Luigi Silvestrelli. van der Waals interactions in density functional theory using Wannier functions. *The Journal of Physical Chemistry A*, 113(17):5224–5234, April 2009.

[94] Alexandre Tkatchenko and Matthias Scheffler. Accurate molecular van der Waals interactions from Ground-State electron density and Free-Atom reference data. *Physical Review Letters*, 102(7):073005, February 2009.

[95] F.L. Hirshfeld. Bonded-atom fragments for describing molecular charge densities. *Theoretica chimica acta*, 44(2):129–138, 1977.

[96] Alexandre Tkatchenko, Robert A. DiStasio, Roberto Car, and Matthias Scheffler. Accurate and efficient method for many-body van der Waals interactions. *Phys. Rev. Lett.*, 108:236402, Jun 2012.

[97] Hye-Young Kim, Jorge O. Sofo, Darrell Velegol, Milton W. Cole, and Amand A. Lucas. van der Waals forces between nanoclusters: Importance of many-body effects. *The Journal of Chemical Physics*, 124(7):074504, 2006.

[98] Bengt I. Lundqvist, Erika Hult, Henrik Rydberg, Alexander Bogicevic, Johan Strömquist, and David C. Langreth. Density functionals and van der Waals interactions at surfaces. *Progress in Surface Science*, 59(1-4):149–165, September.

[99] Erika Hult, Ylva Andersson, Bengt I. Lundqvist, and David C. Langreth. Density functional for van der Waals forces at surfaces. *Physical Review Letters*, 77(10):2029, 1996.

[100] Y. Andersson, E. Hult, P. Apell, D. C. Langreth, and B. I. Lundqvist. Density-functional account of van der Waals forces between parallel surfaces. *Solid State Communications*, 106(5):235–238, May 1998.

[101] Henrik Rydberg, Bengt I. Lundqvist, David C. Langreth, and Maxime Dion. Tractable nonlocal correlation density functionals for flat surfaces and slabs. *Physical Review B*, 62(11):6997, 2000.

[102] David C. Langreth and M. J. Mehl. Easily implementable nonlocal Exchange-Correlation energy functional. *Physical Review Letters*, 47(6):446, 1981.

[103] D. C. Langreth, M. Dion, H. Rydberg, E. Schröder, P. Hyldgaard, and B. I. Lundqvist. Van der Waals density functional theory with applications. *International Journal of Quantum Chemistry*, 101(5):599–610, 2005.

[104] H. Rydberg, M. Dion, N. Jacobson, E. Schröder, P. Hyldgaard, S. I. Simak, D. C. Langreth, and B. I. Lundqvist. Van der Waals density functional for layered structures. *Physical Review Letters*, 91(12):126402, 2003.

[105] T. Thonhauser, Valentino R. Cooper, Shen Li, Aaron Puzder, Per Hyldgaard, and David C. Langreth. Van der Waals density functional: Self-consistent potential and the nature of the van der Waals bond. *Physical Review B*, 76(12):125112, 2007.

[106] Yingkai Zhang and Weitao Yang. Comment on "Generalized Gradient Approximation Made Simple". *Phys. Rev. Lett.*, 80(4):890, Jan 1998.

[107] Valentino R. Cooper. Van der Waals density functional: An appropriate exchange functional. *Phys. Rev. B*, 81:161104, Apr 2010.

[108] John P. Perdew and Wang Yue. Accurate and simple density functional for the electronic exchange energy: Generalized gradient approximation. *Phys. Rev. B*, 33:8800–8802, Jun 1986.

[109] Éamonn D. Murray, Kyuho Lee, and David C. Langreth. Investigation of exchange energy density functional accuracy for interacting molecules. *Journal of Chemical Theory and Computation*, 5(10):2754–2762, 2009.

[110] Ikutaro Hamada and Susumu Yanagisawa. Pseudopotential approximation in van der Waals density functional calculations. *Phys. Rev. B*, 84:153104, Oct 2011.

[111] Oleg A. Vydrov and Troy Van Voorhis. Nonlocal van der Waals density functional made simple. *Physical Review Letters*, 103(6):063004, 2009.

[112] Oleg A. Vydrov and Troy Van Voorhis. Improving the accuracy of the nonlocal van der Waals density functional with minimal empiricism. *The Journal of Chemical Physics*, 130(10):104105, 2009.

[113] Oleg A. Vydrov and Troy Van Voorhis. Dispersion interactions from a local polarizability model. *Physical Review A*, 81(6):062708, June 2010.

[114] Oleg A. Vydrov and Troy Van Voorhis. *Fundamentals of Time-Dependent Density Functional Theory (Springer Lecture Notes in Physics, V. 837)*. Springer, 2012.

[115] Oleg A. Vydrov and Troy Van Voorhis. Nonlocal van der Waals density functional: The simpler the better. *The Journal of Chemical Physics*, 133(24):244103, 2010.

[116] Riccardo Sabatini, Tommaso Gorni, and Stefano de Gironcoli. Nonlocal van der Waals density functional made simple and efficient. *Phys. Rev. B*, 87:041108, Jan 2013.

[117] Oleg A. Vydrov and Troy Van Voorhis. Benchmark assessment of the accuracy of several van der Waals density functionals. *Journal of Chemical Theory and Computation*, 8(6):1929–1934, 2012.

[118] Gregory H. Wannier. The structure of electronic excitation levels in insulating crystals. *Phys. Rev.*, 52(3):191–197, Aug 1937.

[119] K. S. Thygesen, L. B. Hansen, and K. W. Jacobsen. Partly occupied wannier functions. *Phys. Rev. Lett.*, 94(2):026405, Jan 2005.

[120] K. S. Thygesen, L. B. Hansen, and K. W. Jacobsen. Partly occupied wannier functions: Construction and applications. *Phys. Rev. B*, 72(12):125119, Sep 2005.

[121] Ivo Souza, Nicola Marzari, and David Vanderbilt. Maximally localized wannier functions for entangled energy bands. *Physical Review B*, 65(3):035109, December 2001.

[122] Arash A. Mostofi, Jonathan R. Yates, Young-Su Lee, Ivo Souza, David Vanderbilt, and Nicola Marzari. wannier90: A tool for obtaining maximally-localised wannier functions. *Computer Physics Communications*, 178(9):685–699, May 2008.

[123] Stefan Grimme, Jens Antony, Tobias Schwabe, and Christian Mück-Lichtenfeld. Density functional theory with dispersion corrections for supramolecular structures, aggregates, and complexes of (bio)organic molecules. *Organic & Biomolecular Chemistry*, 5(5):741–758, March 2007. PMID: 17315059.

[124] X. Wu, M. C. Vargas, S. Nayak, V. Lotrich, and G. Scoles. Towards extending the applicability of density functional theory to weakly bound systems. *The Journal of Chemical Physics*, 115(19):8748–8757, 2001.

[125] Pier Luigi Silvestrelli, Karima Benyahia, Sonja Grubisiĉ, Francesco Ancilotto, and Flavio Toigo. Van der Waals interactions at surfaces by density functional theory using Wannier functions. *The Journal of Chemical Physics*, 130(7):074702, 2009.

[126] Pier Luigi Silvestrelli. Improvement in hydrogen bond description using van der Waals-corrected DFT: The case of small water clusters. *Chemical Physics Letters*, 475(4-6):285 – 288, 2009.

[127] A. Ambrosetti and P. L. Silvestrelli. Adsorption of rare-gas atoms and water on graphite and graphene by van der Waals-corrected density functional theory. *The Journal of Physical Chemistry C*, 115(9):3695–3702, 2011.

[128] A. Ambrosetti and P. L. Silvestrelli. van der Waals interactions in density functional theory using wannier functions: Improved C_6 and C_3 coefficients by a different approach. *Phys. Rev. B*, 85:073101, Feb 2012.

[129] Pier Luigi Silvestrelli and Alberto Ambrosetti. Inclusion of screening effects in the van der Waals corrected DFT simulation of adsorption processes on metal surfaces. *Phys. Rev. B*, 87:075401, Feb 2013.

[130] Pier Luigi Silvestrelli. Van der Waals interactions in density functional theory by combining the quantum harmonic oscillator-model with localized Wannier functions. *The Journal of Chemical Physics*, 139(5):054106, 2013.

[131] Matthew Shelley, Nicolas Poilvert, Arash A. Mostofi, and Nicola Marzari. Automated quantum conductance calculations using maximally-localised wannier functions. *Computer Physics Communications*, 182(10):2174 – 2183, 2011.

[132] Paolo Giannozzi, Stefano Baroni, Nicola Bonini, Matteo Calandra, Roberto Car, Carlo Cavazzoni, Davide Ceresoli, Guido L Chiarotti, Matteo Cococcioni, Ismaila Dabo, Andrea Dal Corso, Stefano de Gironcoli, Stefano Fabris, Guido Fratesi, Ralph Gebauer, Uwe Gerstmann, Christos Gougoussis, Anton Kokalj, Michele Lazzeri, Layla Martin-Samos, Nicola Marzari, Francesco Mauri, Riccardo Mazzarello, Stefano Paolini, Alfredo Pasquarello, Lorenzo Paulatto, Carlo Sbraccia, Sandro Scandolo, Gabriele Sclauzero, Ari P Seitsonen, Alexander Smogunov, Paolo Umari, and Renata M Wentzcovitch. QUANTUM ESPRESSO: a modular and open-source software project for quantum simulations of materials. *Journal of Physics: Condensed Matter*, 21(39):395502, 2009.

[133] Vincenzo Barone, Maurizio Casarin, Daniel Forrer, Michele Pavone, Mauro Sambi, and Andrea Vittadini. Role and effective treatment of

dispersive forces in materials: Polyethylene and graphite crystals as test cases. *Journal of Computational Chemistry*, 30(6):934–939, 2009.

[134] M. Dion, H. Rydberg, E. Schröder, D. C. Langreth, and B. I. Lundqvist. Erratum: Van der Waals density functional for general geometries [phys. rev. lett. 92, 246401 (2004)]. *Phys. Rev. Lett.*, 95(10):109902, Sep 2005.

[135] Svetla D. Chakarova-Käck, Elsebeth Schröder, Bengt I. Lundqvist, and David C. Langreth. Application of van der Waals density functional to an extended system: Adsorption of benzene and naphthalene on graphite. *Phys. Rev. Lett.*, 96(14):146107, Apr 2006.

[136] Petr Slavíček, René Kalus, Petr Paška, Iva Odvárková, Pavel Hobza, and Anatol Malijevský. State-of-the-art correlated *ab initio* potential energy curves for heavy rare gas dimers: Ar_2, Kr_2, and Xe_2. *The Journal of Chemical Physics*, 119(4):2102–2119, 2003.

[137] E. Orti and J. L. Bredas. Electronic structure of metal-free phthalocyanine: A valence effective hamiltonian theoretical study. *The Journal of Chemical Physics*, 89(2):1009–1016, 1988.

[138] Shoji Ishibashi, Norio Terada, Madoka Tokumoto, Nobumori Kinoshita, and Hideo Ihara. Characterization of fullerenes using positrons. *Hyperfine Interactions*, 84(1):413–419, 1994.

[139] Noa Marom, Alexandre Tkatchenko, Matthias Scheffler, and Leeor Kronik. Describing both dispersion interactions and electronic structure using density functional theory: The case of metal-phthalocyanine dimers. *Journal of Chemical Theory and Computation*, 6(1):81–90, January 2010.

[140] Anton Kokalj. Computer graphics and graphical user interfaces as tools in simulations of matter at the atomic scale. *Computational Materials Science*, 28(2):155 – 168, 2003. Proceedings of the Symposium on Software Development for Process and Materials Design.

[141] Marcus Elstner, Pavel Hobza, Thomas Frauenheim, Sándor Suhai, and Efthimios Kaxiras. Hydrogen bonding and stacking interactions of nucleic acid base pairs: A density-functional-theory based treatment. *The Journal of Chemical Physics*, 114(12):5149, 2001.

[142] Mooij, Frans B. van Duijneveldt, Jeanne G. C. M. van Duijneveldt-van de Rijdt, and Bouke P. van Eijck. Transferable *ab initio* intermolecular potentials. 1. derivation from methanol dimer and trimer calculations. *The Journal of Physical Chemistry A*, 103(48):9872–9882, 1999.

[143] S J Clark, M D Segall, C J Pickard, P J Hasnip, M J Probert, K Refson, and M C Payne. First principles methods using castep. *Zeitschrift für Kristallographie*, 220(5-6):567–570, 2005. Reproduced with permission from the publisher.

[144] X. Gonze, B. Amadon, P.-M. Anglade, J.-M. Beuken, F. Bottin, P. Boulanger, F. Bruneval, D. Caliste, R. Caracas, M. Côté, T. Deutsch, L. Genovese, Ph. Ghosez, M. Giantomassi, S. Goedecker, D.R. Hamann, P. Hermet, F. Jollet, G. Jomard, S. Leroux, M. Mancini, S. Mazevet, M.J.T. Oliveira, G. Onida, Y. Pouillon, T. Rangel, G.-M. Rignanese, D. Sangalli, R. Shaltaf, M. Torrent, M.J. Verstraete, G. Zerah, and J.W. Zwanziger. Abinit: First-principles approach to material and nanosystem properties. *Computer Physics Communications*, 180(12):2582 – 2615, 2009.

[145] Giulia Galli. Linear scaling methods for electronic structure calculations and quantum molecular dynamics simulations. *Current Opinion in Solid State and Materials Science*, 1(6):864 – 874, 1996.

[146] Stefan Goedecker. Linear scaling electronic structure methods. *Rev. Mod. Phys.*, 71:1085–1123, Jul 1999.

[147] D R Bowler and T Miyazaki. $\mathcal{O}(N)$ methods in electronic structure calculations. *Reports on Progress in Physics*, 75(3):036503, 2012.

[148] W. Kohn. Density functional and density matrix method scaling linearly with the number of atoms. *Phys. Rev. Lett.*, 76:3168–3171, Apr 1996.

[149] W. Kohn. Analytic properties of bloch waves and wannier functions. *Phys. Rev.*, 115:809–821, Aug 1959.

[150] Jacques Des Cloizeaux. Analytical properties of n-dimensional energy bands and wannier functions. *Phys. Rev.*, 135:A698–A707, Aug 1964.

[151] Nicola Marzari, Arash A. Mostofi, Jonathan R. Yates, Ivo Souza, and David Vanderbilt. Maximally localized wannier functions: Theory and applications. *Rev. Mod. Phys.*, 84:1419–1475, Oct 2012.

[152] José M. Soler, Emilio Artacho, Julian D Gale, Alberto García, Javier Junquera, Pablo Ordejón, and Daniel Sánchez-Portal. The siesta method for *ab initio* order-N materials simulation. *Journal of Physics: Condensed Matter*, 14(11):2745, 2002.

[153] D. R. Bowler, R. Choudhury, M. J. Gillan, and T. Miyazaki. Recent progress with large-scale *ab initio* calculations: the CONQUEST code. *Physica Status Solidi (b)*, 243(5):989–1000, 2006.

[154] J.-L. Fattebert and J. Bernholc. Towards grid-based $O(N)$ density-functional theory methods: Optimized nonorthogonal orbitals and multigrid acceleration. *Phys. Rev. B*, 62:1713–1722, Jul 2000.

[155] J.-L. Fattebert and F. Gygi. Linear-scaling first-principles molecular dynamics with plane-waves accuracy. *Phys. Rev. B*, 73:115124, Mar 2006.

[156] T. Ozaki and H. Kino. Efficient projector expansion for the *ab initio* LCAO method. *Phys. Rev. B*, 72:045121, Jul 2005.

[157] Joost VandeVondele, Matthias Krack, Fawzi Mohamed, Michele Parrinello, Thomas Chassaing, and Jürg Hutter. Quickstep: Fast and accurate density functional calculations using a mixed gaussian and plane waves approach. *Computer Physics Communications*, 167(2):103 – 128, 2005.

[158] Gregory Ho Emily A. Carter Jeng-Da Chai, Vincent L. Lignères and John D. Weeks. Orbital-free density functional theory: Linear scaling methods for kinetic potentials, and applications to solid Al and Si. *Chemical Physics Letters*, 473(4):263–267, 2009.

[159] Michael Foley and Paul A. Madden. Further orbital-free kinetic-energy functionals for *ab initio* molecular dynamics. *Phys. Rev. B*, 53:10589–10598, Apr 1996.

[160] Chris-Kriton Skylaris, Peter D Haynes, Arash A Mostofi, and Mike C Payne. Using ONETEP for accurate and efficient $\mathcal{O}(N)$ density functional calculations. *Journal of Physics: Condensed Matter*, 17(37):5757, 2005.

[161] A. A. Mostofi P. D. Haynes, C.-K. Skylaris and M. C. Payne. ONETEP: linear-scaling density-functional theory with plane waves. *Psi-k Newsletter*, (72):78–91, 2005.

[162] Chris-Kriton Skylaris, Arash A. Mostofi, Peter D. Haynes, Oswaldo Diéguez, and Mike C. Payne. Nonorthogonal generalized wannier function pseudopotential plane-wave method. *Phys. Rev. B*, 66:035119, Jul 2002.

[163] Arash A. Mostofi, Peter D. Haynes, Chris-Kriton Skylaris, and Mike C. Payne. Preconditioned iterative minimization for linear-scaling electronic structure calculations. *The Journal of Chemical Physics*, 119(17):8842–8848, 2003.

[164] P D Haynes, C-K Skylaris, A A Mostofi, and M C Payne. Density kernel optimization in the onetep code. *Journal of Physics: Condensed Matter*, 20(29):294207, 2008.

[165] X.-P. Li, R. W. Nunes, and David Vanderbilt. Density-matrix electronic-structure method with linear system-size scaling. *Phys. Rev. B*, 47:10891–10894, Apr 1993.

[166] R. McWeeny. Some recent advances in density matrix theory. *Rev. Mod. Phys.*, 32:335–369, Apr 1960.

[167] R. W. Nunes and David Vanderbilt. Generalization of the density-matrix method to a nonorthogonal basis. *Phys. Rev. B*, 50:17611–17614, Dec 1994.

[168] P D Haynes, C-K Skylaris, A A Mostofi, and M C Payne. Density kernel optimization in the ONETEP code. *Journal of Physics: Condensed Matter*, 20(29):294207, 2008.

[169] Chris-Kriton Skylaris, Arash A. Mostofi, Peter D. Haynes, Chris J. Pickard, and Mike C. Payne. Accurate kinetic energy evaluation in electronic structure calculations with localized functions on real space grids. *Computer Physics Communications*, 140(3):315 – 322, 2001.

[170] N.D.M. Hine, P.D. Haynes, A.A. Mostofi, C.-K. Skylaris, and M.C. Payne. Linear-scaling density-functional theory with tens of thousands of atoms: Expanding the scope and scale of calculations with ONETEP. *Computer Physics Communications*, 180(7):1041 – 1053, 2009.

[171] Nicholas Zonias, Pavlos Lagoudakis, and Chris-Kriton Skylaris. Large-scale first principles and tight-binding density functional theory calcula-

tions on hydrogen-passivated silicon nanorods. *Journal of Physics: Condensed Matter*, 22(2):025303, 2010.

[172] Fabiano Corsetti and Arash A. Mostofi. System-size convergence of point defect properties: The case of the silicon vacancy. *Phys. Rev. B*, 84:035209, Jul 2011.

[173] Jacek Dziedzic, Stephen J. Fox, Thomas Fox, Christofer S. Tautermann, and Chris-Kriton Skylaris. Large-scale DFT calculations in implicit solvent - A case study on the T4 lysozyme L99A/M102Q protein. *International Journal of Quantum Chemistry*, 113(6):771–785, 2013.

[174] Louis P. Lee, Daniel J. Cole, Chris-Kriton Skylaris, William L. Jorgensen, and Mike C. Payne. Polarized protein-specific charges from atoms-in-molecule electron density partitioning. *Journal of Chemical Theory and Computation*, 9(7):2981–2991, 2013.

[175] Stephen J. Fox, Chris Pittock, Thomas Fox, Christofer S. Tautermann, Noj Malcolm, and Chris-Kriton Skylaris. Electrostatic embedding in large-scale first principles quantum mechanical calculations on biomolecules. *The Journal of Chemical Physics*, 135(22):224107, 2011.

[176] John P. Perdew and Yue Wang. Accurate and simple analytic representation of the electron-gas correlation energy. *Phys. Rev. B*, 45:13244–13249, Jun 1992.

[177] J. A. White and D. M. Bird. *Physical Review B*, 50:4954–4957.

[178] Jiří Klimeš, David R. Bowler, and Angelos Michaelides. Van der Waals density functionals applied to solids. *Phys. Rev. B*, 83:195131, May 2011.

[179] John P. Perdew, Kieron Burke, and Matthias Ernzerhof. Generalized gradient approximation made simple [Phys. rev. lett. 77, 3865 (1996)]. *Physical Review Letters*, 78(7):1396, February 1997.

[180] B. Hammer, L. B. Hansen, and J. K. Nørskov. Improved adsorption energetics within density-functional theory using revised Perdew-Burke-Ernzerhof functionals. *Phys. Rev. B*, 59(11):7413–7421, Mar 1999.

[181] A. D. Becke. Density-functional exchange-energy approximation with correct asymptotic behavior. *Phys. Rev. A*, 38:3098–3100, Sep 1988.

[182] A. D. Becke. On the large-gradient behavior of the density functional exchange energy. *The Journal of Chemical Physics*, 85(12):7184–7187, 1986.

[183] Judy C. Matthewman Kosmas Prassides T. John S. Dennis Jonathan P. Hare Harold W. Kroto Roger Taylor William I. F. David, Richard M. Ibberson and David R. M. Walton. Crystal structure and bonding of ordered C_{60}. *Nature*, 353:147–149, 1991.

[184] R. M. Fleming, T. Siegrist, P. M. Marsh, B. Hessen, A. R. Kortan, D. W. Murphy, R. C. Haddon, R. Tycko, G. Dabbagh, A. M. Mujsce, M. L. Kaplan, and S. M. Zahurak. Diffraction symmetry in crystalline, close-packed C_{60}. *Mat. Res. Soc. Symp. Proc.*, 206, 1991.

[185] John E. Fischer, Paul A. Heiney, Andrew R. McGhie, William J. Romanow, Arnold M. Denenstein, John P. McCauley, and Amos B. Smith. Compressibility of solid C_{60}. *Science*, 252(5010):1288–1290, 1991.

[186] Paul A. Heiney, John E. Fischer, Andrew R. McGhie, William J. Romanow, Arnold M. Denenstein, John P. McCauley Jr., Amos B. Smith, and David E. Cox. Orientational ordering transition in solid C_{60}. *Phys. Rev. Lett.*, 66:2911–2914, Jun 1991.

[187] Ravi Sachidanandam and A. B. Harris. Comment on "orientational ordering transition in solid C_{60}". *Phys. Rev. Lett.*, 67:1467–1467, Sep 1991.

[188] C. Pan, M. P. Sampson, Y. Chai, R. H. Hauge, and J. L. Margrave. Heats of sublimation from a polycrystalline mixture of carbon clusters (C_{60} and C_{70}). *The Journal of Physical Chemistry*, 95(8):2944–2946, 1991.

[189] Eric L. Shirley and Steven G. Louie. Electron excitations in solid c_{60}: Energy gap, band dispersions, and effects of orientational disorder. *Phys. Rev. Lett.*, 71:133–136, Jul 1993.

[190] Q.-M. Zhang, Jae-Yel Yi, and J. Bernholc. Structure and dynamics of solid C_{60}. *Phys. Rev. Lett.*, 66:2633–2636, May 1991.

[191] Susumu Saito and Atsushi Oshiyama. Cohesive mechanism and energy bands of solid c_{60}. *Phys. Rev. Lett.*, 66:2637–2640, May 1991.

[192] J. Abrefah, D. R. Olander, M. Balooch, and W. J. Siekhaus. Vapor pressure of buckminsterfullerene. *Applied Physics Letters*, 60(11):1313–1314, 1992.

[193] N. Troullier and José Luís Martins. Structural and electronic properties of C_{60}. *Phys. Rev. B*, 46:1754–1765, Jul 1992.

[194] Wanda Andreoni. Computational approach to the physical chemistry of fullerenes and their derivatives. *Annual Review of Physical Chemistry*, 49(1):405–439, 1998. PMID: 15012433.

[195] Gustavo E. Scuseria. *Ab initio* theoretical predictions of the equilibrium geometries of C_{60}, $C_{60}H_{60}$ and $C_{60}F_{60}$. *Chemical Physics Letters*, 176(5):423 – 427, 1991.

[196] Florent Tournus, Jean-Christophe Charlier, and Patrice Melinon. Mutual orientation of two C_{60} molecules: An *ab initio* study. *The Journal of Chemical Physics*, 122(9):094315, 2005.

[197] James S. Chickos and Jr. William E. Acree. Enthalpies of sublimation of organic and organometallic compounds. 1910–2001. *Journal of Physical and Chemical Reference Data*, 31(2):537–698, 2002.

[198] Kristian Berland, Øyvind Borck, and Per Hyldgaard. Van der Waals density functional calculations of binding in molecular crystals. *Computer Physics Communications*, 182(9):1800–1804, September 2011.

[199] J.D. Axe, P.C. Chow, S.C. Moss, and P. Wochner. Orientational disorder and the intermolecular potential of FCC C_{60}. *Physica B: Condensed Matter*, 219&220(0):121–124, 1996.

[200] W. V. Steele, R. D. Chirico, N. K. Smith, W. E. Billups, P. R. Elmore, and A. E. Wheeler. Standard enthalpy of formation of buckminsterfullerene. *The Journal of Physical Chemistry*, 96(12):4731–4733, 1992.

[201] Herminio P. Diogo, Manuel E. Minas da Piedade, T. John S. Dennis, Jonathan P. Hare, Harold W. Kroto, Roger Taylor, and David R. M. Walton. Enthalpies of formation of buckminsterfullerene (C_{60}) and of the parent ions C_{60}, C_{60}^{2+}, C_{60}^{3+} and C_{60}^{-}. *J. Chem. Soc., Faraday Trans.*, 89:3541–3544, 1993.

[202] C. K. Mathews, M. Sai Baba, T. S. Lakshmi Narasimhan, R. Balasubramanian, N. Sivaraman, T. G. Srinivasan, and P. R. Vasudeva Rao. Vaporization studies on buckminsterfullerene. *The Journal of Physical Chemistry*, 96(9):3566–3568, 1992.

Appendix A

Inverse of overlap matrix

Using the linear transformation from the Bloch states to the localized NGWFs

$$|\psi_n\rangle = M^{\alpha}_{\ n}|\phi_\alpha\rangle \tag{A.1}$$

we can write the inverse relationship and then expand once more for the Bloch states, to write:

$$\begin{aligned} |\phi_\alpha\rangle &= \sum_n (M^{-1})_{\alpha n}|\psi_n\rangle \\ &= \sum_n (M^{-1})_{\alpha n} M^{\beta}_{\ n}|\phi_\beta\rangle \end{aligned} \tag{A.2}$$

so

$$\sum_n (M^{-1})_{\alpha n} M^{\beta}_{\ n} = \delta^{\alpha}_{\ \beta} \tag{A.3}$$

Now multiplying both sides of Eq. A.3 by $S_{\beta\gamma}M^{*\gamma}_{\ m}$:

$$\begin{aligned} \sum_n (M^{-1})_{\alpha n} M^{\beta}_{\ n} S_{\beta\gamma} M^{*\gamma}_{\ m} &= S_{\alpha\gamma} M^{*\gamma}_{\ m} \\ &= \sum_n (M^{-1})_{\alpha n}\delta_{nm} = S_{\alpha\gamma} M^{*\gamma}_{\ m} \end{aligned} \tag{A.4}$$

so

$$(M^{-1})_{\alpha m} = S_{\alpha\gamma} M^{*\gamma}_{\ m}. \tag{A.5}$$

Now that we have an expression of $\mathbf{M}^{-1}$ explicitly in terms of known quantities, we use Eq. A.2 again to write:

$$|\phi_\alpha\rangle = \sum_n S_{\alpha\gamma} M^{*\gamma}_{\ n} |\psi_n\rangle \tag{A.6}$$

Now operating with $\langle\phi_\beta|$ on the left of Eq. A.6, recalling that $\langle\phi_\beta|\phi_\alpha\rangle = S_{\beta\alpha}$ and expanding on the right with respect to Bloch functions:

$$S_{\beta\alpha} = \sum_{nm} S_{\beta\delta} M^{\delta}_{\ m} S_{\alpha\gamma} M^{*\gamma}_{\ n} \delta_{mn} \tag{A.7}$$

Now, multiplying both sides by $S^{\beta\epsilon} S^{\alpha\eta}$, we get

$$S_{\beta\alpha} S^{\beta\epsilon} S^{\alpha\eta} = \sum_n S^{\beta\epsilon} S^{\alpha\eta} S_{\beta\delta} S_{\alpha\gamma} M^{\delta}_{\ m} M^{*\gamma}_{\ n}, \tag{A.8}$$

which now, using $S_{\alpha\beta} S^{\beta\gamma} = \delta^\gamma_\alpha$, becomes an explicit expression for $S^{\alpha\beta}$ in terms of the transformation matrices $\mathbf{M}$:

$$S^{\eta\epsilon} = \sum_n M^{*\eta}_{\ n} M^{\epsilon}_{\ n}. \tag{A.9}$$

Appendix B

vdW-DF non-local correlation energy integral in reciprocal space

Here we show how the non-local correlation double integral in real space can be written as a single integral of their Fourier components in reciprocal space. Expanding the θ functions as a Fourier series we get

$$\begin{aligned} E_{\mathrm{c}}^{\mathrm{nl}} &= \frac{1}{2}\int\int d\mathbf{r}d\mathbf{r}'\theta_\alpha(\mathbf{r})\theta_\beta(\mathbf{r}')\phi_{\alpha\beta}(r) \\ &= \frac{1}{2}\int\int d\mathbf{r}d\mathbf{r}'\sum_{\mathbf{G},\mathbf{G}'}\theta_\alpha(\mathbf{G})\theta_\beta(\mathbf{G}')e^{i(\mathbf{G}\cdot\mathbf{r}+\mathbf{G}'\cdot\mathbf{r}')}\phi_{\alpha\beta}(r). \end{aligned}$$

We can now define transformed coordinates as

$$\mathbf{R} = \mathbf{r} - \mathbf{r}'; \quad \mathbf{R}' = \mathbf{r} + \mathbf{r}' \tag{B.1}$$

or

$$\mathbf{r} = \frac{1}{2}(\mathbf{R} + \mathbf{R}'); \quad \mathbf{r}' = \frac{1}{2}(\mathbf{R}' - \mathbf{R}).$$

Note that now $r = |\mathbf{r} - \mathbf{r}'| = |\mathbf{R}|$. Using Eq. B.1 we can write

$$\mathbf{G}\cdot\mathbf{r} + \mathbf{G}'\cdot\mathbf{r}' = \frac{1}{2}\Big((\mathbf{G} - \mathbf{G}')\cdot\mathbf{R} + (\mathbf{G} + \mathbf{G}')\cdot\mathbf{R}'\Big).$$

Now defining

$$\mathbf{k} = \frac{1}{2}(\mathbf{G} - \mathbf{G}'); \quad \mathbf{k}' = \frac{1}{2}(\mathbf{G} + \mathbf{G}') \tag{B.2}$$

we can write

$$\begin{aligned} E_{\mathrm{c}}^{\mathrm{nl}} &= \frac{1}{2}\int\int d\mathbf{R}d\mathbf{R}' \sum_{\mathbf{G},\mathbf{G}'} \theta_\alpha(\mathbf{G})\theta_\beta(\mathbf{G}')e^{i\mathbf{k}\cdot\mathbf{R}}e^{i\mathbf{k}'\cdot\mathbf{R}'}\phi_\alpha\beta(|\mathbf{R}|) \\ &= \frac{1}{2}\sum_{\mathbf{G},\mathbf{G}'} \theta_\alpha(\mathbf{G})\theta_\beta(\mathbf{G}')\int e^{i\mathbf{k}'\cdot\mathbf{R}'}d\mathbf{R}'\int d\mathbf{R}e^{i\mathbf{k}\cdot\mathbf{R}}\phi_{\alpha\beta}(|\mathbf{R}|). \end{aligned}$$

Now, because $\int e^{i\mathbf{k}'\cdot\mathbf{R}'}d\mathbf{R}' = \int e^{i(\mathbf{G}+\mathbf{G}')\cdot\mathbf{R}'}d\mathbf{R}' = \delta_{\mathbf{G},-\mathbf{G}'}$ and $\theta_\alpha^*(\mathbf{G}) = \theta_\alpha(-\mathbf{G})$, the integral becomes

$$\begin{aligned} &\frac{1}{2}\sum_{\mathbf{G}'} \theta_\alpha(-\mathbf{G}')\theta_\beta(\mathbf{G}')\int d\mathbf{R}e^{-i\mathbf{G}'\cdot\mathbf{R}}\phi_{\alpha\beta}(|\mathbf{R}|) \\ &= \frac{1}{2}\int d\mathbf{k}\theta_\alpha^*(\mathbf{k})\theta_\beta(\mathbf{k})\phi_{\alpha\beta}(k) \end{aligned} \tag{B.3}$$

where in the last line the Fourier series was made into a continuous Fourier transform and we replaced the dummy index $\mathbf{G}'$ by $\mathbf{k}$.

Appendix C

Becke 88 exchange

The expression for the B88 exchange energy [181] is:

$$E_{\mathrm{x}} = E_{\mathrm{x}}^{\mathrm{LDA}} - \beta \sum_{\sigma} \int \rho_{\sigma}^{4/3} \frac{x_{\sigma}^{2}}{1 + \gamma\beta x_{\sigma} \mathrm{arcsinh}(x_{\sigma})} d\mathbf{r} \tag{C.1}$$

with $x_{\sigma} = \frac{|\nabla\rho_{\sigma}|}{\rho_{\sigma}^{4/3}}$, σ is the spin index and $\beta = 0.0042$ and $\gamma = 6$. The LDA exchange energy is:

$$E_{\mathrm{x}}^{\mathrm{LDA}} = -C_{x} \sum_{\sigma} \int \rho_{\sigma}^{4/3} d\mathbf{r} \tag{C.2}$$

with $C_{x} = \frac{3}{2}\left(\frac{3}{4\pi}\right)^{1/3}$. We can then write Eq. C.1 as:

$$E_{\mathrm{x}} = -C_{x} \sum_{\sigma} \int \rho_{\sigma}^{4/3} \Big(1 + \frac{\beta/C_{x} x_{\sigma}^{2}}{1 + \gamma\beta x_{\sigma} \mathrm{arcsinh}(x_{\sigma})}\Big) d\mathbf{r} \tag{C.3}$$

For a spin unpolarized system, $\rho_{\uparrow} = \rho_{\downarrow} := \rho_{s}$ with $\rho = 2\rho_{s}$. As a result, $x_{\uparrow} = x_{\downarrow} := x$, and we can write

$$x = \frac{|\nabla\rho_{s}|}{\rho_{s}^{4/3}} = 2^{1/3} \frac{|\nabla\rho|}{\rho^{4/3}} \tag{C.4}$$

Performing the sum over spins, Eq. C.3 becomes:

$$\begin{aligned} E_{\mathrm{x}} &= -C_{x} \int 2\rho_{s}^{4/3} \Big(1 + \frac{\beta/C_{x} x^{2}}{1 + \gamma\beta x \ \mathrm{arcsinh}(x)}\Big) d\mathbf{r} \\ &= -A_{x} \int \rho^{4/3} \Big(1 + \frac{\beta/C_{x} x^{2}}{1 + \gamma\beta x \ \mathrm{arcsinh}(x)}\Big) d\mathbf{r} \end{aligned} \tag{C.5}$$

where $A_x = \frac{3}{4}(\frac{3}{\pi})^{1/3}$. From Eq. C.5, we can write the enhancement factor:

$$F_{\mathrm{x}}(x) = 1 + \frac{\beta/C_x x^2}{1 + \gamma\beta x \ \mathrm{arcsinh}(x)}. \tag{C.6}$$

We now want to express this in terms of the dimensionless gradient

$$s = \frac{|\nabla\rho|}{2(3\pi^2)^{1/3}\rho^{4/3}} \tag{C.7}$$

which means we can write $x = 2^{4/3}(3\pi^2)^{1/3}s := cs$ from Eq. C.4. Now the enhancement factor becomes

$$F_{\mathrm{x}}(x) = 1 + \frac{s^2\beta/C_x c^2}{1 + \gamma\beta \ cs\mathrm{arcsinh}(cs)} \tag{C.8}$$

with

$$\beta' = c\gamma\beta \tag{C.9}$$

$$\mu = \frac{\beta}{C_x}c^2 \tag{C.10}$$

$$\text{so } \beta' = 9\frac{\mu}{2c}\left(\frac{6}{\pi}\right)^{1/3} \tag{C.11}$$

and finally

$$F_{\mathrm{x}}(s) = 1 + \frac{\mu s^2}{1 + \beta' s \ \mathrm{arcsinh}(cs)}. \tag{C.12}$$